Universität Stuttgart

Development of a Bioinspired Multimodal Mobile Robot Platform

Von der Stuttgarter Zentrum für Simulationswissenschaften (SC SimTech)
der Universität Stuttgart zur Erlangung der Würde eines Doktors-Ingenieurs
(Dr.-Ing.) genehmigte Abhandlung

Vorgelegt von
HyunGyu Kim
aus Daegu, Südkorea

Hauptberichter:	Prof. Dr. Metin Sitti
Mitberichter:	Prof. Dr. Syn Schmitt
Mitberichter:	Prof. Dr. Matthew A Woodward
Prüfungsvorsizender:	Prof. Dr. David Remy

Tag der mündlichen Prüfung: 24. April. 2024

Max-Planck-Institut für Intelligente Systeme

2024

ABSTRACT

Mobile robots can provide services for humans to replace dangerous tasks in unstructured environments, such as disaster sites; therefore, mobile robots are required to overcome various obstacles, such as debris, and generate propulsion under various conditions, such as terrain, water, and air. Multimodal locomotion is one of the solutions for these challenges in unstructured environments. This dissertation develops a multimodal robotic platform to integrate multiple locomotion modes: jumping, perching, and gliding. The development process includes mainly two tasks to integrate locomotion modes and improve the performance of each mode: a mechanical design and studying the interactions between integrated modes. The first task conducts design processes for the perching mechanism, active tail, wing, and gliding dynamics. The perching mechanism is inspired by a bird's leg so that the mechanism has 3D-printable viscoelastic material like a bird's muscles to absorb perching shock and claws to make interlock on surfaces. The design process of the perching mechanism includes characterizing the shock-absorbing and engagement performances according to design parameters and perching conditions. The demonstration proves and discusses the performance of the designed perching mechanism on various surface conditions. The robot employs an active tail for dynamic orientation control. Control torques from the active tail are characterized according to

design parameters from the simplified single-axis dynamic and experimental models and operating strategies. Also, the characterization includes the aerodynamic effects on the active tail. The characterization provides initial design inspirations to employ the active tail. As the final design, passive and active gliding dynamics are designed through an airfoil configuration and dynamic control of gliding angle in simulation. The best location of the body's center of mass has stable gliding behavior and the longest gliding distance. The optimization of the active gliding is for the control strategy of the gliding angle to maximize the gliding distance. As the second task, this dissertation studies interactions between the integrated locomotion modes. During the transition of the locomotion modes, modes share the robot's orientation and moving speed. Therefore, the previous modes determine the initial conditions for the next locomotion mode. This dissertation searches for strategical interaction between modes through demonstrations to improve performances of multimodal locomotion. Through these design tasks and studying interactions of integrated locomotion modes, the developed multimodal robotic platform successfully integrates jumping-gliding and jumping-perching through demonstrations. Finally, this dissertation introduces and discusses achieved features from multimodal locomotion, such as improved maneuverability under various operating conditions, overcomable obstacles, and specific functions during locomotion modes. I hope the results of this dissertation contribute to developing multimodal robotic platforms to replace dangerous works in accident sites.

ZUSAMMENFASSUNG

Mobile Roboter können Dienstleistungen für Menschen erbringen, um gefährliche Aufgaben in unstrukturierten Umgebungen, wie z. B. an Katastrophenorten, zu ersetzen. Daher müssen mobile Roboter verschiedene Hindernisse, wie z. B. Trümmer, überwinden und unter verschiedenen Bedingungen, wie z Luft. Multimodale Fortbewegung ist eine der Lösungen für diese Herausforderungen in unstrukturierten Umgebungen. Diese Dissertation entwickelt eine multimodale Roboterplattform zur Integration mehrerer Fortbewegungsmodi: Springen, Hocken und Gleiten. Der Entwicklungsprozess umfasst hauptsächlich zwei Aufgaben zur Integration von Fortbewegungsmodi und zur Verbesserung der Leistung jedes Modus: ein mechanisches Design und die Untersuchung der Wechselwirkungen zwischen integrierten Modi. Die erste Aufgabe führt Designprozesse für den Sitzmechanismus, das aktive Leitwerk, den Flügel und die Gleitdynamik durch. Der Sitzmechanismus ist von einem Vogelbein inspiriert, sodass der Mechanismus über 3D-druckbares viskoelastisches Material wie die Muskeln eines Vogels verfügt, um Stöße beim Sitzen zu absorbieren, und Krallen, um sich auf Oberflächen zu verriegeln. Der Konstruktionsprozess des Sitzmechanismus umfasst die Charakterisierung der Stoßdämpfungs- und Eingriffsleistungen gemäß Konstruktionsparametern und Sitzbedingungen. Die Demonstration beweist und diskutiert die Leistung des entworfenen Sitzmechanismus

bei verschiedenen Oberflächenbedingungen. Der Roboter verwendet einen aktiven Schwanz zur dynamischen Orientierungskontrolle. Steuerdrehmomente vom aktiven Heck werden gemäß Konstruktionsparametern aus den vereinfachten einachsigen dynamischen und experimentellen Modellen und Betriebsstrategien charakterisiert. Die Charakterisierung umfasst auch die aerodynamischen Auswirkungen auf das aktive Heck. Die Charakterisierung liefert erste Designinspirationen für den Einsatz des aktiven Hecks. Als endgültiges Design werden die passive und aktive Gleitdynamik durch eine Profilkonfiguration und eine dynamische Steuerung des Gleitwinkels in der Simulation entworfen. Die beste Lage des Körperschwerpunktes hat ein stabiles Gleitverhalten und die längste Gleitstrecke. Das Design des aktiven Gleitens optimiert die Steuerstrategie des Gleitwinkels, um die Gleitstrecke zu maximieren. Als zweite Aufgabe untersucht diese Dissertation Wechselwirkungen zwischen den integrierten Fortbewegungsmodi. Während des Übergangs der Fortbewegungsmodi teilen sich die Modi die Orientierung und Bewegungsgeschwindigkeit des Roboters. Daher werden Anfangsbedingungen für den nächsten Fortbewegungsmodus durch die vorherigen Modi bestimmt. Diese Dissertation sucht nach strategischer Interaktion zwischen den Modi durch Demonstrationen, um die Leistungen der multimodalen Fortbewegung zu verbessern. Durch diese Entwurfsaufgaben und das Studium der Wechselwirkungen integrierter Fortbewegungsmodi integriert die entwickelte multimodale Roboterplattform erfolgreich Springen-Gleiten und Springen-Hocken durch Demonstrationen. Abschließend werden in dieser Dissertation erreichte Merkmale der multimodalen Fortbewegung vorgestellt und diskutiert, wie verbesserte Manövrierfähigkeit unter verschiedenen Betriebsbedingungen, überwindbare Hindernisse und spezifische Funktionen während Fortbewegungsmodi. Ich hoffe, dass die Ergebnisse dieser Dissertation zur Entwicklung multimodaler Roboterplattformen beitragen, um gefährliche Arbeiten an Unfallstellen zu ersetzen.

ACKNOWLEDGEMENTS

I would like to thank my advisor, Prof. Metin Sitti, for allowing me to work in the Physical Intelligence Department at the Max Planck Institute for Intelligent Systems, Stuttgart. I appreciate his warm support, guidance, and freedom in my research. Without his support, it would not have been possible. I would like to thank Prof. Matthew A Woodward for all the detailed and regular discussions and for sharing his research philosophy. I would like to thank Prof. TaeWon Seo for his warm teaching and for initiating my research interests. I would like to thank the Max Planck Society for funding this dissertation. I also like to thank Prof. Frank Allgöwer, who accepted me to enroll as a Ph.D. student at Universität Stuttgart. I am grateful to Prof. David Remy and Prof. Syn Schmitt for serving on my thesis committee.

I want to thank all group members and my colleagues from Universität Stuttgart, Samuel Leder, and my office maters, Dr. Yunwoo Lee, Dr. Varun Sridhal for brilliant discussions, motivation, and wonderful times as friends during my first stay abroad in Germany.

I want to thank MPI service groups, Zentralen Mechanischen Werkstatt, Feinmechanische Werkstatt, and robotics, for their warm and professional support. I would also like to thank staff and technician in our group, Patricia Martinez and Janina Schwartz, for their warm support for administration and institute life; Gerd Hoerner and Maritta Dudek for their kind management of

order requests; Jack Saud for IT supports. Without these supports, it would not have been possible.

I am very grateful to my parents for their support during my Ph.D. Also, I thank my parents-in-law for all their motivation and warm hearts. I also thank the Anderer family for their support for my German life. Special thanks to my wife, Dr. Minjae Kim, and daughter, Ein Kim, for unforgettable precious memories, support, motivation, and love.

Thanks all.

CONTENTS

LIST OF FIGURES

LIST OF TABLES

NOMENCLATURE

α_t	Angular acceleration of the tail
$\ddot{\theta}_p$	Angular acceleration in pitch direction
$\ddot{y}$	Acceleration in Z axis
$\ddot{z}$	Acceleration in Z axis
$\dot{\theta}_p$	Angular velocity in pitch direction
$\dot{\vec{P}}$	Velocity vector for each component in dynamic model
$\dot{y}$	Velocity in Y axis
$\dot{z}$	Velocity in Z axis
η	Efficiency of a gear head
ω_b	Angular velocity of the body

ω_t	Angular velocity of the tail
ρ	Density of air
τ_{AD}	Torque from drag force of the air at the wing
τ_A	Transmitted torque from aerodynamic force of the tail
τ_C	Transmitted torque from centrifugal force of the tail
τ_{ex}	External torque
τ_{in}	Input torque
τ_I	Transmitted torque from inertia of the tail
τ_{tr}	Instantaneously transmitted torque
τ_T	Transmitted torque from tangential force of the tail
θ_a	Pitch angle of the robot from the initial position to the apex
θ_b	Body's pitch angle
θ_c	contact angle
θ_f	foot angle
θ_i	Angle of each component in dynamic model
θ_j	Jumping angle
θ_l	Leg angle of the perching mechanism
θ_f	Angle of the air flow

θ_p	Robot's pitch angle during gliding
θ_{tg}	Target rotating angle of the tail
$\vec{f}$	Vector for air flow
$\vec{P}$	Position vector for each component in dynamic model
A_{drag}	Air drag area
C_d	Air drag coefficient
C_k	Constant to define torque from spring
C_{AD}	Drag coefficient the wing in the body frame
c_l	Cord length of the wing
C_M	Moment coefficient the wing in the body frame
C_Y	Drag coefficient in Y direction in inertia frame
C_Z	Drag coefficient in Z direction in inertia frame
D_a	Distance of the robot from the initial position to the apex
D_l	Jumping distance of the robot at the landing position
D_p	Changed jumping distance between jumping with angle and the integrated perching motion
E_H	Energy in horizontal direction
E_O	Overall energy
E_V	Energy in pitch direction

E_V	Energy in vertical direction
E_{ab}	Absorbed energy through perching mechanism
F_a	Force in the axial direction to the perching mechanism’s leg
F_D	Air drag force at the tail
F_f	Force to fold the leg
$F_f r$	Friction force to fold the leg
F_r	Reaction force from the perching surface
F_{AD}	Drag force of the air at the wing
g	Gravitional constant
H_a	Height of the robot at the apex
I_b	Body’s moment of inertia
I_i	Moment of inertia of each component in dynamic model
I_t	Tail’s moment of inertia
I_{pitch}	Moment of inertia for the robot
K^*	Affected spring coefficient
K_g	Empirically measured constant to define mechanical resistance forces of the DC motor
K_t	Torque constant of DC motor
KE_i	Initial kinetic energy

KE_{tail}	Kinetic energy of the tail
KE_t	Kinetic energy after perching
l_i	Initial length of a spring
l_p	Length of perching mechanism
l_s	Length of a spring
l_t	Length of tail
l_{CoP}	Distance between the tail's rotating point and center of pressure
l_{CP}	Distance between the center of pressure and connection point of the wing
l_{mt}	Distance between body's mass center and connecting point of the tail
l_{mw}	Distance between body's mass center and connecting point of the jumping mechanism
l_{ww}	Height difference between body's mass center and connecting point of the jumping mechanism
m_b	Mass of body
m_i	Mass of each component in dynamic model
m_b	Mass of robot
n	Gear ratio of the gear head
P_0	Origin

P_m	Position of main body
R_m	DC motor resistance
T_a	Elapsed time of the robot to reach the apex
T_l	Elapsed time of the robot at the landing position
v_a	Horizontal speed of the robot at the apex
v_b	Initial velocity of the robot during perching
v_{ex}	velocity of external air flow
v_{flow}	Air flow speed generated by a wind tunnel
V_{in}	Input volt
w_l	Length of the wing
w_w	Width of the wing
AoA	Angle of attack
$\mathbf{CM}_R$	Position of the mass center of the main body from wing's leading edge
CoP	Center of the pressure of the tail's aerodynamic area
CP	Center of the pressure of the wing's aerodynamic area
Hardness	Shore A hardness of the viscoelastic material
$\mathbf{KE}_i$	Kinetic energy of each component in dynamic model
$\mathbf{PE}_i$	Potential energy of each component in dynamic model

CHAPTER 1

INTRODUCTION

1.1. Introduction

Robots provide services for humans, especially doing dangerous tasks instead of humans. Accident sites are representative examples. Due to accident site's risks, such as additional collapse, fires, and radiation, humans sometimes have limited access for rescue and recovery tasks. For example, The Fukushima nuclear disaster occurred in 2011, but human access to recovery tasks is still restricted by radiation. As one of the alternative plans, several robots were immediately deployed to investigate the accident sites, as listed in Table 1.1. Using robots is still underway [1, 2], and we expect them to provide enough inside information to minimize radioactive contamination. Boat sinking accidents also have challenges to humans due to limited sight, ocean currents, and low temperatures. Robots can be free from these dangers and do tasks instead of humans [3, 4]. As the last example, building collapse always has issues with additional collapses, explosions, and fires. Robots can explore inside situations to find survivors and provide information to rescue survivors [5, 6, 7].

Table 1.1.: Robots deployed for Fukushima nuclear disaster [8]

Manufactureer	Robot	Tasks
iRobot	Packbot	Visual exploring, Radiological monitoring, Robotic arm manipulation
	Warrior	Visual exploring, Robotic arm manipulation
QinetiQ	Dragon Runner	Visual Exploring, Robotic arm manipulation
	Talon	Visual Exploring, Radiological monitoring, Robotic arm manipulation
Chiba Tech. Tohoku Univ.	Quince	Visual exploring, Radiological monitoring, Robotic arm manipulation

The main challenges to the robot locomotion in the accident sites are

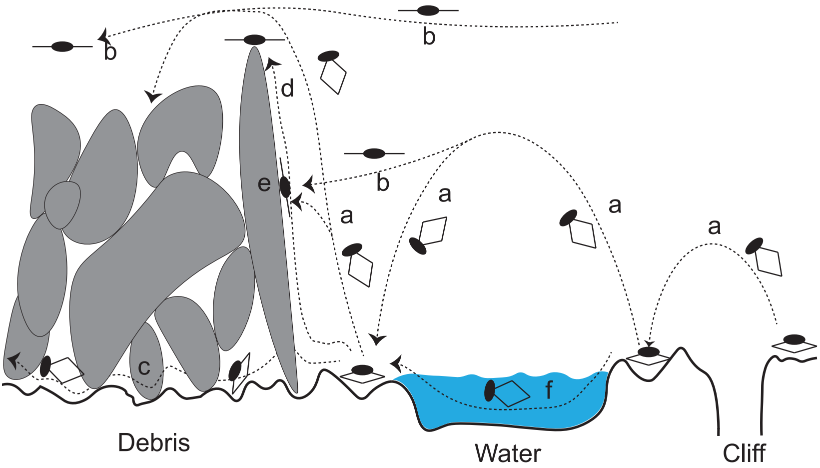

Figure 1.1.: Possible locomotion modes at the unstructured environment to overcome obstacles and generate propulsion. a. jumping, b. gliding, c. crawling, d. climbing, e. perching, f. swimming.

obstacles and different propulsion conditions, as shown in Figure 1.1. As the robot can overcome various obstacles and generate propulsion under multiple conditions, the robot has robust performance in any accident site. The accident site's unstructured environment has various obstacles, such as stairs and debris, which hinder the robot's mobility. Robots can overcome these obstacles through specific motions. For example, jumping or gliding allows the robot to pass obstacles (Figure 1.1a and b); crawling makes the robot pass the narrow spaces (Figure 1.1c); climbing overcomes any height of obstacles (Figure 1.1d). Furthermore, the accident sites may have various propulsion conditions, such as terrain, water, and air, therefore generating propulsion in multiple conditions improves the robot's maneuverability, even in overcoming obstacles. For example, integrated jumping-gliding motion can have additional moving distance from gliding compared with distances from pure jumping, which allows overcoming short jumping distances (Figure 1.1a→b); in the case of integrating perching and climbing into the jumping robot, perching after jumping provides a stationary height for tasks at high positions, such as visual exploring and charging through the solar cells, in addition climbing supplements low jumping heights to overcome tall obstacles. (Figure 1.1a→e→d); integrated crawling-swimming allows the robot to overcome more propulsion conditions, terrain and water (Figure 1.1f→c). As a result, although each motion provides solutions to overcome obstacles, integrating these locomotion modes improves the overcoming performance further and extends the operating conditions. Examples of multimodal robots and achieved features are as follows:

- Jumping-Gliding [9, 10, 11, 12, 13, 14, 15] :

  Obtaining initial potential energy for gliding during jumping, and Increasing jumping distance by performing the gliding after jumping.

- Flying-Perching [16, 17, 18, 19, 20, 21] :

  Flying to target spots, and conducting tasks without locomotion through perching, such as charging through a solar cell and sensing for environmental monitoring.

- Swimming-Walking [22, 23, 24, 25, 26, 27, 28, 29, 30] :

  Extending working conditions by generating propulsion in both environments.

- Running-Flying [31, 32, 33] :

  Enhancing running stability through balancing forces from flying.

Creatures in nature provide a lot of inspiration for robots' locomotion and mechanisms to generate propulsion. There are many works to develop bioinspired mechanisms and apply propulsion strategies to robot design. Creatures generate instantaneous jumping power from leg mechanisms, and roboticists have applied these jumping mechanisms to robots: locus-inspired [34], frog-inspired [35], and kangaroo-inspired [36] robots. A bird's flapping motion generates continuous air drag and lifting forces for flying. Researchers have observed the bird's flapping behaviors and applied them to robots: insect- [37], and bird- [38, 39] inspired robots. Researchers have observed Cockroach's crawling behaviors to pass narrow spaces and applied the mechanism to robots[40, 41, 42]. Creature's climbing is also a fascinating motion to the robotists. For climbing, Robots need holding forces to the climbing surfaces, such as adhesion or interlocking. Gecko lizards climb surfaces with their adhesive foot hairs through van der Waals adhesion [43]. Researchers have mimicked the Gecko's foot hair [44, 45, 46] and behaviors for attachment and detachment mechanism [47, 48, 49, 50, 51]. Interlocking is another way to generate holding force to surfaces. A claw's sharp tip can establish interlocking. Researchers mimicked claws from creatures and developed climbing robots [52, 53, 54]. Finally, swimming allows the robot to generate locomotion in the water. Many researchers have developed fish-like robots by mimicking the undulation behavior of the fish [55, 56]. Interestingly, Basilisk lizards also cross the water by running on the water's surface through rapid leg rotation [57, 58, 59]. Robotists have also tried to mimic the lizard's leg mechanism, including foot trajectory. [23, 60, 61, 62]. As a result, creatures provide plenty of inspiration to develop bioinspired mechanisms and operating strategies for robot design.

To develop multimodal robots, the focus has been on developing the mechanisms to integrate multiple motions in a robotic platform. Creatures also provide inspiration to design the mechanism for motion integration. For example, flying squirrels can integrate walking, climbing, and gliding through legs and membranes formed between the legs. So, they can locomote on multiple propulsion conditions, and overcome various obstacles. Researchers developed a bioinspired mechanism like the flying squirrels to integrate gliding and walking motions [63]; Researchers have mimicked rapidly and repeatedly jump of arboreal mammals, specifically Galago, and integrate jumping on ground and vertical surfaces [64]. The multiple jumping on the horizontal and vertical surfaces allows the robot to change the jumping directions and varies the ability of the robot's obstacle overcoming. Robotists mimicked body undulation of Salamander lizards and snakes [65, 66] to integrate swimming and walking motions. The amphibious motion improves the robot's maneuverability by varying possible propulsion conditions. As a result, as the creatures locomote in various propulsion conditions with given mechanisms, robotists can combine bioinspired mechanisms for multimodal robot design, however strategically consider using the minimum number of mechanisms for motion integration because a single mechanism can generate propulsions in multiple environments.

Furthermore, from varying the working environment, roboticists have also studied strategic interactions between integrated motions. Each motion can cooperate to complement each other, maximizing performances of the integrated motions. In the case of integrated jumping and gliding motions, jumping motion provides the potential energy for gliding. The integrated gliding transforms the potential energy into propulsion using aerodynamics and generates longer jumping distances than a single jump [13, 14, 67, 11, 10]. Integrated walking and flying motions can also be very complimentary as orientation control is one of the challenging points for the bipedal walking robots. The actuators for flight control can assist in orientation control for the walking motion [68]. In addition, during near surface flight, intermittent surface contact can be used to stabilize the robot under external disturbances, such as air flows. As a result, considering the interaction between the integrated motions improves each motion's performance during the mechanism design for the motion integration.

As motion integration requires more dynamic and agile locomotion for robots, the search for additional control strategies has become more important. One such strategy being explored by robotists and inspired by animals is the inclusion of an inertial, aerodynamic, or hydrodynamic appendage (e.g., tail) [69, 70, 71]. These appendages have one or more controlled degrees of freedom (DOF) which increases the control inputs and thus the locomotion variability, adaptability, and controllability. An active tail has the effect of producing variable forces and torques on the body, which can enhance the dynamic motion control. While quadruped animals have sufficient DOF in their legs and spine to control their locomotion, many have an active tail to enhance their dynamic motion control and robustness further. A robotic example of this is seen in the MIT cheetah, which has sufficient DOF in the legs for stable running [72, 73, 74]; however, it can also benefit from the inclusion of a tail [75]. Current miniature robots tend to be very underactuated because of excessive design constraints [15, 76]. In this case, an active tail is one possible solution to add controlled DOF and improve dynamic motion control [77]. Miniature multimodal robots with limited DOF, such as the jumping and gliding robot, MultiMo-Bat [14], can potentially benefit even further as each mode can utilize the tail in different ways. It has already been shown that controlling the orientation at the initiation of gliding has a significant effect on the gliding performance [78]. Previous work has already shown the benefits of an active tail in animals including, Libby *et al.* [79], Chang-Siu *et al.* [80], and Jusufi *et al.* [81], who observed how lizards use their active tails for body orientation control. This concept was then incorporated into a robot, which showed similar behaviors [82]. Therefore, employing the active tail for orientation control of the multimodal robot helps transition between motions and improves the stability of multimodal locomotion.

This work develops a multimodal robotic platform to integrate jumping, perching, and gliding modes. Through motion integration, this work improves the robot's maneuverability under unstructured environments, such as overcoming obstacles and operating under various propulsion conditions. One of the main tasks of this work is mechanical design for enhancing the performance of the locomotion mode. For the necessary components of each mode's function, the mechanical design includes not only developing, characterizing, and design of mechanisms or components, but designing the dynamics of each locomotion mode. This dissertation includes three design tasks: a design of a perching mechanism to absorb perching shock and make engagement at the surface, an airfoil design for passive gliding distance, a design of gliding dynamics to increase gliding distances, and an active tail characterization for dynamic orientation control. Introductions for each mechanism are described in section 1.1.1, and detailed tasks are described in each chapter in this dissertation. The other task is to study interactions during a transition of integrated locomotion modes. Strategical integration of the modes makes the robot use given energy efficiency and improves the performance of the multimodal locomotion. For instance, assuming the gliding of the multimodal robot is followed after jumping, the initial angle and height determined by integrated jumping significantly determine gliding behaviors. Initial perching speed and angle from the integrated jumping or gliding modes are important parameters for the success of perching. For favorable interactions during the transition, the robot employs an active tail, an aerodynamic tail, for pitch control. Through pitch control, each motion has favorable initial conditions to maximize performance. Strategical integration of the locomotion modes is described in section 1.1.2 with possible scenarios. I hope the results of this dissertation will be helpful in developing other multimodal robots in the future.

1.1.1. Mechanical design

A robotic platform and mechanisms for the integrated jumping-gliding have been developed in previous works [13, 14, 15], however this work renovates the old designs to integrate additional perching mode and employ an active tail for pitch control. In addition, this work improves performances of each locomotion mode through designs of mechanism and dynamics. This section introduces three main tasks: the development of the perching mechanism (section 1.1.1.1 [83]), the characterization of the active tail (section 1.1.1.2 [77]), and optimal airfoil configuration and control strategy for gliding (section 1.1.1.3 [78]). Each chapter in this thesis describes a detailed design process for each mechanism, and an overview of each chapter is as follows:

1.1.1.1. Developement of the perching mechanism

This work develops an avian-inspired perching mechanism to integrate perching with a jumping robot, as seen in Figure 1.2A. While a bird-inspired active mechanical perching mechanism was developed for the grasping or perching on branches [16], this work focuses on rough vertical surfaces. The perching mechanism is designed to passively absorb the perching impact and establish a mechanical interlock with the surface while minimizing weight, as this is a key parameter in determining the jumping performance. This work consists three main sections: First section is about characterization of the

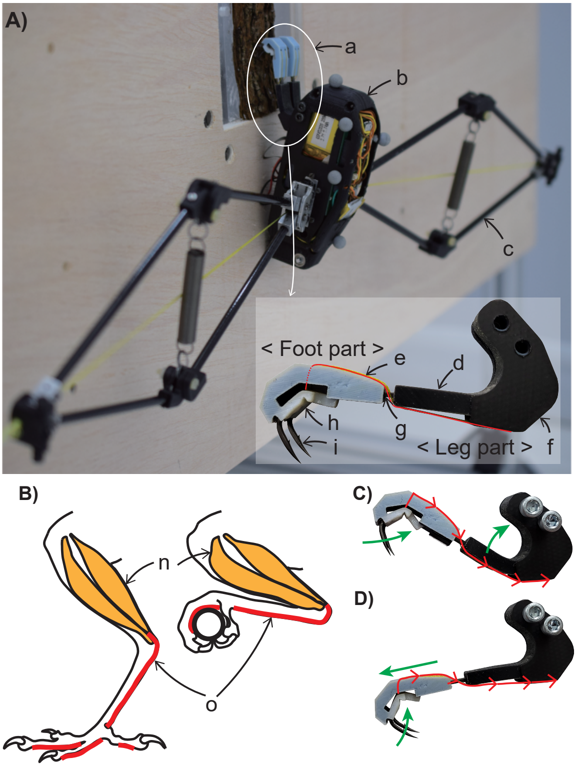

Figure 1.2.: Avian-inspired perching mechanism to integrate perching and jumping locomotion modes. A) Perching on a vertical wall (a. perching mechanism, b. robot body, c. four-bar jumping mechanism, d. viscoelastic shock absorbing material (bird's muscle), e. tendon for the passive fastening mechanism (bird's tendon), f. outer shell to fix the wire for the passive fastening mechanism, g. carbon load to assemble leg and foot parts, h. flexible claw holder for the fastening mechanism, i. claws for the mechanical interlocking). B) Bird's leg anatomy (j. muscle, k. tendon). C) Fastening mechanism through the leg folding. D) Fastening mechanism through the applied weight of the robot while perching.

shock-absorbing mechanism, which is a 3D-printable viscoelastic material. The viscoelastic characteristics for shock-absorption is inspired by bird's muscle in Figure 1.2B. Roboticists have previously employed viscoelastic materials to absorb perching shocks [84]; however, this work introduces a fully 3D printable viscoelastic digital material for shock absorption. The digital material can vary the hardness of the shock-absorbing mechanism through changing the ratios of the solid and flexible base materials during printing. The changes in the material ratio and material structure change the viscoelastic properties allowing for optimization of the shock-absorbing characteristics of the material. We first characterized the shock-absorbing performances according to various parameters, such as hardness of the material, foldable angle, thickness, mechanism length, perching speed, and perching angle. Second, we characterized the engagement performance of the gripper within the context of the energy-absorbing mechanism. This work studies mechanical interlocking and penetration as methods for engagement. The characterization of the engagement was conducted at different conditions, such as hardness of surfaces and contact angle of the claw, and includes performance changes of interlocking according to penetration. Experimental test were conducted to determine the performance characteristics of the mechanism both independently and within the complete system's locomotion behavior demonstrating the enhancement to jumping performance. Third, this work provides a design methodology for developing perching mechanisms for a target system. Detailed descriptions are in Chapter 2.

1.1.1.2. Characterization of active tail

Active tails can be categorized according to source of the induced force. The first type induces inertial forces, as seen in Figure 1.3A. Inertial tails use a distal mass to generate sufficiently high inertial forces to reorient the body. The inertial tail can be differentiated into different types, according to the position of the tail's center of mass (CoM) and the tail's connecting point on the body. The first type is a distal-mass inertial tail, which has a single distal point mass from the rotating axis. The tail's rotation generates

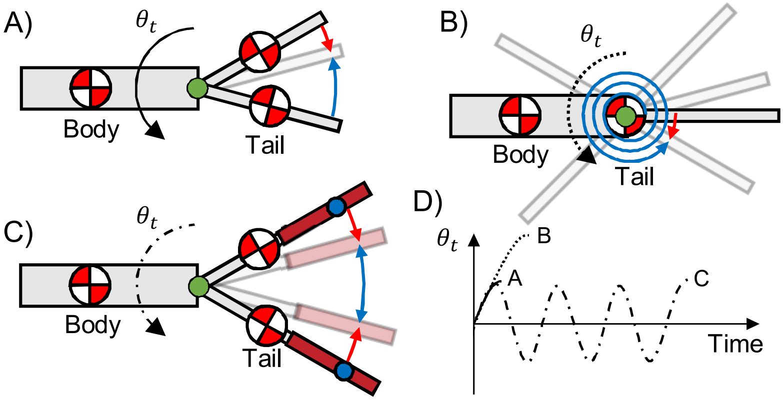

Figure 1.3.: Active tails with different types of induced forces and operating strategies. A) Partial oscillation of the distal-mass inertial tail: the tail has distal center of mass (CoM) from a rotating axis and makes single swing. B) Full rotation of the mass-balanced inertial tail: the tail has CoM at the rotating axis and makes multiple turns. C) Symmetric or asymmetric oscillation of the distal-mass aerodynamic tail: the tail has distal CoM from the rotating axis and makes multiple swings. D) Behaviors of the tail rotation. Red areas and blue circles in the tail denote an aerodynamic surface and center of pressure (CoP), respectively. Blue and red arrows denote the directions of acceleration and deceleration, respectively. Green circles denote the rotating axis of the tail.

several forces and torques, such as tangential forces, centrifugal forces, and inertial torques. A number of studies have explored different aspects of the distal-mass inertial tails, including their steering control for maneuverability [85], orientation control during jumping [86, 87], dynamic motion control of wheeled robots [88, 89], motion control of a kangaroo-inspired robot [90], and legged robots [91].

The next type is a mass-balanced inertial tail, as shown in Figure 1.3B. The tail's CoM is located at the rotational axis and therefore, the tail does not generate the centrifugal and tangential forces seen in the distal-mass type tails. The tail does, however, generates torque due to its angular acceleration.

This type is not common in nature, but some robots employ this tail because of the simplified design parameters [76, 92, 93, 64].

Tails can also generate aerodynamic forces based on their air drag surfaces, as shown in Figure 1.3C. In nature, flying squirrels have an aerodynamic tail to glide between neighboring trees [94, 95], and birds have an aerodynamic tail for flight control. These tails can generate forces through both external airflow over the surface and generated airflow through the motion of the surface. Motion of this tail type will also necessarily include inertial forces as well, however, aerodynamic forces can be used without the inertial component in the case of external air flow. A number of robots have employed minimal structures with thin films to create such drag surfaces[96, 97].

In addition to the tail type and design, the tail driving strategy has a significant affect on the performance of an active tail. This work focuses on characterizing the four different fundamental tail operation strategies: partial oscillation, symmetric oscillation, asymmetric oscillation, and full rotation, as can be seen in Figure 1.3. The characteristics of the locomotion strategy and the tail design itself, as components can interfere with each other, constrains the possible tail operation strategies for a given system. In the case of a short jump, an active tail only has a very limited time to operate. Therefore, it is likely limited to a partial oscillation, as shown in Figure 1.3A, and must create sufficient torque over this range to control the body orientation [79]. However, gliding locomotion has sufficient time for any of the specified operating strategies including full rotation (Figure 1.3B), and multiple partial oscillations in clockwise and counterclockwise directions (Figure 1.3C) [98]. The characteristics of the oscillations, such as asymmetric oscillation, can be used to bias the generated torques in the desired direction, while an aerodynamic tail can add additional biased torque. While the full rotation is similar to partial oscillation, tail rotation enters a steady-state behavior which allows for better control of the body's angular momentum [76, 99].

In this work, we cover the two fundamental single DOF inertial tail designs (mass-distal, mass-balanced), three aerodynamic configurations (inertial, aerodynamic, aerodynamic with external airflow), and the four fundamental operating strategies (partial oscillation, symmetric oscillation, asymmetric oscillation, full rotation) to determine under what conditions each of the 24 possible combinations is applicable and the performance associated with each. While previous works have studied tail performance from several perspectives, such as mass-distal inertial tails under partial oscillation [85, 86, 87, 88, 89, 90, 91], mass-balanced inertial tails under full rotation [76, 92, 93, 64], mass-distal aerodynamic tails under partial oscillation [100], and mass-distal hydrodynamic tails under oscillation [101], they have not yet explored how the full range of possible tail configurations, operation strategies, and aerodynamic effects could affect the reorientating performance of the body. Detailed descriptions are in Chapter 3.

1.1.1.3. Optimal airfoil configuration and control strategy for gliding

There are two general types of gliding: uncontrolled and controlled gliding. In the case of uncontrolled (passive) gliding, the focus is placed on the aerodynamic design as the energy conversion efficiency determines the gliding performance. For this reason, previous works have studied airfoil designs, such as comparative studies focused on the aerodynamics of the different wing airfoils to find efficient wing configurations [102, 103], while others focused on optimization of the jumping and gliding behavior [9]. This work focuses on a key characteristic of the encoded morphological intelligence, that of the optimal relative position of the robot's center-of-mass (CM_R) in relation to the range of its center-of-pressure (CP). The position of the CP changes with the angle-of-attack (AoA), and different locations of the CM_R in relation to the CP determine the overall passive gliding behavior. We find the optimal location of CM_R to maximize the passive gliding ratio and stability of the MultiMo-Bat's gliding. Controlled (active) gliding adds several additional parameters, as energy can be added to the system while gliding. Active gliding can be controlled by steering mechanisms, such as rudder or morphological change of the wing, and control the gliding trajectory [104, 105, 106]. Many animals, such as lizards and flying squirrels, use their tails to control their aerial trajectories [107, 108, 109]. This work studies using an active tail to improve a robot's gliding distance. Detailed descriptions are in Chapter 4.

Figure 1.4.: Configuration of the airfoil. Red arrow denotes gliding direction. Black-dotted arrows denote leading edge of the different locations of the robot's center-of-mass (CM$_R$). The 30 % to 50 % denote locations of CM$_R$ of the chord length measured from the leading edges. The mark of the CM$_R$ is representated on the wing.

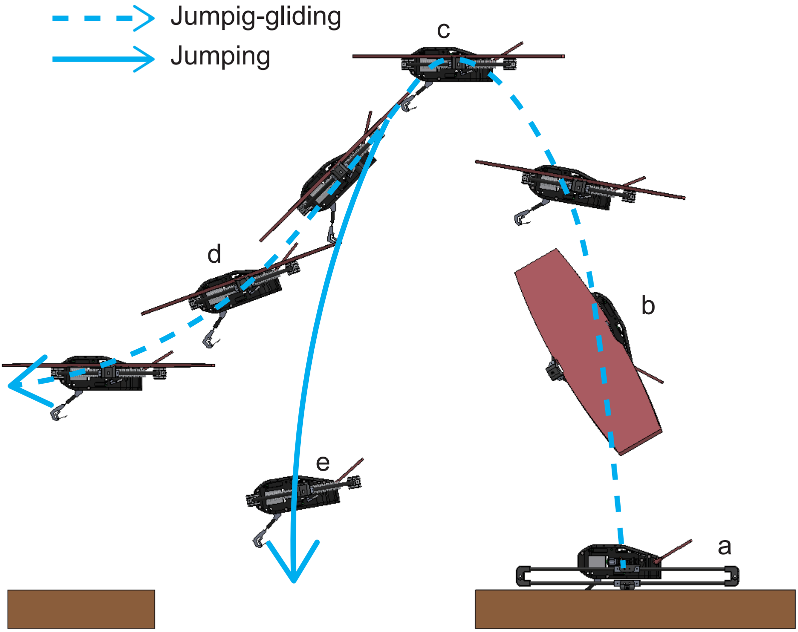

Figure 1.5.: Scenario for integration of locomotion modes: jumping and perching. a. jumping from the ground, b. mechanism opening for perching and pitch control through the active tail, c. apex of jumping trajectory, d. gliding after jumping, e. falling after jumping. Integrating locomotion modes supplements short jumping distances and improves the ability to overcome obstacles.

1.1.2. Strategical integration of the locomotion modes

Integration of the locomotion modes improves each mode's performance, such as jumping or gliding distance, and abilities to overcome obstacles, Furthermore, the improvement can be maximized through strategic interactions during the transition of the modes. Figure 1.5 depicts a scenario of integrated jumping and gliding modes. The robot initially jumps from the ground and generates enough height to glide; tail's pitch control during the jumping provides proper initial gliding angles; with the height and initial gliding angle from the jumping, a membrane of the mechanism generates air drag for gliding. Although similar integration of locomotion modes has been studied in several works [13, 14, 67, 11, 10], this work not only employs active tail to add additional dynamic pitch control during jumping [77] but observes strategy of the gliding angle control to enhance the gliding distances [78]. The additional gliding after jumping provides more horizontal moving distances than pure jumping, therefore overcomable obstacles can be diversified. Integrating additional perching improves system performance further like Figure 1.6. The robot initially jumps from the ground and perches on the vertical surface. For successful perching, the active tail controls pitch orientation during jumping to provide the best perching angle. After perching, the horizontal jumping from the vertical surface provides initial horizontal velocity, and the robot can overcome obstacles that cannot be overcome through pure jumping. Specifically, the initial velocity is powerful to increase the gliding distance, therefore integrating gliding after perching can have more overcomable obstacles. In addition, perching provides stationary height to the robot for specific tasks at the elevated position, such as visual sensing for mapping the target area. As a result, this work studies interactions between the integrated locomotion modes to maximize the achieved features from these motion integration.

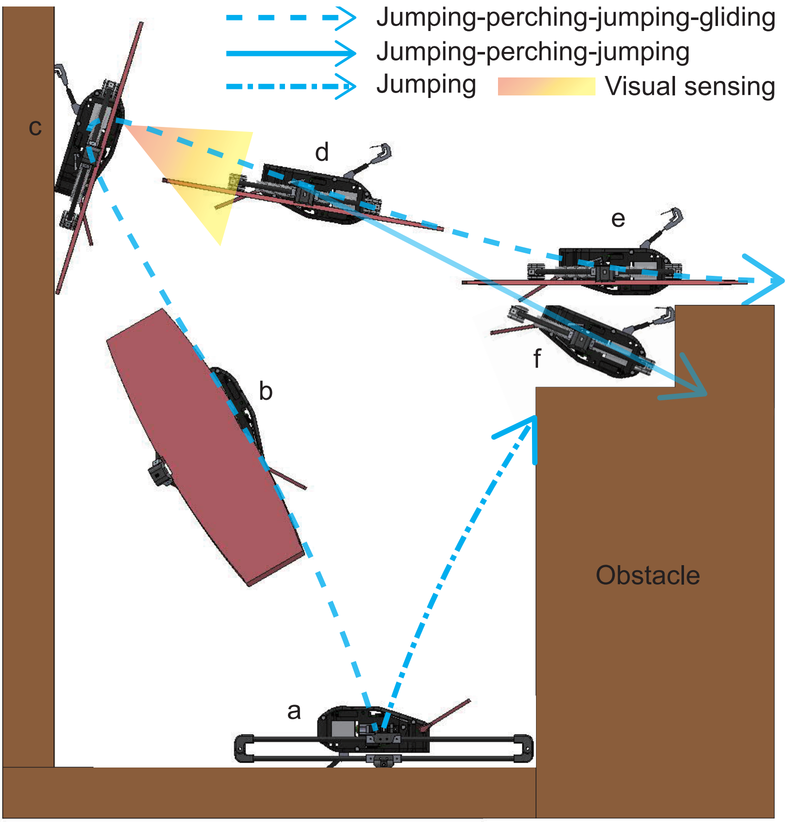

Figure 1.6.: Scenario for integration of locomotion modes: jumping, perching, and gliding. a. jumping from the ground, b. mechanism opening for perching and pitch control through the active tail, c. perching on the vertical surface at the apex of the jumping trajectory, d. jumping from the vertical surface and transitioning to gliding, e. gliding, f. falling after jumping from the vertical surface. Integrating locomotion modes strategically supplements short jumping distances and improves the ability to overcome obstacles. In addition, motion integration can provide the proper environment for specific tasks, such as visual sensing for mapping obstacles.

The structure of this thesis

The structure includes three main parts, integrating perching motion on the jumping robot, active tail characterizations to incorporate it for improving the performance of multimodal locomotion, and improving the gliding performance through both optimizations of the passive dynamics and active pitch control strategy. Chapter 2 introduces the bioinspired perching mechanism. Through the characterization of the shock-absorbing and engagement performances according to the design parameters, a design methodology is discussed to employ the mechanism to the target system. In addition, integrated jumping and perching motions are showcased at the various surface condition, and the performance of the multimodal locomotion is discussed. Chapter 3 describes the single-axis active tail characteristics to generate pitch control torque. This chapter observes changes in generated torque from the active tail according to the design parameters, aerodynamic effects, and operating strategies. In addition, the chapter provides design guidelines for various target systems. Chapter 4 presents the experimental results of the jumping-gliding robot and the optimization of the passive gliding dynamics, furthermore develops the dynamic simulations used to determine the aerodynamic coefficients and optimize the tail control strategy. Conclusion and future works are mentioned in Chapter 5.

This dissertation combines below three papers, which are edited and revised to match the context of this dissertation. All publications are properly cited in the relevant sections of the dissertation:

1. H Kim, M A Woodward, M Sitti, "Avian-Inspired Perching Mechanism for Jumping Robots", Advanced Intelligent Systems, 2022, Submitted [83].

2. H Kim, M A Woodward, M Sitti, "Active Tail Configurations for Enhanced Body Reorientation Performance", Advanced Intelligent Systems, 2022, http://doi.org/10.1002/aisy.202200219 [77].

3. H Kim, M A Woodward, M Sitti, "Enhanced Non-Steady Gliding Performance of the MultiMo-Bat through Optimal Airfoil Configuration and Control Strategy", IEEE/RSJ International Conference on Intelligent Robots and Systems (IROS), 2018, pp. 1382-1388 [78].

1.2. Methodology

Chapters in this dissertation share the same robotic platform, measurement equipment, and specific coefficients. Therefore, the methodology section provides configurations of the robot, set-up of the measurement equipment, and estimation of necessary coefficients to support each chapter.

1.2.1. Configurations of the multimodal robotic platform

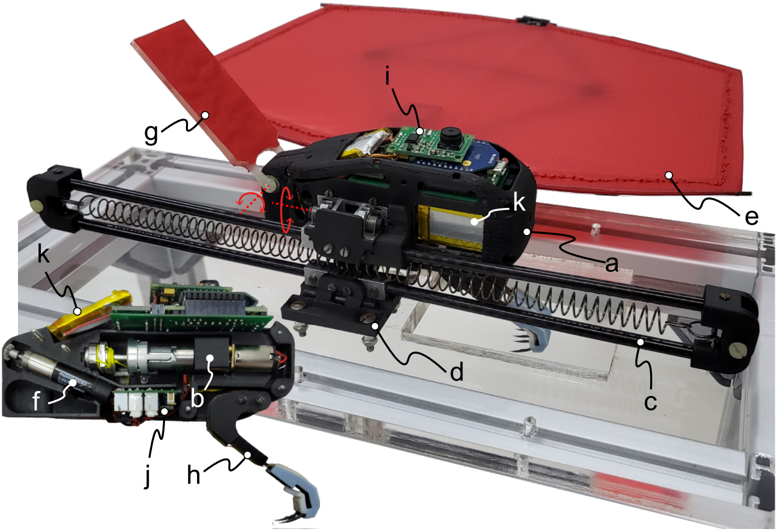

Figure 1.7.: Multimodal robotic platform to integrate jumping, perching, and gliding. a. 3D printed body frame, b. Energy storage and release mechanism (chapter 1.2.1.1), c. Jumping mechanism (compressed state, chapter 1.2.1.2), d. foot holder to remove slip while jumping, e. gliding mechanism (released state, chapter 1.2.1.2), f. geared dc motor and gear connection for the active tail actuation (chapter 1.2.1.4), g. single-axis aerodynamic tail for pitch control of the robot, h. perching mechanism (chapter 1.2.1.3), i. Main electronic board for a controller, sensor, and commutation (chapter 1.2.1.5), j. Sub electronic board for power management and tail control (chapter 1.2.1.5), k. Battery (chapter 1.2.1.5).

Figure 1.7 depicts the overall configurations of the multimodal robot. The robot integrates multiple locomotion modes: jumping, perching, and gliding, therefore, has mechanisms for each motion: jumping mechanism (Figure 1.7C), perching mechanism (Figure 1.7h), and gliding mechanism (Figure 1.7e). The jumping and gliding motions share the same mechanism. Because the weight of the material significantly affects jumping performance, light and durable materials were selected to fabricate each component, therefore the components consist of machined aluminum and 3D-printed carbon chopped plastic. An aerodynamic tail is employed to control the robot's pitch for the initial conditions of each motion and performance improvement (Figure 1.7 g). Although actuators operate the jumping mechanism and active tail (Figure 1.7 b, f), the perching mechanism and jumping-gliding mechanism's opening for motion transition operate passively to save energy consumption and simplify the actuator control system. Electronics provide actuator control, sensing the robot's behaviors, taking pictures for exploring purposes, and wireless communication (Figure 1.7i, j). Detailed specifications of the robot are listed in Table 1.2. 3D model and assembly design are provided in FigureC.1 in AppendixC.

This section describes an overview of each mechanism's design and operation process. Each chapter in this dissertation describes detailed design processes and characterizations for each mechanism.

1.2.1.1. Jumpign energy storage and release mechanism

For jumping, the robot is required to do two actions: storing and releasing the jumping energy. The jumping mechanism, the four-bar mechanism, has a spring, as shown in Figure 1.9c. An energy storage mechanism deforms the jumping mechanism through wire winding and generates jumping energy with spring stretching (chapter 1.2.1.2). The same mechanism also releases the stored energy instantaneously to make momentum in the robot's body for jumping. This work develops a clutch mechanism with a single-axis rotation to share the single mechanism for energy storage and release actions. Therefore, the mechanism is operated by one actuator and minimizes occupied weight to the robot, which significantly affects overall jumping height.

Table 1.2.: Specification of the multimodal robot

Components	Value
Body assembly	103.5 g
Body frame	31.4 g
Energy storage and release mechanism	18.4 g
Main electronic board	17.9 g
Sub electronic board	5.3 g
Battery	4.7 g (3 ea)
Tail actuator	8.1 g
Gears for tail operation	1.2 g
Misc. components (hardware and cables)	7.1 g
Width	31 mm
Length	109 mm
Height	44.7 mm
Jumping-gliding mechanism	35.8 g (2 ea)
Leg link	5.9 g (4 ea)
Foot	1.5 g
spring for jumping energy	6.2 g
Shoulder	4.5 g
Width (released state)	127.62 mm
Length (released state)	232.93 mm
Spring length (released state)	97.62 mm
Length (compressed state)	2.5 mm
Width (compressed state)	281.7 mm
Spring length (compressed state)	251.7 mm
Membrane width	274.5 mm
Membranes length	274.5 x 270.3 mm
Perching mechanism	7.5 g
Shock absorbing part	4.1 g
Foot part	1.3 g
connector	2.1 g

Detailed tail specifications are excluded because the tail is not optimized yet, although the tail is characterized in Chapter 3. The tail will be optimized to integrate full locomotion modes from jumping, perching, to gliding in future work.

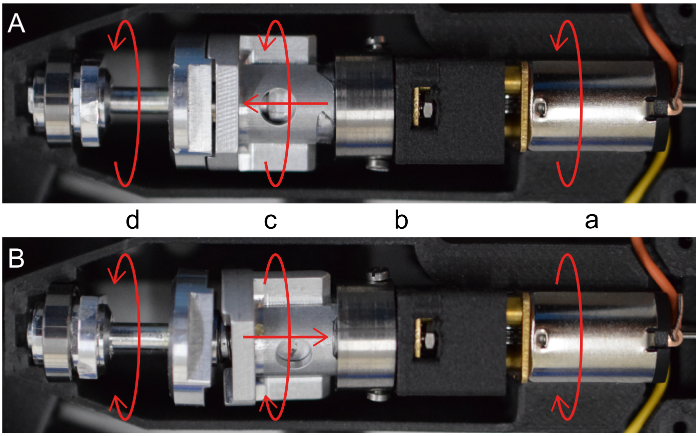

Figure 1.8.: Jumping energy storage and release mechanism. A. winding the wire to stretch the spring in the jumping mechanism, B. releasing the stored jumping energy through clutch actuation, a. geared DC motor (Pololu 1000:1), b. groove for clutch's moving in the axial direction, c. clutch, d. winder.

The single degree of freedom (DOF) mechanism can be a clutch to operate the winder, as shown in Figure 1.8. According to the rotating direction of the DC motor, a clutch is connected (Figure 1.8A) or disconnected (Figure 1.8B) with a winder. While a connection between the groove (Figure 1.8b) and clutch (Figure 1.8c) parts pushes the clutch to connect the clutch with the winder as shown in Figure 1.8A, rotating in the opposite direction pulls the clutch to disconnect the clutch with the winder as shown in Figure 1.8B. Therefore, the single DOF mechanism can store jumping energy by stretching the spring through winding, and releasing the energy through clutch actuation. An exploded assembly view is provided in FigureC.1C.

1.2.1.2. Jumping-gliding mechanism

Previous works developed a mechanism to generate propulsion for jumping and gliding modes. [13, 14, 15]. A spring stretch by deformation of the jumping mechanism generates jumping energy, Figure 1.9c; a membrane,

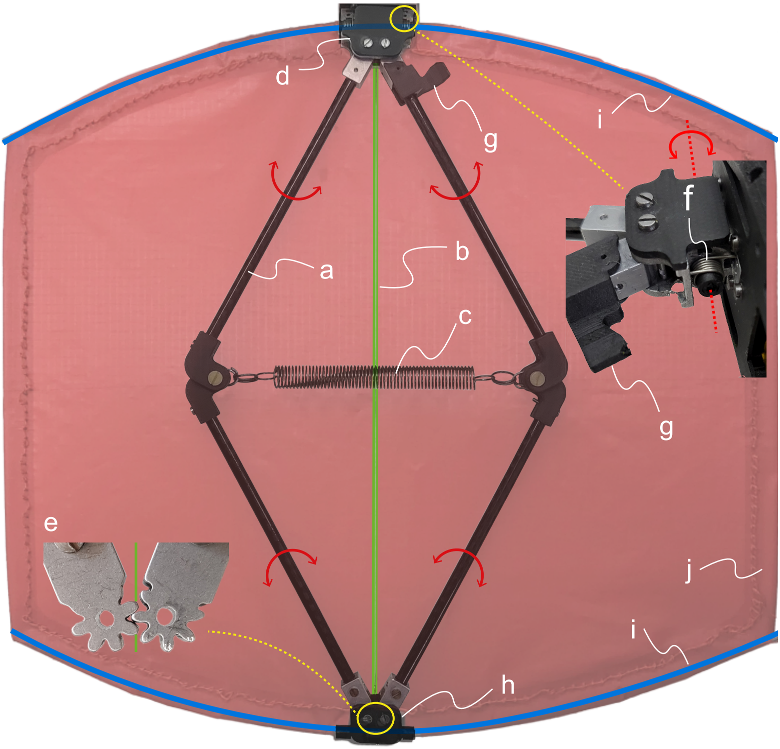

Figure 1.9.: Jumping-gliding mechanism. a. four-bar mechanism consisting of carbon pipe and 3D printed rotational joints, b. wire for leg compress (fishing line), c. spring to generate jumping energy, d. shoulder between the four-bar mechanism and body, e. gear connection in the four-bar mechanism for the symmetric mechanism folding, f. torsion spring at the rotating point between the mechanism and body for motion transition through wing opening, g. tongue to close the mechanism during compressing with contact with the body, h. foot, i. carbon rod to hold the wing membrane, j. wing membrane (coated ripstop nylon, Goodwinds).

Figure 1.9j, generates air drags forces for gliding. A design purpose was to minimize the necessary components by sharing the mechanism for multiple locomotions. Then, the robot profits less weight for jumping performance.

Jumping energy is generated by a spring in a four-bar mechanism, as shown in Figure 1.9. A wire is connected from the winder in the robot body to the foot (green line in Figure 1.9). Winding the wire deforms the shape of the four-bar mechanism like a compressed state in Figure 1.7 to stretch the spring and generate jumping energy. Clutch actuation releases stored energy for jumping. The mechanism deformation is symmetric based on the wire due to the gear connections at the shoulder and foot parts like Figure 1.9e. Exploded assembly views are provided in FigureC.1D-F.

An aerodynamic force for the gliding comes from a thin membrane, which is installed on the jumping mechanism through carbon rods (Figure 1.9i). The fabrication process of the membrane is depicted in FigureC.2 in AppendixC. A falling speed and initial pitch angle after the jumping determine initial drag and lifting forces with the initial angle of attack for gliding. For the transition of locomotion modes from jumping to gliding, the jumping-gliding mechanism has to be opened like the Figure 1.7e. During The mechanism opening in the middle of jumping, the membrane generates negative air drags causing jumping height reduction. For this reason, the mechanism opening for locomotion mode transition can be initiated after the robot reaches the apex of a jumping trajectory like transition strategy in previous works [13, 14, 15], however, to integrate perching after jumping, the mechanism opening has to be finished before the perching mode is started because the closed mechanism will disturb the perching by contacting with the vertical surface. In future work, we will design the membrane to minimize the air drag during the mechanism opening. The mechanism opening passively occurs by a torsion spring as shown in Figure 1.9f. For the next jumping, a tongue makes contact with the body surface to close the mechanism passively (Figure 1.9g) during the mechanism compressing.

1.2.1.3. Perching mechanism

The perching mechanism is designed to perch on vertical surfaces during dynamic motions, such as jumping or flying. The mechanism has to not only absorb the robot's energy during an approach for the minimum bouncing, which disturbs engagement, but make interlocking on rough surfaces. The mechanism is made of 3D printable viscoelastic material to absorb energy through the deformation of the material and claws to make a holding force for perching through interlocking. The mechanism also has a passive fastening mechanism inspired by the bird's leg, as seen in Figure 1.2B-D. Applied loads during leg folding for the shock-absorption (Figure 1.2C) and weight after perching (Figure 1.2D) passively fasten the claw's interlocking. Control of the loads on the wire allows engagement and detachment phases while perching. The mechanism is operated without any actuators. Chapter 2 includes descriptions of characteristics of the perching mechanism and demonstrations to integrate jumping and perching motion. An exploded assembly view is provided in FigureC.1B.

1.2.1.4. Active tail

The active tail generates control torque for the pitch orientation of the robot. The pitch control improves not only the performances of each motion, such as gliding distance through gliding angle control, but allows the robot has the best initial condition for following modes after jumping, such as perching or gliding angles. The tail rotation generates inertia forces for control torque to the robot. Furthermore, the tail can generate aerodynamic forces with an air drag area. While the inertial tail only uses inertia forces from the tail's rotation, the aerodynamic tail can use three additional sources to generate control torque, including inertia effects: airflow from the tail's rotation, airflow from the robot's moving, and external airflow. Therefore, the aerodynamic tail can use energy from the robot's locomotion and external energies to perform better than the inertia tail. Chapter 3 describes the active tail's characterization, effects of aerodynamics, and comparison of operating

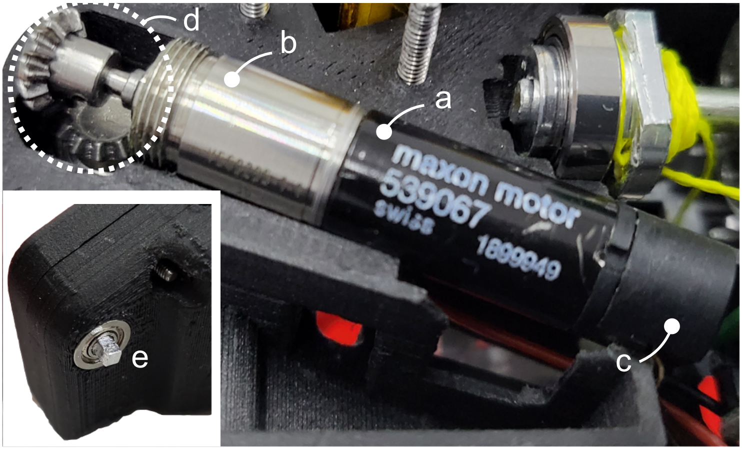

Figure 1.10.: Actuator and gear connection of the active tail. a. DC motor (347727, Maxon motor), b. gear head (474124, Maxon motor), c. encoder (334910, Maxon motor), d. bevel gear connection (gear ratio = 1:1), e. squared-shaped tail connector.

strategies.

A single-axis active tail is operated by a geared DC motor like Figure 1.10. A geared DC motor's rotational direction is changed to pitch direction through a bevel gear connection. An encoder on the motor measures the angular position of the actuator for tail control.

1.2.1.5. Electronics

The purposes of the electronic part are to provide actuator control through sensing, communication, and power supply or fully untethered operation. Although the robot has various actions, such as wing opening and perching, there are only two actuators for the jumping mechanism and the active tail to minimize the robot's weight. To operate these two actuators, the Inertia measurement unit (IMU) provides pitch orientation and inertial data, then the microcomputer unit (MCU) determines the proper tail angles for pitch control. During the jumping, the robot's pitch behavior changes flow directions. The pitch data from the IMU helps to estimate airflow directions

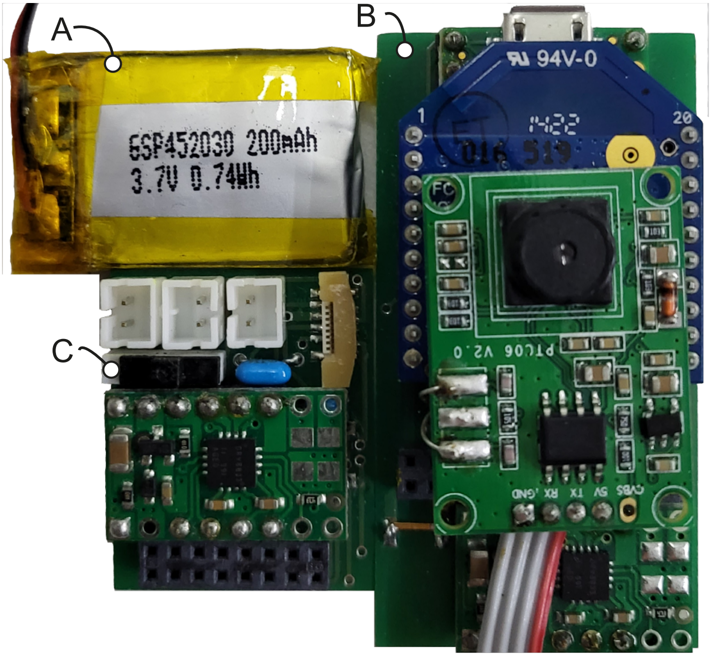

Figure 1.11.: Electronics for actuator control, sensing, power management, and communication. A. Battery (Serial connection, 3 x 3.3V 200mAh), B. main controller: microcomputer unit (Teensy3.2), Inertia measurement unit (MTI-1, Xsens), motor driver (DRV8833, Pololu), communication module (Xbee), and camera module (Miniature TTL Serial JPEG Camera, Adafruit), C. Power manager: voltage regulator (12v to 5v), motor driver (DRV8833, Pololu)

from the robot's motion, and the aerodynamic tail can use the airflow to generate more control torque. In addition, the best perching timing is when the robot reaches the top point in the jumping trajectory due to zero vertical velocity (chapter 2). The MCU can estimate the robot's vertical position from the IMU's inertia data, and calculate how to actuate the tail to make proper perching angles during the given jumping time. In addition, a camera module is another sensor to take pictures for exploring tasks, and the picture can be transferred to the user through a wireless communication module.

The picture provides information about the working environment, and users can establish an operating strategy by analyzing the picture.

As shown in Figure 1.11, the electronic part consists of two control boards, the main controller and the power manager, to integrate several components. MCU calculates and sends control signals to the motor driver according to the data of the IMU. Motor drivers provide calculated voltage according to the signals from the MCU. A wireless communication module sends the status of the robot and taken pictures to users. Both control boards consist of commercial components, and design boards integrate the components. The design process of control boards is conducted by the design software, Eagle. Appendix A depicts schematic connections between components (Figure A.1 and A.2) and Route design for arranged components (Figure A.3).

1.2.2. Equipment

This dissertation uses several equipment to measure robot behaviors, perching dynamics, and tail dynamics. Each experiment has its own set-up to generate required dynamic motions, such as inverted pendulum-like equipment to produce initial perching conditions (Figure 2.1), simplified tail rotating set-up (Figure 3.1), and elevated robot drop set-up for gliding (Figure 1.12). To measure robot behaviors with minimized contacts, measurement systems are required to minimize any disturbances to their motion. For this reason, this works mainly uses a high-speed camera and motion capture system to record dynamic motions.

1.2.2.1. Motion capture system

A motion capture system has 16 cameras to capture reflective markers in 3D space, which in volume as 3.2 m (width) x 4.8 m (height) x 5 m (length), as seen in Figure 1.12. Although we need to attach a small reflective marker on the target objects, the marker weight occupies around 5% of the overall robot weight (8 g). A sampling rate for each frame is 800Hz, which is enough to measure detailed jumping dynamics. Section E in AppendixE provides a

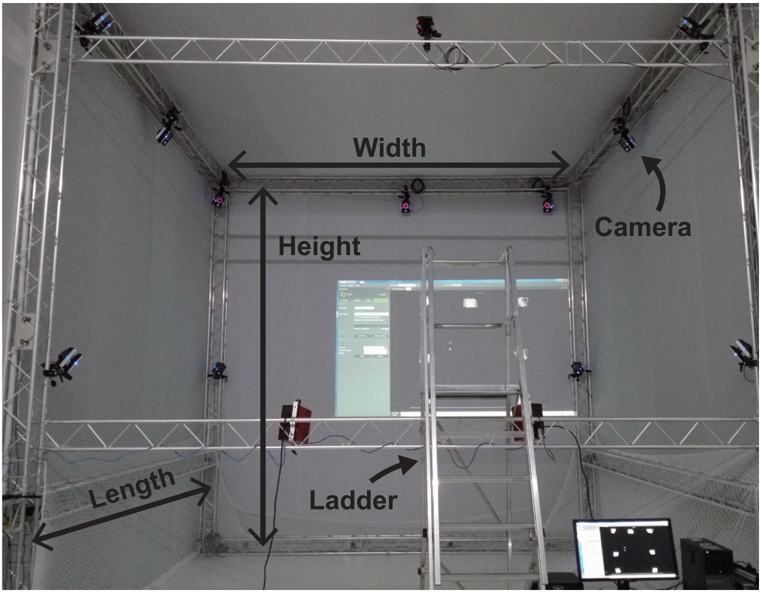

Figure 1.12.: Motion capture system (Vantage, VICON) to measure the robot's behaviors. Volume is 3.2 *m* (width) x 4.8 *m* (height) x 5 *m* (length), the system has 12 cameras, ladder provides enough height for gliding.

software set-up to use the motion capture system.

1.2.2.2. High-speed camera

A high-speed camera (Phantom v641), as seen in Figure 1.13, measures dynamic motion with a higher frame than the motion capture systems. For this reason, the high-speed camera is used to measure highly dynamic motions, such as perching and tail rotation. The camera does not require any contact for measurements, however there are accuracy issues with camera lens distortion, which is hard to compensate. For this reason, this work records very limited area to minimize the distortion. The sampling rate for each recording frame is 1400 Hz. Section E in AppendixE provides software set-up to use the high-speed camera for each experiment.

Figure 1.13.: High-speed camera to observe detailed behavior of the robot. a camera body (V641, PHANTOM), b. lens, c. Memory, d. tripod

1.2.3. Estimation of coefficient

1.2.3.1. Air drag coefficient

This work includes some simulations of aerodynamics with a thin film, therefor accurate drag coefficient of the thin film is necessary. The film, coated ripstop nylon, was selected because it has characteristics of high durability and low mass (Goodwinds, 0.75 oz). Although we can easily find the drag coefficient of rectangular-shaped thin films, the coefficient can be changed according to the applied film's material. For this reason, this section estimates the drag coefficient of the selected film.

Figure 1.14 introduces a built wind tunnel. the wind tunnel has a fan to generate target air flow speed ,0-6 m/s, flow straighter for laminar flow, air flow sensor measures flow speed for feedback control; a loadcell measures air drag forces. The drag coefficient of the tail, C_d, can be estimated by measured drag forces, F_D, through the definition as follow:

$$C_d = 2\frac{F_D}{\rho A_{drag}(v_{flow})^2}, \tag{1.1}$$

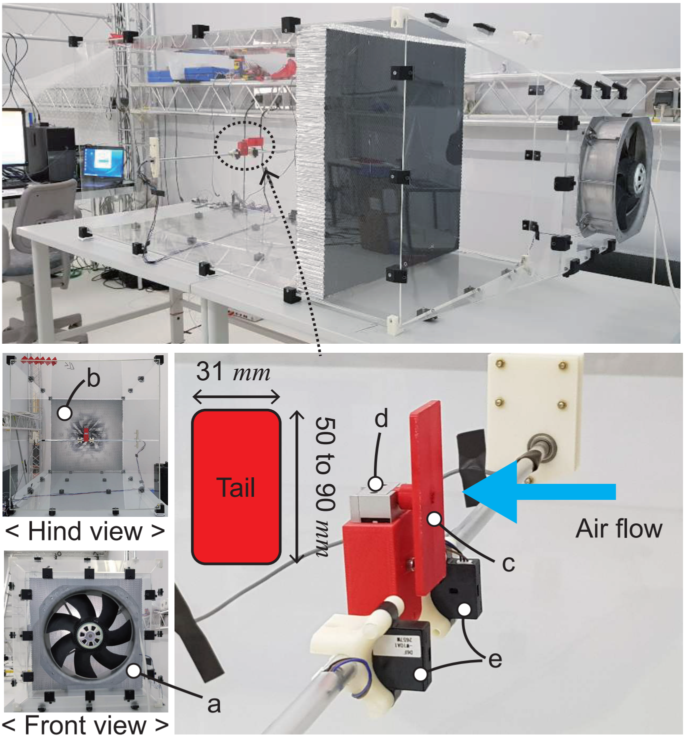

Figure 1.14.: Wind tunnel to measure the Air drag coefficient of the thin film. The size of the tunnel is 0.7 x 0.7 x 2.1 m, and the distance between the measuring target and flow straighter is 70 cm: a. Fan to generate airflow, b. flow straighter to make the laminar flow, c. tail with a thin film, The width of the tail is fixed as the maximum length as 31 mm, d. load cell to measure the air drag forces (GS0-25, Transducer techniques), e. flow sensor to measure flow speeds (D6F-W10A1, Omron), The measured flow speeds provide feedback data to control the fan speed, Airflow (Blue arrow) is always perpendicular to the tail's surface.

where ρ is the density of the air at room temperature, A_{drag} is the plane area for the aerodynamic forces, v_{flow} is the flows speed. To estimate the accurate drag coefficient, the measurements were performed by varied flow speeds, as 2, 3, and 4 m/s, and tail length, 50 to 90 mm. Figure 1.15A provides measured drag forces, and Figure 1.15B shows the estimated drag coefficient as 1.1219.

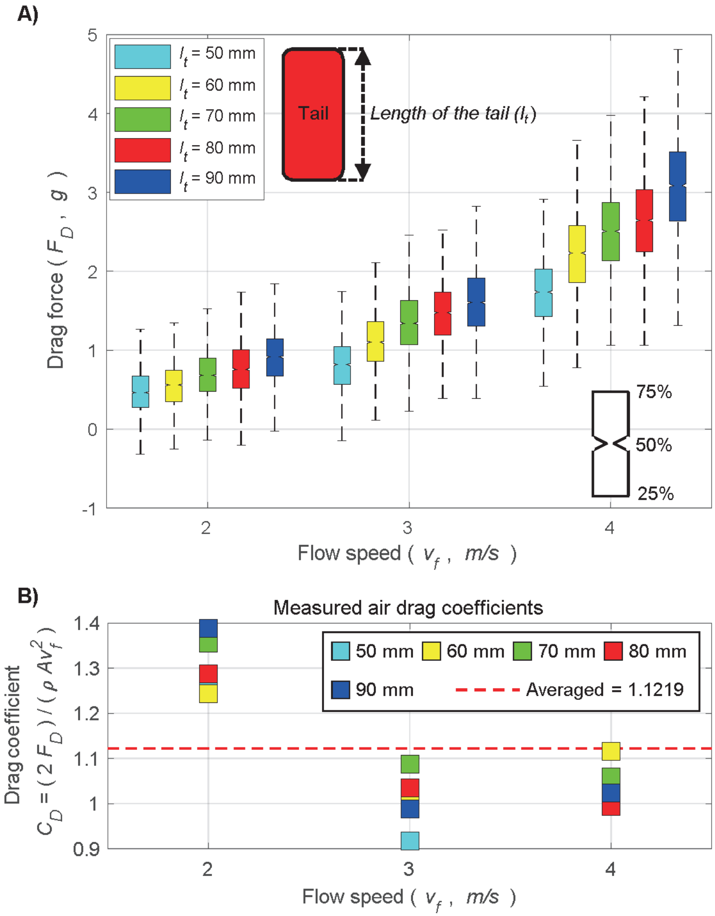

Figure 1.15.: Estimation of the air drag coefficient: A) Measured forces according to different flow speeds and tail lengths. The averaged data was captured for 1000 seconds. B) Calculated air drag coefficient of the tail. Averaged coefficient is 1.1219.

1.2.3.2. Affected spring stiffness

A spring provides jumping energy and determines overall jumping behaviors. All scenario for multimodal locomotion starts from jumping, as seen in Figures 1.5 and 1.6; therefore, an estimation of the spring stiffness is necessary to predict jumping height and distance. The spring is installed in the jumping mechanism, which is the four-bar mechanism. For this reason, the estimated spring stiffness includes effects from the four-bar mechanism, such as friction of the mechanism's rotational joint. The estimation is conducted by a dynamic model of the jumping motion and measured jumping behaviors. The robot has seven components: the body, leg mechanism, and tail, as seen in Figure 1.16.

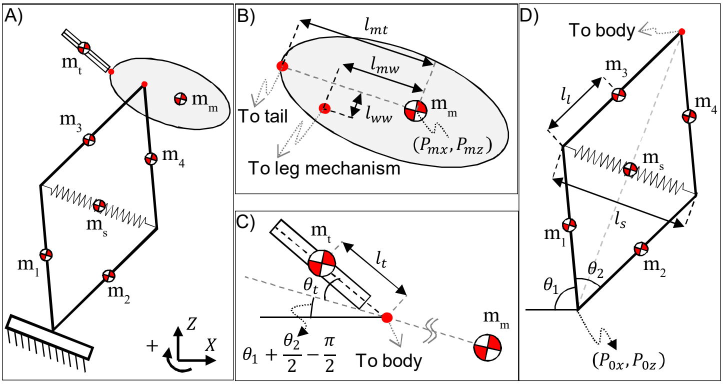

Figure 1.16.: Schematic view of the dynamic model of the jumping robot: A) Overall structure and the coordinate system (m_1 and m_2 are 6.65 g. m_3 and m_4 are 8.15 g. m_s is 6.2 g. m_m is 103.5 g). B) Body. (l_{mt}, 47.3 mm, is a length between the body's center of mass and connecting point with the tail, l_{mw} and l_{ww} are lengths between the body's center of mass and connecting point with the leg mechanism, and they are 8.16 mm and 9.5 mm, respectively). C) Tail (l_t is length of the tail, which is the design parameter for optimization in future work). D) Leg mechanism (l_l, 67 mm, is a half-length of a leg, l_s is the length of the spring, Non-extended length of the spring, l_i, is 98 mm).

The dynamic model can be defined by the Lagrangian method. To calculate the energies, we need to define a position, $\vec{P}_i$, and velocity, $\dot{\vec{P}}_i$, vectors for each body from an origin point (P_{0x}, P_{0z}). Then, we can calculate the kinetic, KE_i, and potential, PE_i, spring's potential, PE_s, energies and Lagrangian form as follows:

$$\begin{aligned}
&KE_i = 0.5m_i(\vec{P_i} \cdot \vec{P_i}) + 0.5I_i\dot{\theta_i}^2, \\
&PE_i = m_i g\vec{p_{iz}}, \\
&PE_s = 0.5(l_s - l_i)^2, \\
&L = \sum KE_i - \sum PE_i,
\end{aligned} \tag{1.2}$$

where i is the number of the bodies. m_i is the mass, I_i is the moment of inertia, θ_i is the angle, g is gravitational acceleration, 9.8 m/s, P_{iz} is the position of mass center in Z axis. We use two kinds of models to describe the jumping motion. The first one is before the lift-off. The model assumes that a revolute joint connects the robot's foot with the ground to remove a slip between the foot and the ground. We can calculate the motions of all bodies before the lift-off with three variables: θ_1, θ_2, and θ_t. A model after the lift-off does not have any connection with the ground. The model can describe the behaviors of the robot in the air. After the lift-off, we can calculate the motions in the model with five variables: θ_1, θ_2, θ_t, P_{0x}, and P_{0z}. We can derive dynamic models with external torques, $\tau_{ex,i}$, as follows:

$$\frac{d}{dt}\left(\frac{\partial L}{\partial \dot{\theta_i}}\right) - \frac{\partial L}{\partial \theta_i} = \tau_{ex,i} \tag{1.3}$$

As a result, a matrix form of the dynamic models before and after the lift-off can be expressed as follows:

$$M_I[\ddot{\theta}] + M_{CE}[\dot{\theta}^2] + M_{CO}[\dot{\theta}\dot{\theta}] + M_G = M_{EX} \tag{1.4}$$

where M_I, M_{CE}, M_{CO}, M_G, and M_{EX} are matrices for a body's inertia, centrifugal forces, Coriolis force, gravity, and external torques, respectively. Calculating the dynamic equations for the multiple components is challenging because of the huge equation lengths. For this reason, I developed a code to derive dynamic equations easily through Lagrangian equations, as provided in SectionD of Appendix D. In addition, the code rearranges the dynamic equation into matrix form. Matrices for the inertia, centrifugal force, and Coriolis force can be calculated by specifications of the robot. However, the matrix for the external torques requires the spring coefficient. We estimate the affected spring coefficients to define the external force matrix by using the measured jumping behaviors and the dynamic model. The dynamic model for the estimation does not have a tail.

We can differentiate the jumping motion into two regions like Figure 1.17A. The robot starts to jump with a fully compressed leg mechanism and has the maximum elastic energy from the spring. The clutch mechanism inside the robot boy released the stored elastic energy to initiate the jumping. Region I depicts the pitch behavior of the robot before the lift-off. The body leans in pitch direction due to the distance between the mass center of the body and connecting point of the jumping mechanism. When the body's momentum is enough to lift the whole robot's weight, the robot lifts off from the ground. Region II depicts behaviors after the lift-off. After the lift-off, there are other effects, such as spring fluctuation, as depicted in Figure 1.17B. For this reason, the pitch angles in Figure 1.17A fluctuate initially and determine overall pitch behavior during the jumping. As a result, to avoid other effects, this work estimates the spring stiffness from the robot behaviors of region I, and the affected spring stiffness, K^* can be defined by rearranging the equation 1.2.3.2 as follows:

$$K^* = \left(\frac{d}{dt}\left(\frac{\partial L}{\partial \dot{\theta}_2}\right) - \frac{\partial L}{\partial \theta_2}\right)\frac{1}{C_k} \tag{1.5}$$

where C_k is a constant to define the applied torque from the spring forces. Figure 1.18 indicates the estimated spring stiffness according to the θ_2. The θ_2 at the fully compressed leg is 180 degrees. The robot uses a four-bar mechanism as a jumping mechanism, and the mechanism has a singular point. An inside graph of Figure 1.18 depicts the angular velocity of the

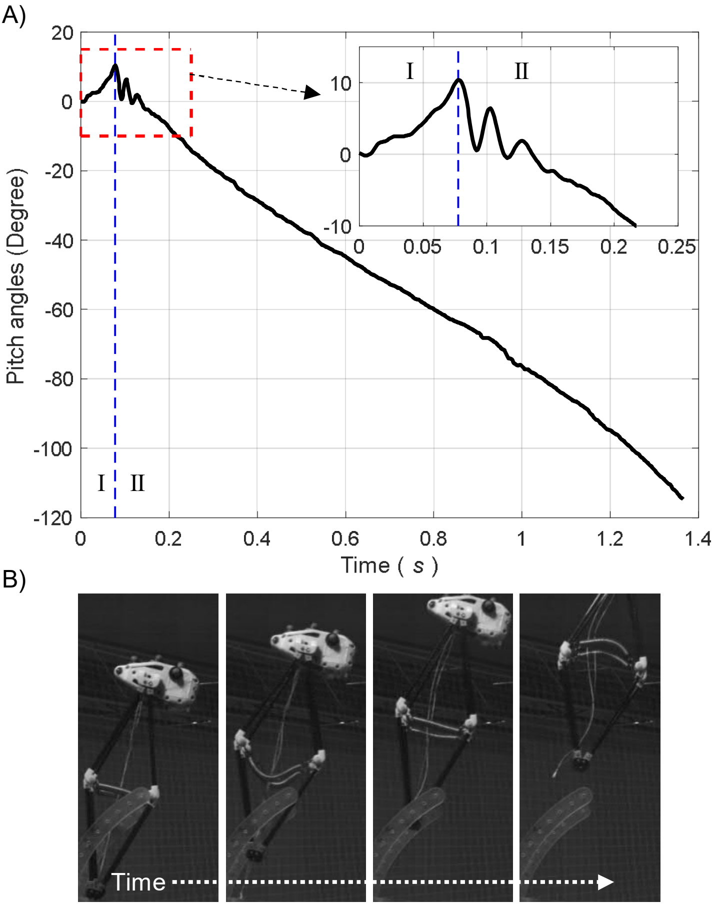

Figure 1.17.: Jumping behavior: A. differentiated regions during the jumping. regions, I and II, show Robot's behaviors before and after the lift-off. B. Spring fluctuation during jumping.

θ_2. The angular velocity is initially increased in the negative direction. However, the angular velocities are in the positive area due to the singularity. Therefore, we exclude the data before 150 degrees to average the estimated effective stiffness. As a result, an estimated effective stiffness is 146.33 N/m.

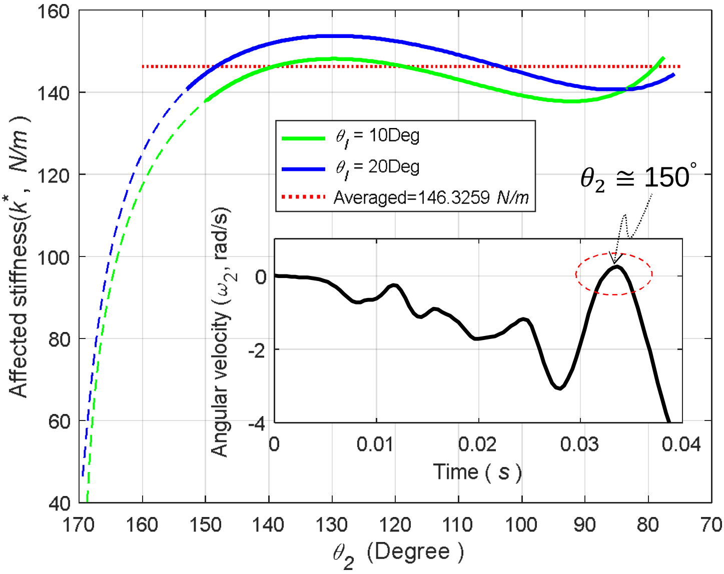

Figure 1.18.: Estimated affected spring stiffness. A red circle indicates the singularity point, θ_2 is around 150 degrees. Averaged stiffness after the singularity point, which is solid blue and green lines, is 146.33 N/m.

Chapter 2

Avian-Inspired Perching Mechanism for Jumping Robots

H Kim, M A Woodward, M Sitti, "Avian-Inspired Perching Mechanism for Jumping Robots", Advanced Intelligent Systems, 2022, Submitted [83]

The integration of multiple locomotion strategies and behaviors allows robots to extend the working environment and enhance the performance of each motion. This chapter integrates perching with a jumping robot to improve the jumping performance. The developed avian-inspired perching device has a shock-absorbing mechanism, which consists of a 3D printable flexible polymer material that absorbs the perching impact. This chapter characterizes the shock-absorbing performance of the viscoelastic material as a function of hardness and thickness of the material, initial angles of a mechanism, mechanism length, perching speed, and perching angle. This chapter also characterizes the performance of mechanical interlocking and penetration as the engagement strategies for vertical surfaces. This chapter observes the performance of perching mechanism as a function of hardness of the target surface, contact angle of the claw, and performance of the shock absorption. Finally, this chapter conduct demonstrations to evaluate the perching mechanism's performance on the complete system, and to show the robot's performance enhancement with an integrated perching motion. This chapter provides a design methodology to develop and integrate a perching mechanism into jumping robots. Prof. Matthew A. Woodward and Prof. Metin Sitti contributed to the discussions and edited the manuscript. The results of this chapter are reported from [83].

2.1. Method

2.1.1. Shock-absorbing mechanism

As perching typically occurs during flying or jumping, the robot has a surface approach speed before perching. The approaching speed generates a perching shock and can cause engagement failures if the mechanism cannot absorb the perching shock properly. One option explored in previous works, has been dynamic motion control during perching to minimize the perching shock [17, 110]; where, orientation and approach speed control while perching can also be observed in birds [111]. However, these strategies do not tend to remove all the impact energy during perching. Therefore, a shock-absorbing mechanism becomes necessary. Hydraulic compression [112] has been one of the methods studied to absorb energy. Energy from the perching shock compresses the fluid in the mechanism which consumes the energy. Movement of the center of mass while perching has also been explored as a means of absorbing energy during perching [16]. Finally, viscoelastic materials have been employed to absorb energy as they deform [113, 114, 115] and provide a simple yet robust mechanism for perching energy absorption.

This chapter studies the viscoelastic material, digitalized 3D printing rubber-like material, as a passive shock-absorbing mechanism. The mechanism is integrated at the front side of the robot like Figure 2.1. Because polyjet 3D printing provides modifiability of the digitalized materials (Figure 2.1C), we can easily vary material properties, such as hardness and angle, for the characterization of the shock-absorbing performance. The characterization is also performed for other design parameters, such as the number of the shock-absorbing material and the length of the leg, and initial perching conditions, such as initial angle and speed. As a result, this characterization provides the design parameter's effects on shock-absorbing performances; in addition, 3D printable material provides advantages of ease and simplicity for producing the shock-absorbing material.

Figure 2.1 depicts the experimental setup to characterize the shock-absorbing performance of the mechanism. The pendulum-like equipment is able to precisely set the perching speed and pitch angle as seen in Figure 2.1A. The experimental procedure is as follows. I initially lift the rotatable rod to a specific height manually to set the potential energy, then let it rotate freely to transform the potential energy into kinetic energy. A quick-release mechanism is attached at the end of the rod (Figure 2.1B), which releases the robot at a target speed. We can change the target speed by changing the initial potential energy. The trigger point is determined by a wire length connected between the quick-release mechanism and equipment frame. In this case, the robot is released at the horizontal position, yielding only horizontal kinetic energy. Figure 2.1C shows the foldable leg part, which is a viscoelastic digital material. As the robot contacts the surface, the inertia of

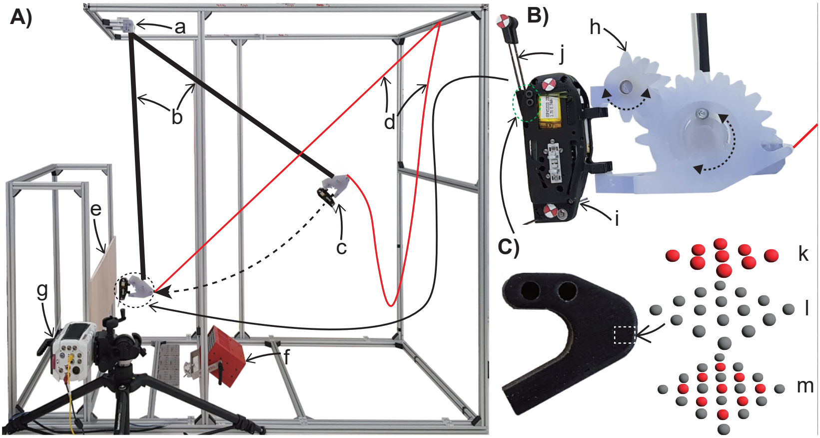

Figure 2.1.: Experimental setup and method to characterize the shock-absorbing performance of the viscoelastic digital material. A) Pendulum-like setup to generate a perching motion (a. rotational joint, b. rod to connect the rotational joint and quick release mechanism, c. quick-release mechanism, d. wire to trigger the quick release mechanism, e. target surface (flat timber plate), f. light for high-speed recording, g. high-speed camera). B) Detailed view of the quick-release mechanism (h. quick-release mechanism, if the wire triggers the mechanism, upper and lower holders open together to minimize an interaction to robot's behaviors, i. robot body, j. perching mechanism; the foot part is replaced as a circular tip to minimize effects from the foot contact with surfaces). C) Viscoelastic 3D-printed material part of the leg (k. UV curable flexible material (TnagoBlackPlus, Stratasys), l. UV curable solid material (VeroBlackPlus, Stratasys), m. digital material structure).

the robot's body and reaction force folds the leg and deforms the viscoelastic material, absorbing or consuming the impact energy.

Figure 2.2 depicts the overall impact process. The leg folding not only absorbs the overall energy (E_O) but transforms some of the energy into pitch (E_P) and vertical (E_V) energies. This is characterized as the first absorption. At the point where the robot's body hits the surface the second absorption phase begins. The new reaction force compensates for the energies generated by the first absorption causing the robot to pitch towards the surface, which creates additional leg folding and additional energy absorption. The body impact also absorbs energy by dispersing it throughout the body structure.

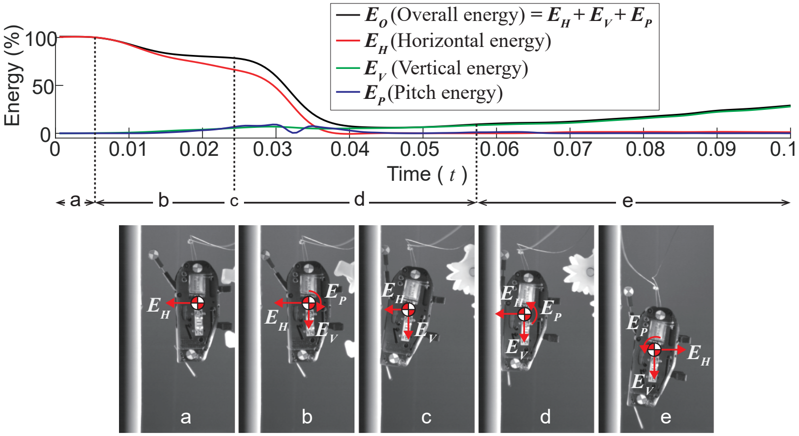

Figure 2.2.: Energy changes during perching (a. approaching, b. first absorption, c. body hitting between the first and second absorption, d. second absorption, e. behavior after shock absorption).

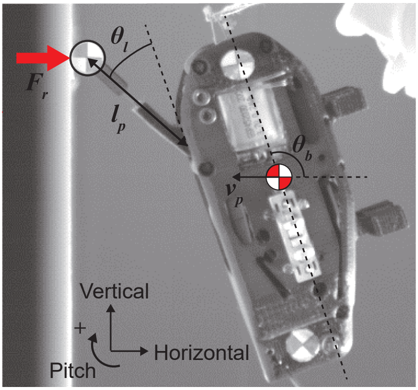

Figure 2.3.: Parameters for the perching motion shown on the robot side-view photo.

The second absorption ends as the foot leaves the surface, and any remaining energy must eventually be absorbed by the attachment mechanism itself.

A high-speed camera recorded the whole impact process and took the position data to calculate energy changes of the body and foot contact stability. To calculate the pure shock-absorbing performances of the leg, I only consider the first absorption before the body hitting has occurred. Then, the absorbed energy of the body is calculated as follows:

$$\begin{aligned} KE &= \frac{1}{2}m_b v_b^2 + \frac{1}{2}I_b \omega_b^2, \\ E_{ab} &= \frac{KE_i - KE_t}{KE_i}, \end{aligned} \tag{2.1}$$

where KE is a measured kinetic energy of the body's center of mass, m_b is the mass of the body, v_b is the linear velocity of the body, I_b is the body's moment of inertia in the pitch direction, ω_p is the angular velocity of the body in pitch direction, E_{ab} is the absorbed energy, KE_i is kinetic energy at the foot's first contact with surfaces, and KE_t is kinetic energy after the first or second absorptions. Foot contact stability is also an essential factor in successful perching. If the foot can stay in contact with the surface during the entire impact process, the claws will have more opportunity for engagement than if the foot is bouncing off the surface. I observed the foot's contact behavior from the recorded videos and determined the foot's contact stability.

For the characterization, I measured the shock-absorbing performance under different conditions. Figure 2.3 depicts the parameters used to determine the perching performance. The design parameters were the leg angle, θ_l, hardness of the leg material, leg length, l_p, and the number of legs. The initial conditions for perching were approaching angle, θ_p, and speed, v_p. We could easily change the leg angle and hardness during the polyjet 3D printing and vary the approaching angle and speed in the experimental setup.

2.1.2. Engagement mechanism

Perching is achieved by attachment to a target high surface. This chapter studied the performance of mechanical interlocking and penetration as engagement methods through the use of claws. The surface parameters, such as surface roughness and hardness, are important in determining the performance of the engagement. The surface roughness is one of the essential factors for mechanical interlocking. For example, birds and insects have claws and hairs on their feet to increase the chance of mechanical interlocks with rough surfaces, which have been studied by roboticists [116, 117, 118, 119, 84, 120]. The hardness of a target surface is another important factor in interlocking through penetration. Regardless of the surface's roughness, a sharp end-tip can penetrate the soft surface to make an engagement [121, 122]. This chapter covers the characterization of mechanical interlocking performance of the developed mechanism but also includes additional studies on the performance changes with penetration. Interlocking through penetration is more robust than without the penetration, as asperities are not necessary. As a result, we can strategically use the penetration according to the surface's hardness and enhance the engagement's success rate.

Figure 2.4 depicts parameters for the engagement. A design parameter is the claw angle calculated as follows:

$$\theta_c = 90 - (\theta_b + \theta_l + \theta_f)(degree), \tag{2.2}$$

where θ_c is the claw angle of the claw, θ_l is a leg angle, and θ_f is a foot angle which is fixed at 40 degrees; leg angles are varied to vary the claw angle. Experiments were then conducted to characterize the performance changes of the engagement according to the claw angle. Additionally, performance changes according to shock-absorbing performance were also experimentally characterized by varying the leg angle and hardness together. Surface roughness is another parameter in determining the engagement performance. While engagement methods, such as adhesion [43] or suction [123] prefer a flat surface, mechanical interlocking requires rough surfaces to have abundant asperities for interlocking. Tree bark was selected as the rough

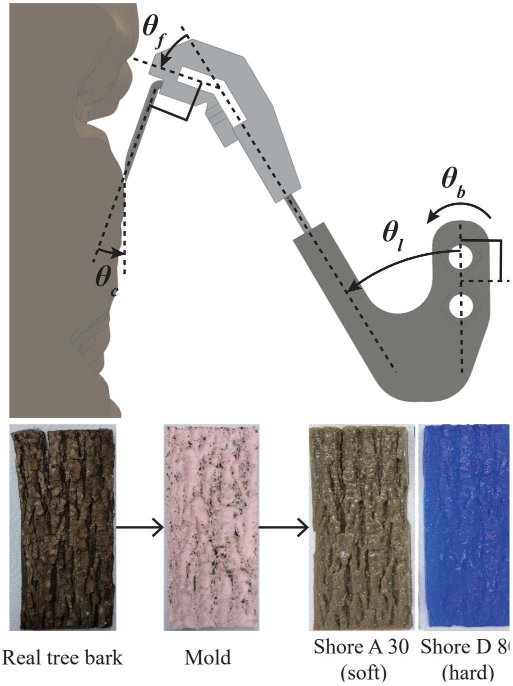

Figure 2.4.: Parameters for the engagement through the mechanical interlocking and penetrating.

surface. The engagement characterization was conducted not only on real tree bark, but also on the same duplicated pattern with harder (Shore D 80, safety helmet) and softer (Shore A 30, rubber) materials as shown in Figure 2.4. Varying the hardness of the surface highlights the penetration affects on interlocking and perching performance.

2.1.3. Passive fastening mechanism

In addition to the claws themselves, the foot structure is also able to passively enhance its grip on the surface. This is achieved through the incorporation of a cable which curls the foot under an applied load, as shown in Figure 1.2

C,D. Therefore, the weight of the robot and leg folding will result in further curling of the claw, while subsequent jumping reduces this force, allowing it to more easily release.

2.2. Results

2.2.1. Shock-absorbing performance

This section characterizes the shock-absorbing performance by varying the leg design parameters and perching conditions; these include the leg material hardness, leg angle, leg length, number of legs, perching angle, and perching speed. Figures 2.5, 2.6, 2.7, 2.8, and 2.9 show the change in the energy according to different conditions during the impact process divided into the first and second absorptions.

2.2.1.1. First absorption

The leg folding not only transforms initial horizontal energy into pitch and vertical energies but absorbs energy through the deformation of the viscoelastic material (Figure 2.5, left of the dotted line). At the end of the first absorption the body makes contact with the surface, this is the starting point of the second absorption.

Energy absorption of the leg is determined by the characteristics of the leg: the hardness, Figure 2.5 (rows), leg angle, Figure 2.5 (columns), number of legs, Figure 2.6, and mechanism length, Figure 2.7. Multiple legs and stiffer material increase the stiffness of the shock-absorbing mechanism and thus shortens the time for energy reduction. However, stiffening the digital material results in changes to the material's micro-structure and thus properties while doubling the leg increases stiffness through the addition of more material with the same micro-structure and properties (left to right in Figure 2.5 and Figure 2.6). Large leg angles provide folding space, which increases the shock-absorbing time and changes energy absorption (top to bottom in Figure 2.5). The length of the mechanism also plays a significant

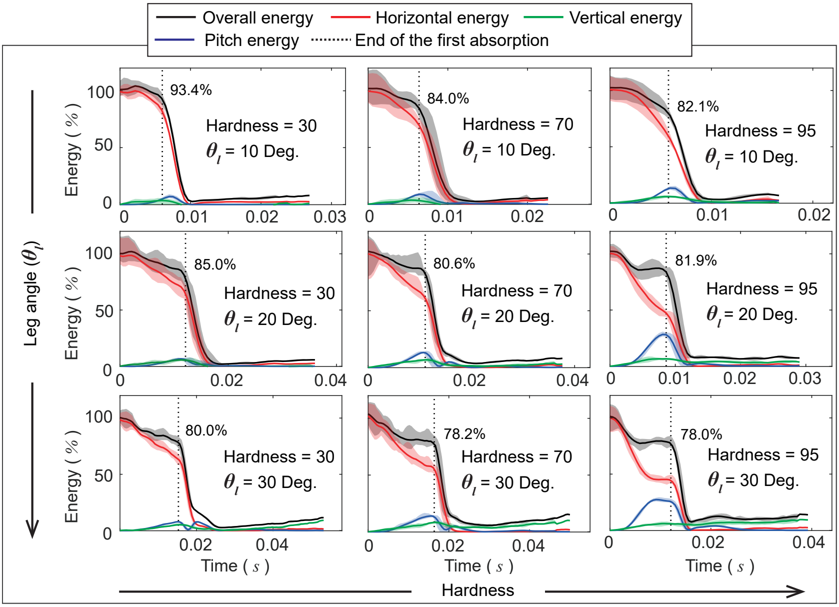

Figure 2.5.: Measured shock-absorbing performance and energy changes of the body according to the leg properties during the entire impact process, the foot firstly contacts to the surface at zero second, The results are with the perching speed and angle of 1.5 m/s and 0 degrees, respectively, All results are averaged from 10 trials. robots have double legs and mechanism length of 40 mm.

role in determining the absorption time. As longer leg lengths increase the absorption time due to the body's increased distance from the surface at the point of contact, this also results in increased time for gravity to accelerate the robot vertically (Figure 2.7). At the initial point of contact, the robot has a set amount of kinetic energy that must eventually be absorbed for a successful perch. The first absorption time varies with the leg parameters. As a result, the ideal shock absorbing behavior is where these parameters are varied such that the leg folding is terminated at the onset of the second absorption (body contact) to avoid over or under folding designs. Although the presented results show hard material (Shore A hardness = 95) and large leg angle (θ_l = 30 degrees) absorb the most energy, early termination of

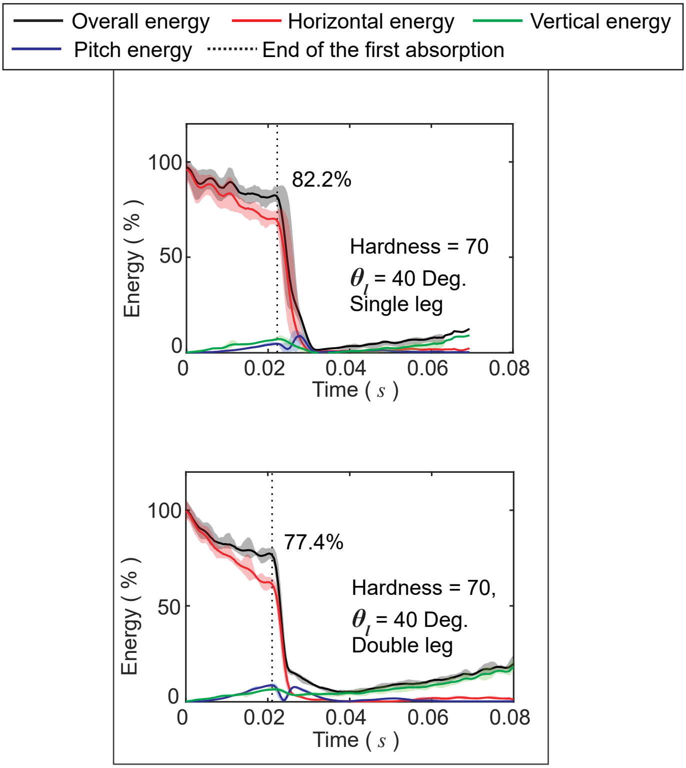

Figure 2.6.: Measured shock-absorbing performance and energy changes of the body according to the number of legs during the entire impact process, the foot firstly contacts to the surface at zero second, The results are with the perching speed and angle of 1.5 m/s and 0 degrees, respectively, All results are averaged from 10 trials, the mechanism length is 40 mm, and the leg material properties are Shore A hardness of 30 and leg angle of 30 degrees.

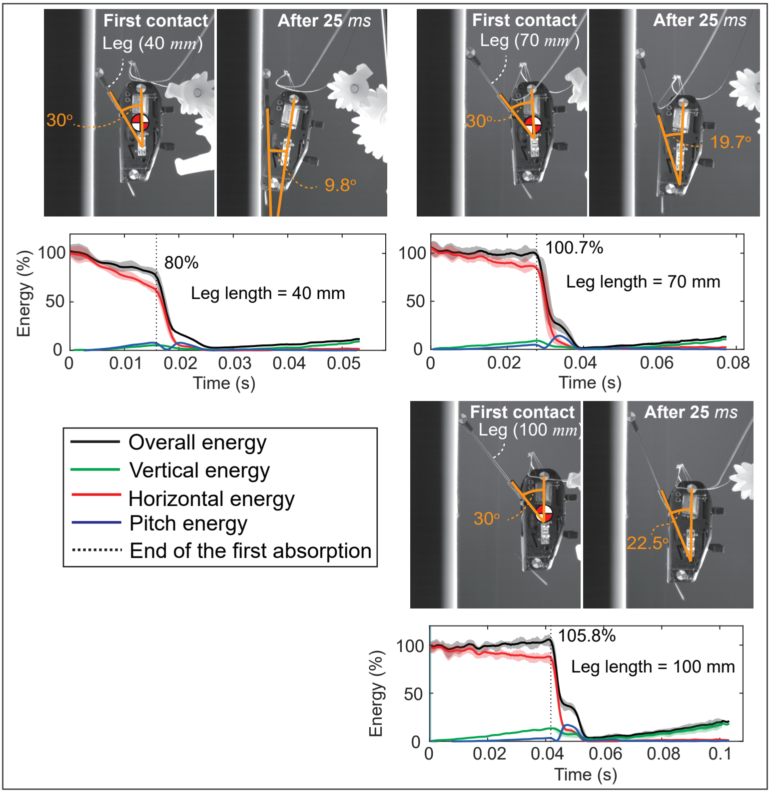

Figure 2.7.: Measured shock-absorbing performance and energy changes of the body according to the mechanism length during the entire impact process, the foot firstly contacts to the surface at zero second, The results are with the perching speed and angle of 1.5 m/s and 0 degrees, respectively, All results are averaged from 10 trials, the robots have double legs, and the leg material properties are Shore A hardness of 30 and leg angle of 30 degrees.

the leg folding causes loss of adaptation ability for the body's behavior and unstable foot contact with the surface (section 2.2.2.1). Because the leg folding behaviors can be changed by the perching conditions and interaction between the claw and surface, I provide the best parameters for our system in section 2.2.2.2.

The first absorption time and shock-absorbing behaviors are also affected by the initial conditions: perching angle, Figure 2.8 and perching speed, Figure 2.9. The perching angle defines the folding torques, τ_f from the reaction force of the surface, F_r :

$$\tau_f = F_f l_p + F_{fr} l_p sin(\theta_b - 90 + \theta_l), \tag{2.3}$$

where F_f is the tangential force and F_{fr} is the frictional force. Angled perching, having both vertical and horizontal inertial components, generates more folding torque as the friction between the foot and surface cause by sliding down the surface, add to the total folding torque, and therefore increases leg folding. As shown in Figure 2.8, folding angles after the same time (25 ms) increase with angled perching. However, excessive perching angle (Perching angle = 30 degree in Figure 2.8) transforms most of the reaction force from the surface to axial forces, F_a, causing less leg folding. Although energy absorption through the axial force is possible due to the deformation of viscoelastic material in the axial direction and energy dispersion in the whole body, this work only considers the leg folding as a shock-absorbing strategy during the first absorption. Angled perching has a longer impact time due to the body's increased distance from the surface, which causes early termination of the leg folding and unstable foot contact stability (section 2.2.2.1). If we consider the foot contact stability necessary for successful perching, the optimal scenario therefore being perching angles of close to zero degrees, and we can vary other parameters to get the desired shock-absorbing performance.

The perching speed directly affects the energy that must be absorbed (Figure 2.9); however the perching speed is determined by the robot's locomotion characteristics. Ideally, the locomotion could be adjusted such

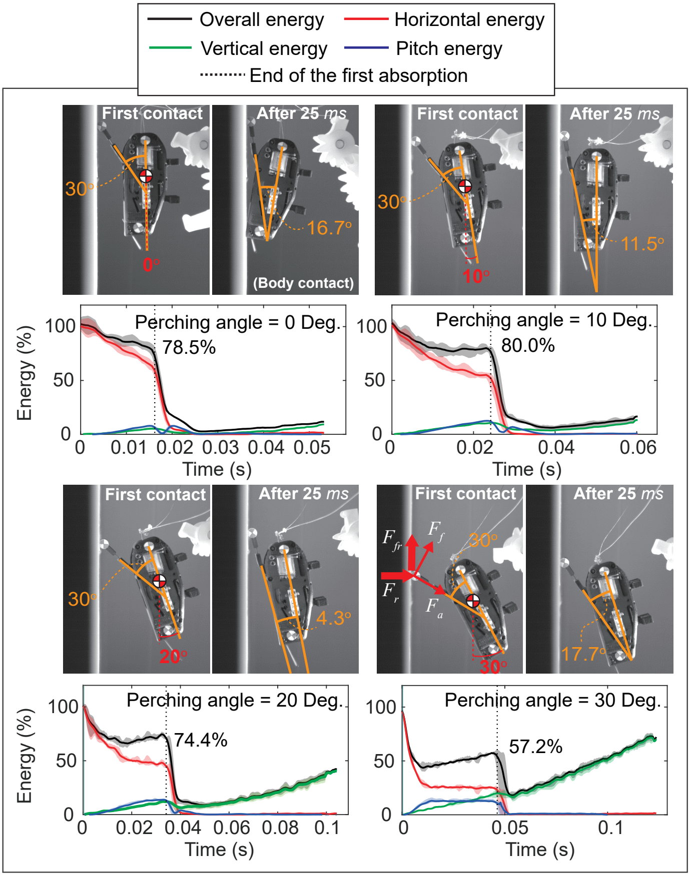

Figure 2.8.: Measured shock-absorbing performance and energy changes according to the perching angle during the entire impact process, the foot firstly contacts to the surface at zero second, The results are with mechanism properties as double legs, Shore A hardness of 30, leg angle of 30 degrees, and mechanism length of 40 mm, All results are averaged from 10 trials, F_r is reaction force from the surface, F_f is folding force, F_a is axial force, and the perching speed is 1.5 m/s.

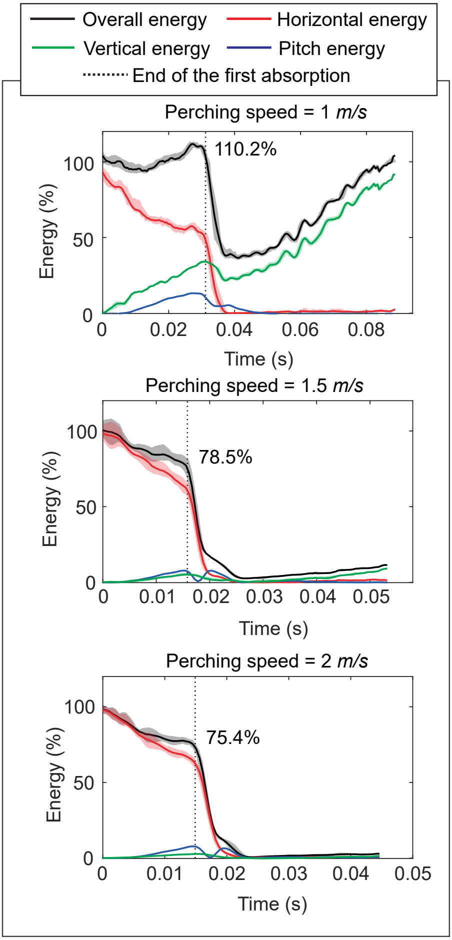

Figure 2.9.: Measured shock-absorbing performance and energy changes according to the perching speed during the entire impact process, the foot firstly contacts to the surface at zero second, The results are with mechanism properties as double legs, Shore A hardness of 30, leg angle of 30 degrees, and mechanism length of 40 *mm*, All results are averaged from 10 trials, the perching angle is 0 degrees.

that at the perching position, the velocity would be minimized; in this case, at the top of the jump the robot is moving at 1.5 m/s horizontally. Since the absorption time determines the amount of kinetic energy added due to gravitational acceleration, lower than expected speeds can greatly increase absorption time. This therefore results in overall lower performance energy absorption. While higher speeds do not increase absorption time, the mechanism's absorption saturates quickly, absorbing a small percentage of the total energy of the system.

2.2.1.2. Second absorption

After the first absorption, there is a second chance to fold the leg for further shock absorption (Figure 2.2 d). As the first absorption create a pitching moment away from the surface, the second absorption must compensate for this pitch energy as well as the remaining translational energy. The body's impact with the surface is used to change the pitch direction (item c in Figure 2.2); however, alternative options, such as a tail [124], have been explored by others. During the second absorption, the remaining energy is absorbed by not only the body making contact with the surface, dispersing the energy throughout the body structure and additional appendages, but through a secondary leg folding, due to the change in the pitch direction. As a result, we can strategically use the second absorption to maximize the shock-absorbing performances. Figures 2.5 and 2.8 show dramatic reduction of body's kinetic energy during the second absorption.

2.2.2. Engagement performance

2.2.2.1. Foot contact stability

Figure 2.10, 2.11, and 2.12 present the results of the foot contact stability tests. Over-folding, Figure 2.10A, and under-folding, Figure 2.10B, can both be observed to cause loss of foot contact due to bouncing; however, the bouncing characteristics are unique to each scenario. Bouncing in the former is due to bottoming out of the mechanism and is more localized in

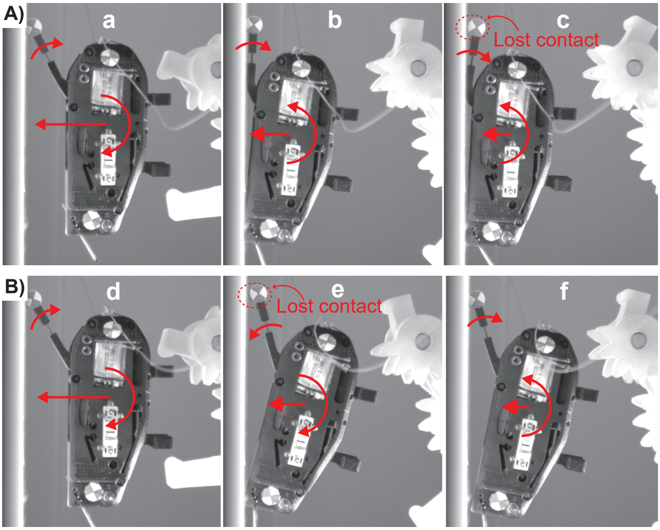

Figure 2.10.: Foot contact stability. A) Unstable foot contacts due to the over-fold issue of the leg: a. first foot contact to the surface, b. end of the first absorption, c. lost of a foot contact from the surface due to the over-fold of the leg. B) Unstable foot contact due to the under-fold issue of the leg: d. first foot contact to the surface, e. lost foot contact from the surface due to the under-fold of the leg, f. second foot contact during the second absorption.

the arm itself, while the latter transfers significant energy into pitch which must be absorbed during body contact (second absorption). The leg angle is the most significant parameter for foot stability when perching, as shown in Figure 2.11. For a robot expected to perch around 1.5 m/s, a leg angle of 10 degrees shows normal folding behavior across nearly all tested material hardness. However, as the perching angle changes the foot contact stability rapidly decreases, as can be seen in Fig 2.12, where the softer material shows the best performance as it is able to better handle the misalignment. In the case of the presented prototype the best design for foot contact stability is a leg angle of 10 degrees and a shore A hardness of 30, allowing for perching speeds between of 1 to 2 m/s and perching angles of 0 to $+10$ degrees. However, we also need to consider the shock-absorbing and interlocking

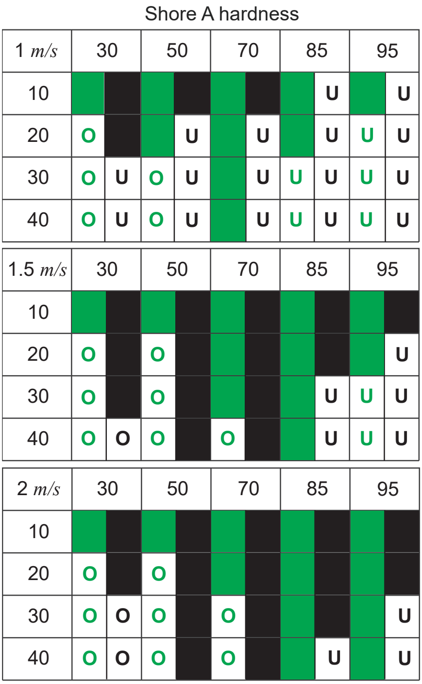

Shore A hardness

1 *m/s*	30		50		70		85		95	
10	🟩	⬛	🟩	⬛	🟩	⬛	🟩	U	🟩	U
20	O	⬛	🟩	U	🟩	U	🟩	U	U	U
30	O	U	O	U	🟩	U	U	U	U	U
40	O	U	O	U	🟩	U	U	U	U	U

1.5 *m/s*	30		50		70		85		95	
10	🟩	⬛	🟩	⬛	🟩	⬛	🟩	⬛	🟩	⬛
20	O	⬛	O	⬛	🟩	⬛	🟩	⬛	🟩	U
30	O	⬛	O	⬛	🟩	⬛	🟩	U	U	U
40	O	O	O	⬛	O	⬛	🟩	U	U	U

2 *m/s*	30		50		70		85		95	
10	🟩	⬛	🟩	⬛	🟩	⬛	🟩	⬛	🟩	⬛
20	O	⬛	O	⬛	🟩	⬛	🟩	⬛	🟩	⬛
30	O	O	O	⬛	O	⬛	🟩	⬛	🟩	U
40	O	O	O	⬛	O	⬛	🟩	U	🟩	U

Figure 2.11.: Summarized foot contact stability according to a leg angle, leg hardness, the number of leg, and perching speed. Green color denotes results of the single leg, black color denotes results of the double legs. **O** means the unstable foot contact due to the leg's over-fold, **U** means the unstable foot contact due to the leg's under-fold, Colored rectangle means stable foot contact through a leg's normal-fold.

performances to find the best design for perching performance.

2.2.2.2. Interlocking performance

Figure 2.13 shows perching behaviors through interlocking between the claws and surfaces; where Figure 2.13A shows an example of a successful perching procedure. If the foot contact is unstable, the first established interlock may be lost (Figure 2.13B). However, the robot has another chance to make a second interlock during the second absorption due to the change in

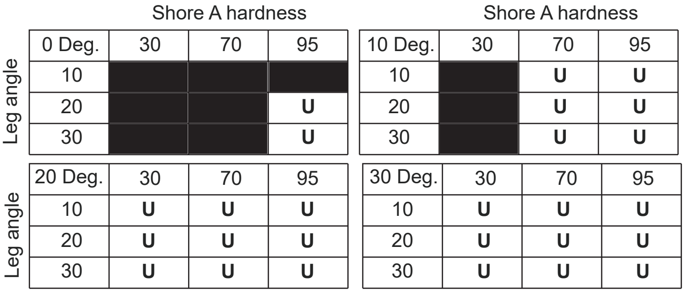

Shore A hardness

Leg angle

0 Deg.	30	70	95
10	■	■	■
20	■	■	**U**
30	■	■	**U**

Shore A hardness

10 Deg.	30	70	95
10	■	**U**	**U**
20	■	**U**	**U**
30	■	**U**	**U**

Leg angle

20 Deg.	30	70	95
10	**U**	**U**	**U**
20	**U**	**U**	**U**
30	**U**	**U**	**U**

30 Deg.	30	70	95
10	**U**	**U**	**U**
20	**U**	**U**	**U**
30	**U**	**U**	**U**

Figure 2.12.: Summarized foot contact stability according to a leg angle, leg hardness, and perching angle. The results are for the double legs. **U** means the unstable foot contact due to the leg's under-fold, Colored rectangle means stable foot contact through the leg's normal-fold.

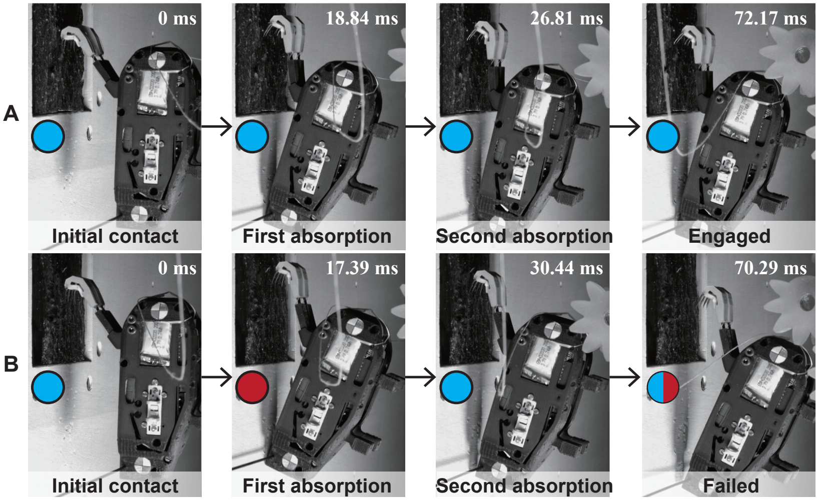

Figure 2.13.: Perching behaviors. A) Successful and B) failed perching procedures through interlocking. Blue and red circles denote interlocked and lost interlocking, respectively.

the pitch direction. As long as one of the interlocks is maintained, the robot will successfully perch on the surface. As a result, the perching performances are the results of the coupled shock-absorbing performances (Figure 2.5, 2.6, 2.7, 2.8, and 2.9), foot contact stability (Figure 2.10, 2.11, and 2.12), and the claw's interactions with the surfaces.

Including claws for interlocking with rough surfaces changes the shock-absorbing behaviors and foot contact stability as compared with the circular tip on flat surfaces. As the claws slide over the bumps of the rough surface, dynamic reaction forces are generated, which are not seen in flat surfaces. Due to the dynamic reaction forces, instantaneous leg folding generates more pitch torque because of the material's viscoelastic characteristics, which results in under-folding and accompanying loss of foot contact. For this reason, under-folding on rough surfaces occurs in softer materials as compared with flat surfaces (comparing the perching speed of 1.5 m/s in Figure 2.14A and Figure 2.11). Although establishing an interlock during the under-folding behavior is possible due to the second interlock, typically, the robot has low success rates for perching because the foot's bouncing during the under-folding behaviors requires more interlocking forces.

The claw's interlocking force can supplement deficiencies in the shock-absorbing performance for successful perching. Several parameters affect the interlocking performance. First, the leg angle changes the claw angle and interlocking forces. Presented angles in the bracket of Figure 2.14A are the final claw angles after a successful perch. If the claw angles are close to parallel ($\theta_c = 0$ degree) or perpendicular ($\theta_c = 90$ degrees) with the surface, interlocking becomes difficult. Although Figure 2.14A has a narrow range of the final claw angles, Figure 2.14B has clear differences in the final claw angles as compared to Figure 2.14A. As a result, the final claw angle of approximately 45 degrees has high success rates due to the robust interlock and reduced under-folding issues. Second, the interlocking force is a function of the surface characteristics, specifically hardness and robustness. The claws can penetrate a soft surface, so they have a more robust interlock and successful perching (Figures 2.15B) than a hard surface (Figure 2.15A). The robustness of the surface determines whether the interlock can be

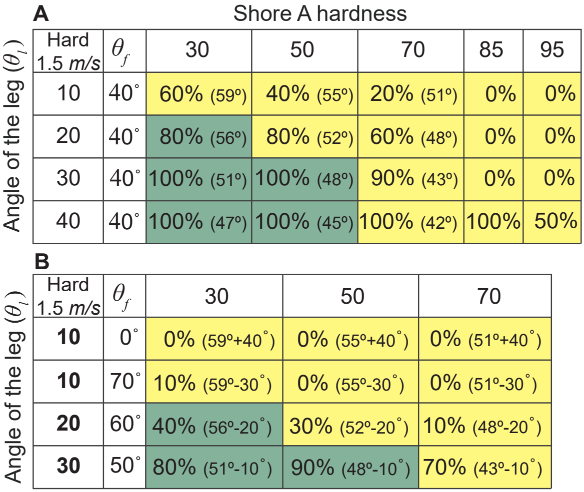

A

Shore A hardness

Angle of the leg (θ_l)

Hard 1.5 *m/s*	θ_f	30	50	70	85	95
10	40°	60% (59°)	40% (55°)	20% (51°)	0%	0%
20	40°	80% (56°)	80% (52°)	60% (48°)	0%	0%
30	40°	100% (51°)	100% (48°)	90% (43°)	0%	0%
40	40°	100% (47°)	100% (45°)	100% (42°)	100%	50%

B

Angle of the leg (θ_l)

Hard 1.5 *m/s*	θ_f	30	50	70
10	0°	0% (59°+40°)	0% (55°+40°)	0% (51°+40°)
10	70°	10% (59°-30°)	0% (55°-30°)	0% (51°-30°)
20	60°	40% (56°-20°)	30% (52°-20°)	10% (48°-20°)
30	50°	80% (51°-10°)	90% (48°-10°)	70% (43°-10°)

Figure 2.14.: Interlocking performances according to different conditions. A) Success rates of the perching and the claw angles after finishing the perching on the hard surface. B) Changes in success rates according to the claw angles (θ_c). For A), denoted angles in bracket are the claw angle after finishing the successful perching. For B), angles in the bracket denote the final claw angle after perching, and are changed as the difference of foot angles with A), the robot has double legs, the perching angle is parallel with the vertical surface. Green and yellow sections denote stable foot contact and unstable foot contact through under-folding of the shock-absorbing mechanism, respectively. Success rates are from 10 trials.

maintained or not. Real tree bark can be torn by the interlocking force, and the claws lose their hold as seen in Figure 2.15D. For this reason, success rates on the real tree bark (Figure 2.15E) have the same trend as on the hard surface (Figure 2.15A) due to the similar hardness, but have lower success rates due to the low surface robustness.

The interlock provides a robust perching behavior which is able to withstand changes in initial conditions. Initial perching speed determines the initial energy that must be absorbed by the shock-absorbing mechanism (Figure 2.9). Therefore, each combination of leg properties has different success rates, and the robust combination has high success rates at various

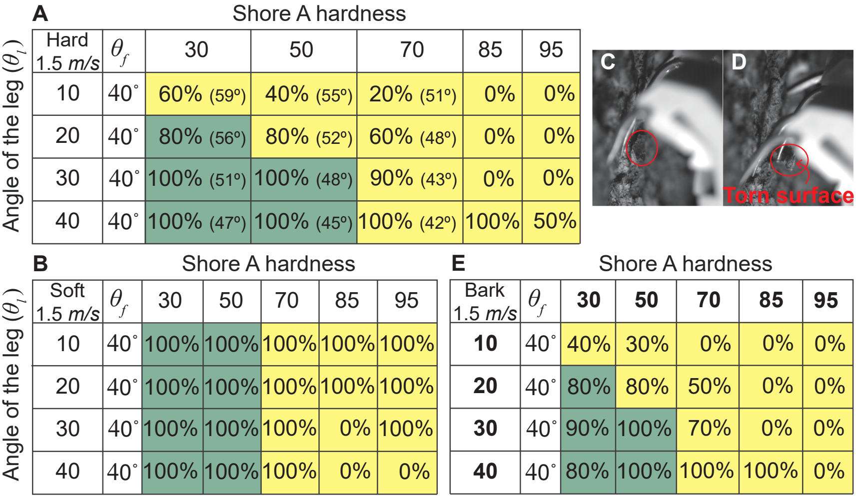

A

Angle of the leg (θ_l) / Shore A hardness

Hard 1.5 *m/s*	θ_f	30	50	70	85	95
10	40°	🟨 60% (59°)	🟨 40% (55°)	🟨 20% (51°)	🟨 0%	🟨 0%
20	40°	🟩 80% (56°)	🟨 80% (52°)	🟨 60% (48°)	🟨 0%	🟨 0%
30	40°	🟩 100% (51°)	🟩 100% (48°)	🟨 90% (43°)	🟨 0%	🟨 0%
40	40°	🟩 100% (47°)	🟩 100% (45°)	🟨 100% (42°)	🟨 100%	🟨 50%

B

Angle of the leg (θ_l) / Shore A hardness

Soft 1.5 *m/s*	θ_f	30	50	70	85	95
10	40°	🟩 100%	🟩 100%	🟨 100%	🟨 100%	🟨 100%
20	40°	🟩 100%	🟩 100%	🟨 100%	🟨 100%	🟨 100%
30	40°	🟩 100%	🟩 100%	🟨 100%	🟨 0%	🟨 100%
40	40°	🟩 100%	🟩 100%	🟨 100%	🟨 0%	🟨 0%

E

Shore A hardness

Bark 1.5 *m/s*	θ_f	**30**	**50**	**70**	**85**	**95**
10	40°	🟨 40%	🟨 30%	🟨 0%	🟨 0%	🟨 0%
20	40°	🟩 80%	🟨 80%	🟨 50%	🟨 0%	🟨 0%
30	40°	🟩 90%	🟩 100%	🟨 70%	🟨 0%	🟨 0%
40	40°	🟩 80%	🟩 100%	🟨 100%	🟨 100%	🟨 0%

Figure 2.15.: Interlocking performances according to different surface conditions. A) Success rates of the perching and the claw angles after finishing the perching on the hard surface. B) Success rates of the perching on the soft surface. C) Moment when the claw makes the interlocking at the bark surface. D) Failed interlocking due to a torn surface of the bark. E) Success rates of the perching on the real tree bark. For A), denoted angles in bracket are the claw angle after finishing the successful perching. For A), B), E), the robot has double legs, the perching angle is parallel with the vertical surface. Green and yellow sections denote stable foot contact and unstable foot contact through under-folding of the shock-absorbing mechanism, respectively. Success rates are from 10 trials.

perching speeds (Figure 2.16A, B, C). The leg angle of 40 degrees and shore A hardness of 50 have 100 % success rate under perching speed from 1 to 2 m/s. The initial perching angle, which is the initial pitch angle, also has different shock-absorbing behaviors and foot contact stability; where angled perching has an increase chance of under-folding issues. The claw's interlocking forces are able to hold the grasp during under-folding behaviors allowing the mechanism to have a range of successful perching angles (Figure 2.17). A leg angle of 40 degrees and shore A hardness of 50 shows 100 % success rate under perching angles from 90 to 95 degrees with perching speeds from 1 to 2 m/s.

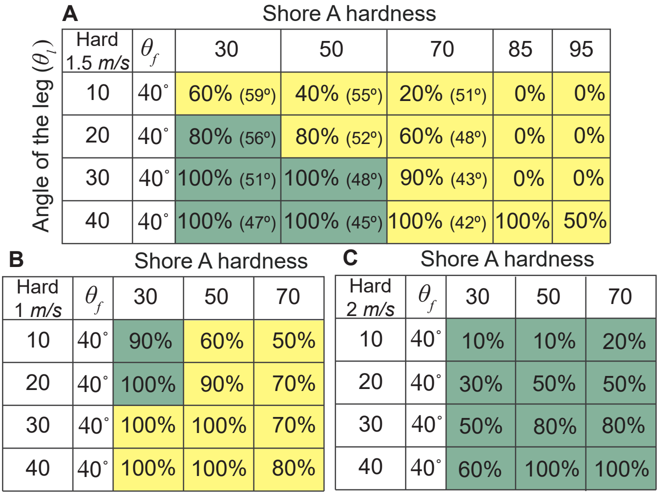

A

Angle of the leg (θ_l)

Hard 1.5 *m/s*	θ_f	Shore A hardness 30	50	70	85	95
10	40°	60% (59°)	40% (55°)	20% (51°)	0%	0%
20	40°	80% (56°)	80% (52°)	60% (48°)	0%	0%
30	40°	100% (51°)	100% (48°)	90% (43°)	0%	0%
40	40°	100% (47°)	100% (45°)	100% (42°)	100%	50%

B

Hard 1 *m/s*	θ_f	Shore A hardness 30	50	70
10	40°	90%	60%	50%
20	40°	100%	90%	70%
30	40°	100%	100%	70%
40	40°	100%	100%	80%

C

Hard 2 *m/s*	θ_f	Shore A hardness 30	50	70
10	40°	10%	10%	20%
20	40°	30%	50%	50%
30	40°	50%	80%	80%
40	40°	60%	100%	100%

Figure 2.16.: Interlocking performances according to different perching speeds. A) Success rates of the perching and the claw angles after finishing the perching on the hard surface. B), C) Success rates of the perching according to different perching speeds: 1 m/s for B) and 2 m/s for C). For A), denoted angles in bracket are the claw angle after finishing the successful perching. For A), B), and C), the robot has double legs, the perching angle is parallel with the vertical surface. Green and yellow sections denote stable foot contact and unstable foot contact through under-folding of the shock-absorbing mechanism, respectively. Success rates are from 10 trials.

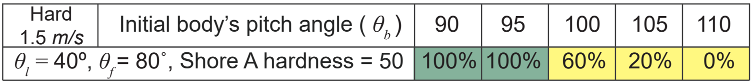

Hard 1.5 *m/s*	Initial body's pitch angle (θ_b)	90	95	100	105	110
θ_l = 40°, θ_f = 80°, Shore A hardness = 50		100%	100%	60%	20%	0%

Figure 2.17.: Success rates of the perching according to the perching angles. The robot has double legs. Green and yellow sections denote stable foot contact and unstable foot contact through under-folding of the shock-absorbing mechanism, respectively. Success rates are from 10 trials.

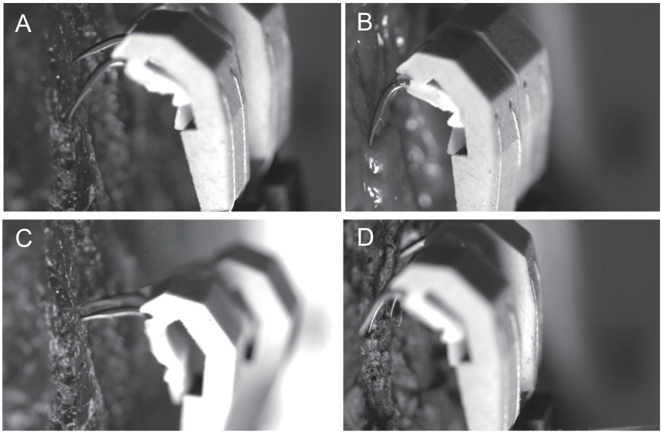

Figure 2.18.: Closed-up views for the interlocking and penetration at varied engagement conditions. A) succeed interlocking on a solid rough surface with the fastening mechanism (Shore D 80 similar to the safety hat), penetrating the surface with the claw is almost impossible to make the interlocking. B) Succeed interlocking on a soft rough surface (shore A 30 similar to an eraser), penetrating the surface with the claw is possible to make the interlocking. C) Failed interlocking on a solid rough surface without the fastening mechanism, D) Succeed interlocking on real tree bark.

Employing the selected parameters, close up views of the interlocking between the claws and various surfaces, and the behaviors of the fastening mechanism are provided in Figure 2.18. Supplementary video S1 showcases demonstrations on possible surfaces around us, such as a rough surface, tree bark, timber, card board, towel. Success rates from 10 trials are 80% (rough surface), 90% (tree bark), 90% (timber), 100% (cardboard), and 100% (towel). The rough surface is bonded small rock particles, which have a grain size of 1.27-2.08 mm.

2.2.3. Integration of jumping and perching

Figures 1.7 and 2.19 show robot configurations and the integrated jumping and perching locomotion modes, respectively. Opening the jumping mechanism is necessary for successful perching as the legs would otherwise impede to interaction of the perching leg and surface (Figure 2.19a-d). The jumping mechanism has a rotational connection to a body, and torsion springs provide a passive opening motion (Figure 1.9f). The mechanism opening produces proper pitch torques with a jumping direction of 80 degrees, creating a parallel perching angle to the vertical surface at the apex of the jumping trajectory (Figure 2.21). Therefore, for experimental testing, I selected the parameters of the shock-absorbing mechanism for this scenario, which results in a 1.78 m/s perching speed at the apex (Shore A hardness: 50, leg angle: 40 Deg., double legs, and leg length : 40 mm). To maintain the initial position of the robot prior to jumping, a experimental rig was developed (Figure 1.7d). For stable jumping without the holder, work has been done to study interactions between the foot and ground [125]; however, we need further studies to employ the results of the work. Supplementary Video S2 shows how the clutch mechanism works.

Figure 2.19B provides success rates of demonstrations on different surfaces. Soft surfaces (duplicated bark pattern with soft material, card board, and towel) have higher success rates than hard surfaces (duplicated bark pattern with hard material and rough surface). This is expected as penetration can create interlocks on soft surfaces while interlocks must be found by the claws on hard surfaces. The procedure for jumping after a perch, including how the robot stores the jumping energy and releases the interlock with the surface, are described in Figure 2.20 and supplementary video S4. In addition, the Figure 2.20 shows an example of a task after perching on the vertical surface, such as taking pictures for exploring purposes at an elevated position.

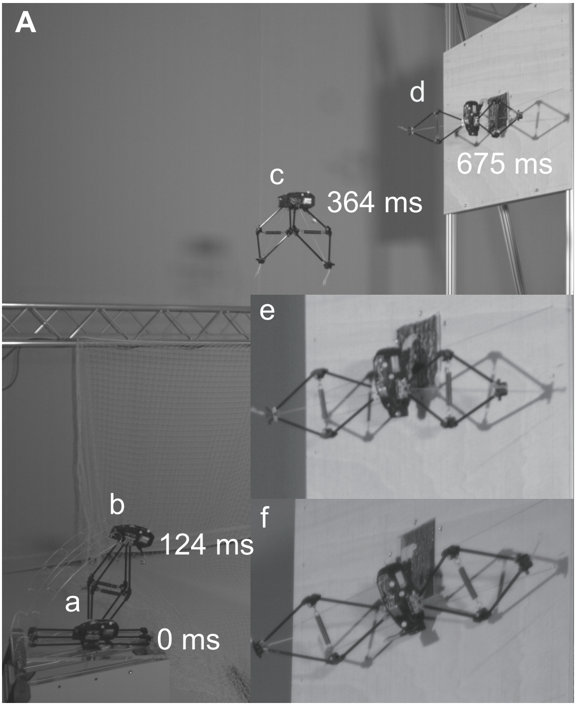

B

Test surface	Success rate
Duplicated bark pattern with hard material	80 %
Duplicated bark pattern with soft material	100 %
Rough surface (bonded small rock particles)	70 %
Card board	100 %
Towel	100 %

Figure 2.19.: Demonstration of the integrated jumping and perching locomotion modes. A) Integrated motion from jumping to perching on a vertical surface: a. robot stores jumping energy in leg mechanism, b. released jumping energy takes off a robot from the ground, c. leg mechanisms are opened for a perching motion, d. leg mechanisms are fully opened before contact with surfaces, e. parallel perching angle to vertical surface (jumping direction : 80 degrees), f. not parallel perching angle to vertical surface (jumping direction : 90 degrees). B) Success rates of jumping-perching on various surfaces, the success rates come from 10 trials. Supplementary Video S3 showcases jumping-perching performances of the robot at various surfaces.

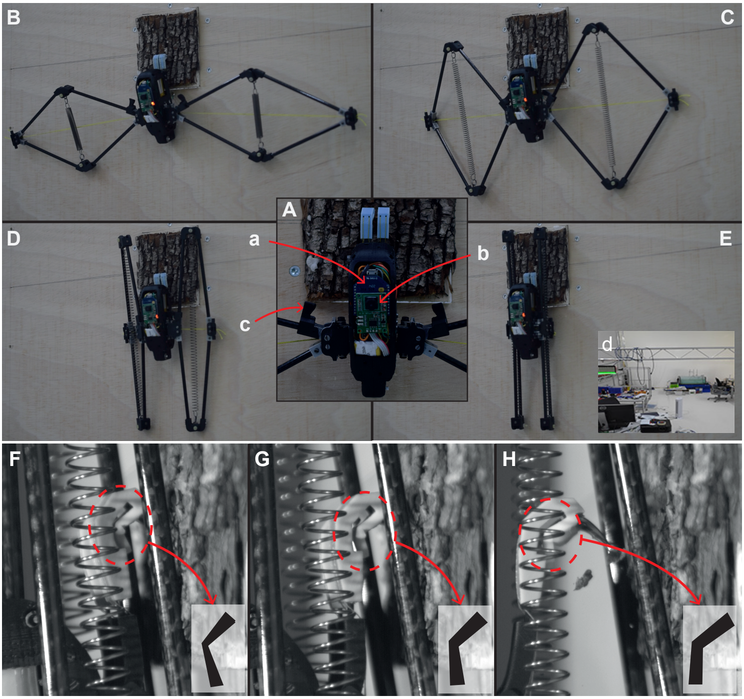

Figure 2.20.: Jumping from the vertical surface. A. Configuration of electronics and passive folding mechanism, a. wireless communication module (Xbee), b. camera module (Miniature TTL Serial JPEG Camera, Adafruit), c. tongue to fold the jumping mechanism, the tongue generates torque to fold the jumping mechanism by touching the body surface while the jumping mechanism is compressing, d. a taken picture transferred through the wireless communication module. B. Staying on the vertical surface after perching, C. compressing jumping mechanism to store the jumping energy, D. the tongue touches a body surface and folds the jumping mechanism passively, E. fully folded and compressed jumping mechanism. F. fastening mechanism fastens a claw's interlocking with the surface before the robot starts to jump, G. the fastened interlocking is loosed during jumping, H. engagement between claws and surface is disappeared by the loosed interlocking. Inside Figures in F-H indicate shape changes of a flexible part in the fastening mechanism. The supplementary video S4 shows a procedure of the robot's jumping energy storage (B-D).

2.3. Discussion

2.3.1. Design methodology

The best design parameters create robust perching performance under various conditions, such as perching speed, angle, and surface hardness. The perching motion of this work occurs after the jumping motion. I selected the jumping direction as 80 degrees to have the proper perching angle at the apex of the jumping trajectory, and the perching speed and angle were 1.78 m/s and parallel with the surface, respectively. In the section for the interlocking performance (section 2.2.2.2), I varied the design parameters of the perching mechanism to observe the success rates. A leg angle of 40 degrees, shore A hardness of 50, double leg, and claw angle of 40 degrees had robust perching performances on various surface conditions. To have robust performance under various perching speeds, given a leg designed for a specific perching velocity, low velocities will result in less absorption however, the lower energy overall requires lower interlocking forces. Perching velocities above the designed velocity will require higher interlocking forces as the additional energy will not be absorbed by the leg mechanism and therefore will remain in the system. Therefore, ideally the leg should be designed for the maximum perching speed observed as lower speeds will create more successful perching as compare to higher speeds. In this case, the selected parameters show stable perching performances between the perching speeds from 1 to 2 m/s, which is a sufficient range for this work's perching scenario. In the case of the perching angles, θ_b, perching angles under zero degrees reduce the first absorption, causing less shock absorption (Figure 2.19A.f). At perching angles greater than zero degrees, shock absorption was improved but caused under-folding and unstable foot contact stability (Figure 2.8 and Figure 2.12). Therefore, we need to avoid negative perching angles. The selected parameters show high success rates at perching angles between 0 and 5 degrees (Supplementary video S3 showcases perching performance after jumping with the designed parameters on various surfaces).

2.3.2. Performance improvement

Interactions between integrated motions can improve the overall performance of the robot. Examples include:

The first improvement is focused on the jumping trajectory characteristics. Jumping with angle and integrated perching and jumping allow for different strategies in using the initial jumping energy to create horizontal distance. While an angled jump divides initial jumping energy into horizontal and vertical kinetic energies (θ_j = 30-90 Deg., Figure 2.21), the robot can generate a very different trajectory by first jumping vertically and perching then jumping horizontally ($\theta_j = 0$ Deg., Figure 2.21). The maximum jumping distance for this robot is observed at a jumping angle, θ_j, of 60 degrees; as seen in Figure 2.21. However, the shallower the jumping angle the higher the possibility of hitting an obstacle and therefore certain obstacles may be impassable by an angled jump; e.g., being in a hole. Assuming a robot can only jump at a single angle, a vertical jump with perching, has the highest apex point to overcome obstacles while perch jumping can still yield significant horizontal distances. Procedure of how the robot jumps on the vertical surface after perching is described in Figure 2.20. Additionally, assuming the robot is able to alter its jumping angle while perched, a perched angled jump can create the maximum horizontal distance travelled to overcome a wide obstacle; this will be explored in future work.

The second improvement is focused on improving glide performance in integrated jumping and gliding robots, such as the MultiMo-Bat [13, 14], which could also integrate a perching mechanism. As gliding performance is dependent on the initial conditions, a perched horizontal jump can provide the initial gliding velocity and height potential energy which would greatly enhance the overall gliding distance as compared a vertical jump which provides zero initial horizontal velocity.

The final improvement is focused on observation and non-locomotion tasks. vertical jumping and perching at the apex of jumping trajectory maintains the high position. The high position provides wide range of view to the robot for exploring tasks. I did a demonstration to take a picture after perching as the exploring purpose (Figure 2.20d). In addition, robot can do other tasks such as battery charging through solar cells.

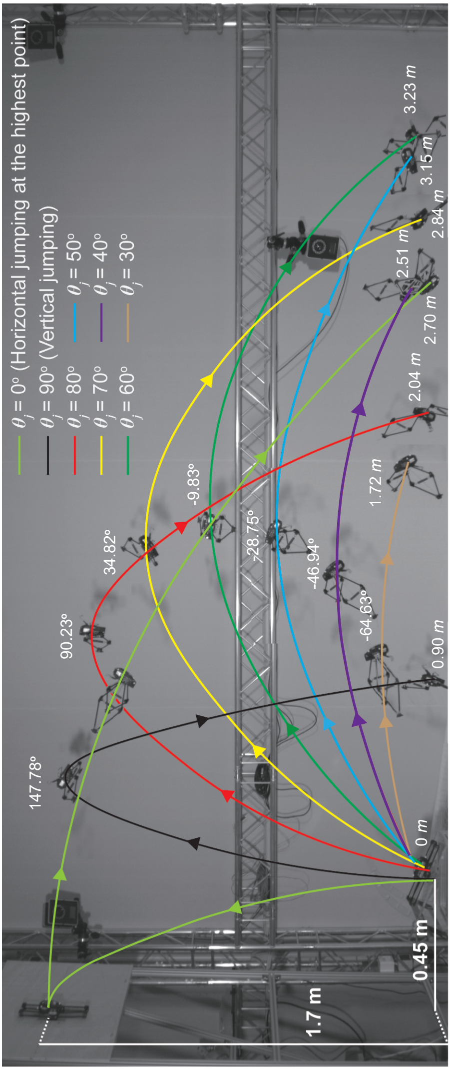

Figure 2.21.: Jumping behaviors according to different jumping angles. Captured robots are when the robot reaches the apex points and landing positions. Provided angles denote body's angles at the apex point of jumping trajectories. Provided distances are jumping distances when the robot reaches the same horizontal level with start height. Results are averaged, maximum and minimum values by 10 trials. Detailed measured behaviors are described in table B.1 in Appendix B.

2.4. Summary

This chapter integrates perching locomotion mode into a jumping robot. I developed a perching mechanism inspired by a bird's leg, which has shock-absorbing and foot-engagement parts. A 3D-printable viscoelastic material absorbs energy through its deformation (folding). The perching mechanism is characterized according to the design parameters, such as leg angle, hardness, mechanism length, number of legs (thickness), and initial perching conditions, such as perching speed and angle. Claws establish the engagement through mechanical interlocking and penetration. The engagement performance is characterized according to the leg angle and hardness, which determine shock-absorbing performances, surface hardness, and perching conditions. Finally, I proved the performance of the perching mechanism by demonstrating a jumping-perching motion. With the developed perching mechanism, I proposed how the motion integration improves the robot's performances, such as jumping and gliding distances and tasks after perching.

I found that the developed perching mechanism absorbs a perching shock properly and has robustness on perching speeds of 1-2 m/s, and perching angles of 0 to 5 degrees to various surface conditions. Through the case study, I have learned how we can improve the perching performance, such as pitch control to overcome limited perching angles. In future work, I will design an active tail, specifically an aerodynamic tail, and improve the flexibility of perching performances for various jumping behaviors. In addition, I will maximize the synergy of motion integration through an additional integration of gliding.

CHAPTER 3

ACTIVE TAIL CONFIGURATIONS FOR ENHANCED BODY REORIENTATION PERFORMANCE

H Kim, M A Woodward, M Sitti, "Active Tail Configurations for Enhanced Body Reorientation Performance", Advanced Intelligent Systems, 2022, http://doi.org/10.1002/aisy.202200219.[77]

During dynamic locomotion, animals employ tails to help control the orientation of their bodies. This type of control is pervasive throughout locomotion strategies. Roboticists endeavor to close the gap between robots and their biological counterparts by developing various active tails. This chapter explores these active tails and establishes a design strategy to enhance reorientation performances. I suggest a dynamic model to describe the transmitted torques at the body from the single-axis active tail. The design parameters, which define the transmitted torques, are analyzed through the dynamic model to understand their contributions. The effects of aerodynamics on the active tail's performance are also explored. The active tails are categorized according to inertial tail designs (unbalanced distal mass or mass-balanced about a rotating point), aerodynamic configurations (inertial, aerodynamic, aerodynamic with external airflow), and operating strategies (partial oscillation, symmetric oscillation, asymmetric-oscillation or full rotations). I explore the reorientation performance of 24 possible active tail combinations and provide design strategies to select the proper combinations according to the target system's conditions. Reults can help in guiding the advanced active tail designs for future agile mobile robots. As co-authors, Prof. Matthew A. Woodward and Prof. Metin Sitti contributed to the discussions and edited the manuscript. The results of this chapter are reproduced from reference [77].

3.1. Dynamic model and testing

I developed both a dynamic model to simulate and an experimental setup to measure the transmitted torques at the body from an active tail. Figure 3.1A,B show the free-body diagram and the associated experimental setup, respectively. The model consists of two bodies, a fixed body and active tail, connected by a single DC motor with an encoder. The experimental setup uses a torque sensor to directly measure the transmitted torque from the single DOF active tail to the body; this can then be used with the rotational inertia of a given body, to determine the change in angular momentum. The

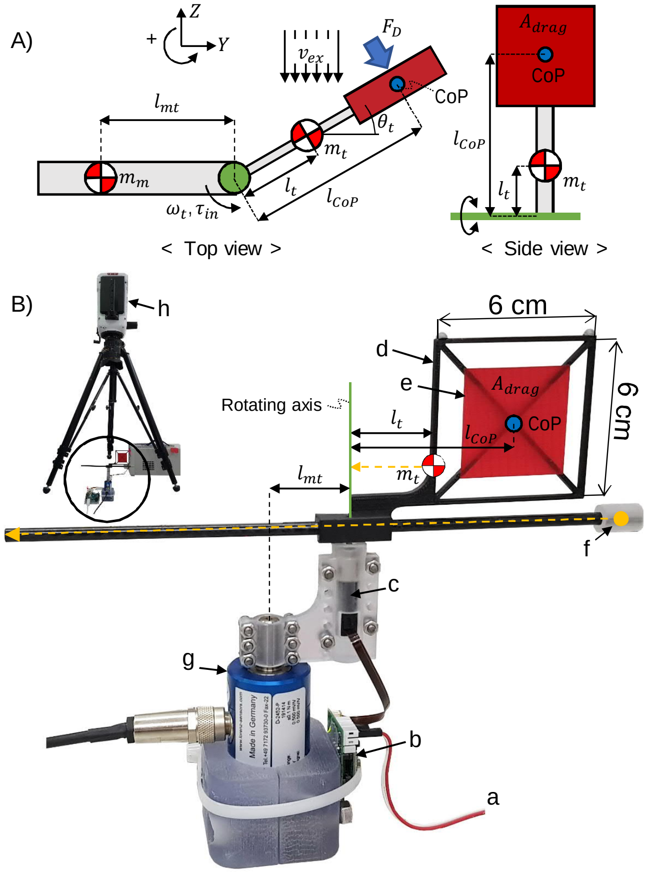

Figure 3.1.: Modelling and experimental measurement of the transmitted torque at the body from the active tail. A) Schematic side and top views of the two-body dynamic model. The green circle and line denote the tail's connection point, rotation axis, and actuator position. B) Experimental setup for measuring the transmitted torque at the body from the active tail. The blue circles denote the center of pressure, CoP. a. Power line, b. Controller, c. DC motor (Maxon motor, 347727, gear head, 474124) with rotary encoder (Maxon motor, 334910, 100 pulses per revolution), d. Tail frame, e. Coated ripstop nylon, f. Movable mass to change tai's mass center, g. Torque sensor (Lorenz-messtechnik GMBH, D-2452-P, 2500Hz), h. High-speed camera (Phantom v641, 1400 fps).

tail has both an aerodynamic surface (square-shaped red area, A_{drag}) with center of pressure, CoP, to create and vary the aerodynamic forces, and a movable mass to create and vary the inertia. I assumed that the CoP is always placed at the center of area of the aerodynamic surface, and the air drag force is always perpendicular to the aerodynamic surface. The position of the tail's CoM, $\vec{P}_{tail}$, is defined as follow:

$$\vec{P}_{tail} = l_{mt} e^{0} + l_{t} e^{\theta_t}, \tag{3.1}$$

where l_{mt} is the distance between the body's CoM and the connecting point of the tail, and l_t is the distance of the tail's CoM from the connecting point of the body. The tail angle, θ_t, is zero when the tail is parallel with the body. The Lagrange equation $L = KE_{tail} - PE_{tail}$ is then defined by the kinetic energy, KE_{tail} and potential energy, PE_{tail}, of the tail. The active tail does not have gravitational effects because the tail rotates on the horizontal plane. So, the Lagrange equation has zero potential energy, and the kinematic energy is calculated as follows:

$$KE_{tail} = 0.5 m_t |\dot{\vec{P}}_{tail}|^2 + 0.5 I_t (\omega_t)^2, \tag{3.2}$$

where the mass of the tail is, m_t, I_t is the moment of inertia of the tail, which is calculated with material properties, l_t is a tail length, and ω_t is the angular velocity of the tail. The air drag force is an external force to the system and can be generated by both the tail's swing and external air flow, where the external air flow can be due to both the robot's locomotion characteristics and atmospheric flow. We can define the air drag force, F_D, and air flow speed, v_{flow}, at the tail as follow:

$$\begin{aligned} F_D &= 0.5 C_d \rho A_{drag} (v_{flow})^2, \\ v_{flow} &= l_{CoP} \omega_t + v_{ex} cos(\theta_t), \end{aligned} \tag{3.3}$$

where C_d is the drag coefficient of the square-shaped drag surface, ρ is the density of the air, A_{drag} is the plane area for the aerodynamic forces, l_{CoP} is the distance between CoP and connecting point of the tail, and v_{ex} is the external airflow speed. The drag coefficient of this work is constant due to the assumption that the angle of attack is always 90 degrees. Although the dynamic model cannot capture the full aerodynamics of the tail locomotion, the drag forces can not only maintain their direction according to the angle of attack through an aerodynamic shape design but also be maximized through the active tail's adaptation to the airflow for a favorable angle of attack. For this reason, the fixed drag coefficient can describe the trend changes in the transmitted torques from the active tail. The dynamic equations are derived from the Lagrange equation and defined external forces, F_{ex}:

$$\begin{aligned}
&\frac{d}{dt}\frac{\partial L}{\partial \dot{\theta}_t} - \frac{\partial L}{\partial \theta_t} = F_{ex},\\
&F_{ex} = \begin{bmatrix} -F_D(l_{CoP} + l_{mt}cos(\theta_t)) \\ -F_D l_{CoP} + \tau_{in} + K_g \omega_t \end{bmatrix}\\
&\tau_{in} = \eta n K_t / R_m V_{in},
\end{aligned} \tag{3.4}$$

where the external forces on the tail includes the input torque from the tail actuator, τ_{in}, aerodynamic forces, and resistance forces from the DC motor. K_g is empirically measured constant to define mechanical resistance forces of the DC motor, η is efficiency of the gear head, n is gear raio, K_t is torque constant, R_m is motor resistance, V_{in} is input voltage. Values for each parameter are summarized in the Table 3.1, 3.2. We can rearrange the dynamic equation for the transmitted torque at the body from the active tail as follows,

$$\begin{aligned}
&\tau_I = -I_t \alpha_t,\\
&\tau_T = -(l_t + l_{mt}cos(\theta_t)) m_t l_t \alpha_t,\\
&\tau_C = m_t l_{mt} l_t sin(\theta_t)\omega_t^2,\\
&\tau_A = -\frac{v_{flow}}{\|v_{flow}\|}(l_{CoP} + l_{mt}cos(\theta_t))F_D,\\
&\tau_{tr} = \tau_I + \tau_T + \tau_C + \tau_A.
\end{aligned} \tag{3.5}$$

where α_t is the angular acceleration of the tail. τ_I is transmitted torque from

Table 3.1.: Parameters and their values used in the dynamic model

m_t	$8.45\ g$	ρ	$1.23\ kg/m^3$	C_d	1.12
l_{CoP}	$60\ mm$	K_g	$0.48\ mNm/(rad/s^2)$	η	0.67
R_m	$92.2\ \Omega$	K_t	$7.11\ mNm/A$	n	36

the tail's moment of inertia. The rotation of the tail generates tangential and centrifugal forces at the tail's CoM, while the aerodynamic forces are generated at the tail's CoP. These forces become tangential (τ_T), centrifugal (τ_C), and aerodynamic (τ_A) torques at the CoM of the body based on their respective distances l_t and l_{mt}. τ_{tr} is an instantaneously transmitted torque from the active tail to the body's CoM at each point in time. I use averaged torque to compare the performances of the active tail's different configurations, and the averaged torque is defined by averaging the transmitted torque (τ_{tr}) up to that moment in time. We can also estimate an angular momentum of the body from the transmitted torque (τ_{tr}) because the angular velocity is proportional to the integrated transmitted torque by tail operation time.

The simplified model does not capture the full details of a real tail because the model is under a condition of energy conservation unlike the real tail operation, especially with aerodynamics effects. Therefore, I observed trend changes in the transmitted torque according to the design parameters, and it can inform design decisions. Observing the trend changes of the transmitted torque can be applied to any body because I measured trend changes without any effects from the body's characteristics. The dynamics are the same in any rotational direction, if there are no external effects, such as gravity and aerodynamics. Although this work observes tail's performance in plane, external effects must be considered for a tail operation in space because each rotational direction has own external effects. In this sense, this section studies the roles of the design parameters in determining the trend changes of the transmitted torque and thus body orientation control, without external effects. I also study performance changes of the tail according to the external effects, especially aerodynamics allowing the dynamics model to deviate

Table 3.2.: Parameters for the tail configuration and operating strategy

l_t (mm)	l_{mt} (mm)	Operating strategy	-	v_{ex} (m/s)	A_{drag} (cm ^ 2)
0 10	0 10	(S)ymmetric or (A)symmetric oscillation	p 1 2 3	0	00
30 50	30 50	(P)artial Oscillation or (F)ull rotation	θ_r (Deg.) 10 30 50 180 1500	1 2	04 16 36

Example: 1030P30&236 → l_t = 10 mm, l_{mt} = 30 mm, Operating strategy= Partial oscillation, θ_r = 30°, v_{ex} = 2 m/s, A_{drag} = 36 cm^2. θ_r denotes the rotation angle of the tail. p denotes absolute value of ratio between the input voltages in the positive and negative directions; i.e., $V_{in,positive} = pV_{in,negative}$.

from the constraint of energy conservation. This understanding allows for the tuning of the design parameters to optimize an active tail for any target systems.

3.1.1. Transmitted torque parameters

Transmitted torque, τ_{tr}, is determined by the coupled parameters shown in Figure 3.1. The interdependence of these parameters requires that they are considered together; however, the contributions of each differ. Figure 3.2 demonstrates the changes in the averaged torque from the active tail at a number of different configurations, where only one parameter is modified to show its significance.

The angular position of the tail is one of the dominant parameters as the tangential, centrifugal, and aerodynamic forces are generated in different directions according to the angular position of the tail, θ_t, as shown in

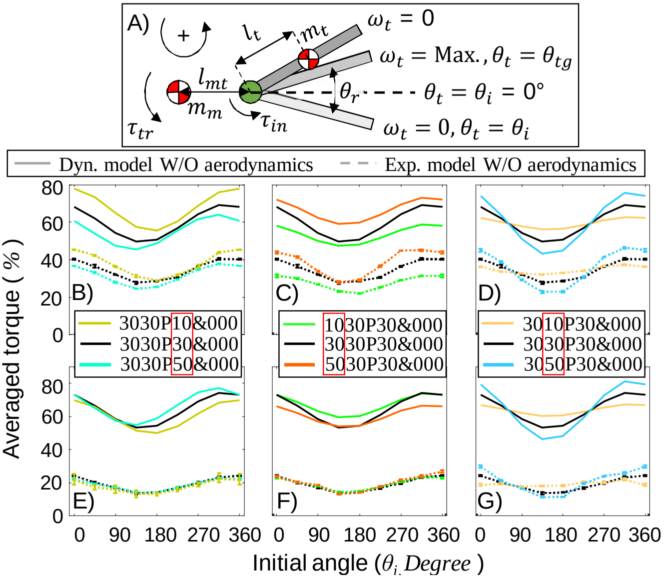

Figure 3.2.: Averaged torque changes of the inertial tail according to variations of the design parameters. A) Schematic view of the tail operation: the tail is accelerated in the positive direction from the initial angle, θ_i, to the target angle, $\theta_{tg} = \theta_i + \theta_r$, with a input torque of constant voltage, V_{in}=12 V. When the tail rotation reaches the target angle (zero angular velocity, ω_t), the input voltage is changed in the opposite direction with the same voltage (V_{in}=-12 V) for the deceleration. This result is free from gravity. B-G) Averaged transmitted torque from the active tail's dynamic and experimental models during the acceleration (B-D) and deceleration (E-G) according to variations of rotating angle (B, E), tail length (C, F), and distance between body's CoM and tail's connecting point (D, G). The averaged torques are normalized by the maximum transmitted torques, which occurs at 3050P30000 and θ_i = 0 degrees in all candidates: -25.6593 mNm for acceleration (B, C, D) and 37.7779 mNm for deceleration (E, F, G). All results from the experimental measurements are from 5 trials, and indicated with error bars. The legend follows a rule given in Table 3.2.

equation (3.5). Therefore, to determine the averaged transmitted torques of a partial oscillation, both simulations and experiments were conducted at different initial tail positions. The procedure is as follows: the tail is positioned at the initial angle; it is accelerated through the specified angle change with a constant input voltage, then decelerated to zero velocity like Figure 3.2A. The results are shown in Figure 3.2B-D (acceleration state) and Figure 3.2E-G (deceleration state). During the acceleration state, the trend shows a maximum transmitted torque, opposite the acceleration direction, at an initial angle of zero degrees. Therefore, given only a short time to reorient before contact, initiating the acceleration state at zero degrees will give the maximum body reorientation; the deceleration state would then occur after contact was made and the energy dissipated into the robot and contact. Examples of such a scenario would be a fall, hopping motion, or short jump.

The rotation angle, θ_r, determines the angular acceleration and velocity during the tail's rotation. The tangential torque (τ_T) is proportional to the angular acceleration, whereas the centrifugal torque (τ_C) is proportional to the square of the angular velocity (equation (3.5)). Therefore, the tangential torque dominates the initial rotation behavior. At some point during the rotation, the acceleration can saturate to zero due to the back EMF force of the DC motor and friction. It is at this point that the angular velocity will saturate to its maximum value and therefore the centrifugal torque will be dominant. The effects of changing the rotation angle can be observed in the comparison between configurations 3030P10&000, 3030P30&000, and 3030P50&000 in Figure 3.2, where '&000' means there are no aerodynamic effects in these configurations. Large rotation angles can result in longer acceleration states; however, the transmitted torque is inversely proportional to the rotation angle. As a result, initial torques from the angular acceleration (τ_T and τ_I) are reducing as the tail is accelerated. Such reduction can potentially cause a change of the torque direction in the undesired direction. In this sense, we can find proper rotation angle to avoid loss of the transmitted torque or angular momentum of the body for a target system.

The distance between the tail CoM and joint, l_t, and the distance between body CoM and joint, l_{mt}, determine the moments of inertia of the system, and changes in the moments of inertia can affect the torque transmission. Whereas l_t inherently changes the tail operation, l_{mt} does not; this is because increasing l_t increases the tail inertia and would therefore decrease the tail acceleration. The effects of changing l_t can be seen in the tail configurations 1030P30&000, 3030P30&000, and 5030P30&000. The transmitted torques are increased in the opposite direction of the tail acceleration with larger l_t during the acceleration state (Figure 3.2B-D). Averaged torque is reduced in the opposite direction of the tail acceleration during deceleration state (Figure 3.2E-G) with the longer l_t. As a result, while the l_t can increase the transmitted torque and angular momentum of the body, it reduces agility of the tail and requires more power to accelerate. In this relationship, there will be optimal points for the target system between the actuator power and required control torque from the tail. The transmitted forces at the tail joint including tangential, centrifugal, and air drag forces, represent torques on the body through the distance l_{mt}. The forces are transmitted in different directions to the connecting point of the tail about the tail's angular position. So, the changes of transmitted torque about the distance l_{mt} are also different according to the angular position of the tail. Tail configurations of 1010P30&000, 1030P30&000, and 1050P30&000 show different transmitted torques as a function of l_{mt}. As a result, we have to consider the angular position together to find the optimal l_{mt}.

3.1.2. Coupled inertial and aerodynamic tail

Incorporating an aerodynamic component to the tail allows it to deviate from the constrains of conservation of angular momentum, and create angular momentum changes which persist even once the tail has come to rest or, with external airflow, without moving the tail at all. While the net torque, summing torques during the entire acceleration and deceleration states, of the pure inertial tail is zero due to energy conservation, as shown in Figure 3.3, the net torque of the aerodynamic tail is none-zero with the incorporated aerodynamic forces, and this additional torque can enhance the

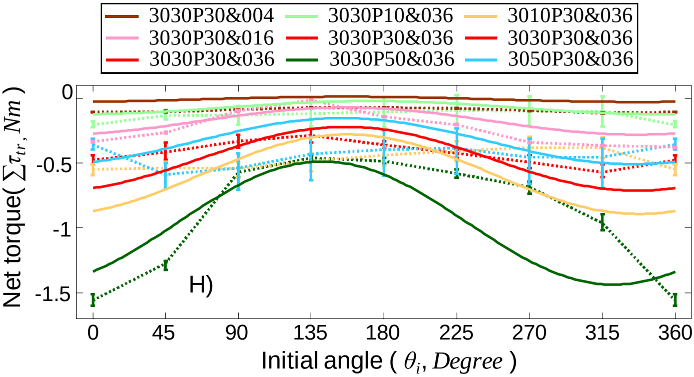

Figure 3.3.: Net transmitted torque, $\Sigma\tau_{tr}$, from the dynamic and experimental models after the acceleration and deceleration states, Results from the experimental model are from 5 trials, and indicated with error bars. The legend follows a rule given in Table 3.2.

tail's ability to control the orientation of the body. The aerodynamic torque is also a function of the angular position of the tail, as seen in equation (3.5), and we see the same trend as observed for the inertial tail. The maximum transmitted torque, in the direction opposite to the tail's acceleration, occurs at an initial angle of 0 degrees and the minimum transmitted torque occurs at 180 degrees; the specific values are again functions of θ_r, l_t, and l_{mt} and will therefore change with these values as well.

The aerodynamic force is defined by a number of parameters, in particular the drag surface, A_{drag}. Assuming the drag surface component is massless - it is very thin square-shaped film with a drag coefficient of 1.1219 - the larger the drag surface is the larger the aerodynamic forces are. As shown in Figure 3.4 (3030P30&004, 3030P30&016, and 3030P30&036), increasing the size of the drag surface has the effect of accentuating the difference between the maximum and minimum transmitted torques as a function of the initial angle. These changes have the same trend according to variation of the drag coefficient as defined in equation 3. The model has a harder time capturing the behavior of the aerodynamic tail indicating that the real aero-

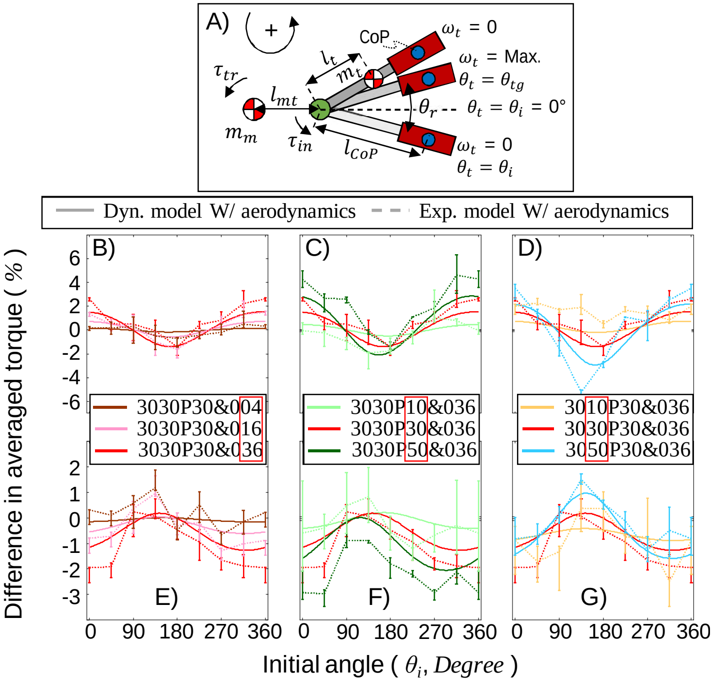

Figure 3.4.: Change in the averaged torque according to the aerodynamic forces. A) Schematic view of the tail operation: The blue circle denotes the center of pressure (CoP). The red area denotes a drag surface of the aerodynamic forces. The distance between the CoP and tail's rotating point, l_{CoP} = 60 mm. The tail is accelerated in the positive direction from the initial angle, θ_i, to the target angle, θ_{tg}, with a input torque of constant voltage, V_{in}=12 V. When the tail reaches the target angle (zero angular velocity, ω_t), the input voltage is changed to the opposite direction with the same voltage (V_{in}=-12 V) for the deceleration. This result is free from gravity. B-G) Aerodynamic torques from the active tail's dynamic and experimental models during the acceleration (B-D) and deceleration (E-G) according to variations of the drag area (B, E), rotating angle (C, F), and distance between body's CoM and tail's connecting point (D, G). The difference in averaged torque is the amount of change after incorporating the aerodynamic component to the inertial tail. Results from the experimental model are from 5 trials, and indicated with error bars. The legend follows a rule given in Table 3.2.

dynamics are not well captured by the simplified drag force. The rotation angle (θ_r) also has the same effect as discussed previously; larger rotation angles provide more time to develop the transmitted torque, as seen in Figure 3.4 configurations 3030P10&036, 3030P30&036, and 3030P50&036. As I discussed, the performance of the aerodynamic tail can be better than the inertial tail at angular position of the tail around zero degree. In the operating range around 0 degrees, we can find optimal drag surface and rotation angle for a target system. Lastly, from ($l_{CoP} + l_{mt}cos(\theta_t)$) in equation (3.5), it is observed that the ratio between l_{CoP} and l_{mt} determines the possible torque directions given a specific tail angle, θ_t. If $l_{CoP}/l_{mt} < 1$ the transmitted torque can be both positive or negative depending on the tail angle whereas, if $l_{CoP}/l_{mt} > 1$, the transmitted torque will always be in the same direction. The effects of changing l_{mt} has a significant effect on the transmitted torque as observed in Figure 3.4 configurations 3010P30&036, 3030P30&036, and 3050P30&036. As a result, longer l_{CoP} make the aerodynamic torque stronger, and the direction of torque is decoupled by the angular position of the tail when the l_{CoP} is longer than l_{mt}. The proposed model represents a basic unbalanced distal mass type of active tail; however, through varying the parameters of this model, other basic tail models can be developed and are discussed in the following section.

3.2. Active tail types

We can categorize active tails according to the location of the tail's mass, l_t, and the tail's connecting point in the body, l_{mt}. The first type is an unbalanced distal mass, which is presented in the previous section and is the common type seen in nature. Roboticists however have also developed the mass-balanced tail type, where the CoM of the tail is located at the rotation joint; therefore, l_t is zero. Mounting this tail at the CoM of the body, results in zero l_{mt}, as well. This means that the mass-balanced type does not generate the tangential and centrifugal forces, and the tail operation can be decoupled from the tail's angular position. This section will analyze and compare the characteristics of these two types of tails with the addition of aerodynamic forces and variable operation strategies including: partial oscillation, symmetric oscillation, asymmetric oscillation, and full rotations.

3.2.1. Unbalanced distal mass tail with partial oscillation

Figure 3.5 shows the performance of the unbalanced distal mass type undergoing partial oscillation. As mentioned in the previous section, with the inclusion of aerodynamic forces, the tail can generate and transmit a net torque after a full acceleration and deceleration cycle. This can be further affected by the robot's locomotion which can generate additional airflow. The tail can use this external airflow to generate more aerodynamic forces thus increasing the torque transmission. In Figure 3.5, the angular velocity (Figure 3.5B) is reduced with the aerodynamic forces, but the transmitted torque is increased during the acceleration state (Figure 3.5C) in the opposite direction of the tail's acceleration. During the deceleration state (Figure 3.5D), the torque from the acceleration state is not perfectly compensated by the deceleration because the aerodynamic force consumes the tail's rotational energy to generate torque in the opposite direction of the tail rotation. As a result, the averaged torque (Figure 3.5E-G) is increased after the acceleration and deceleration states with the aerodynamic forces. Even though it depends on the tail's angular position as seen in results of Section II, the aerodynamic force generates more torque in the opposite direction of the tail rotation at the specific angular positions. The result is an increase in the body's angular momentum at the completion of a partial oscillation. This type of tail is suitable to use under a condition of a limited operation, specifically, limited operating time. The active tail has to be designed to generate enough control torque for a limited time.

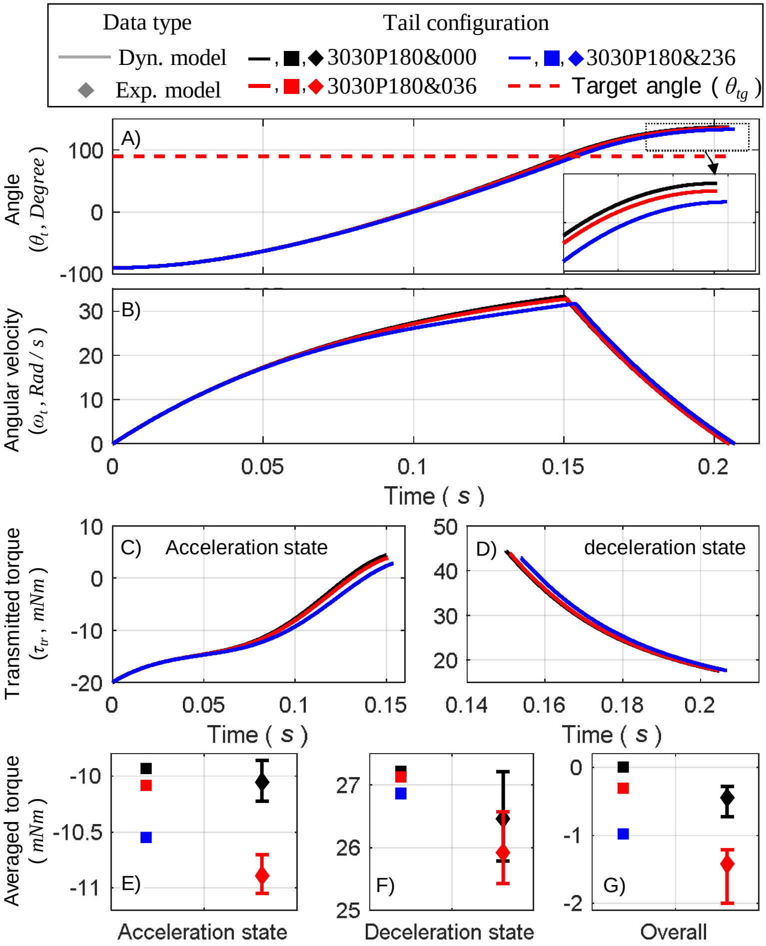

Figure 3.5.: Unbalanced distal mass type tail with partial oscillation. The tail is accelerated with a input torque of contant voltage, V_{in}=12 V, from the initial angle, θ_i = -90^o, to target angle, θ_{tg} = 90^o. After the target angle, the direction of the input voltage is changed to the opposite direction with the same voltage (V_{in}=-12 V) for the deceleration. A) Angular position of the tail, B) Angular velocity of the tail rotation, C) and D) Transmitted torques at the body from the tail during acceleration and deceleration, respectively, E) and F) Averaged transmitted torques during the acceleration and deceleration, respectively, G) Averaged transmitted torque after full acceleration and deceleration. This result is free from the gravity. The legend follows a rule given in Table 3.2. These results are from the dynamic model.

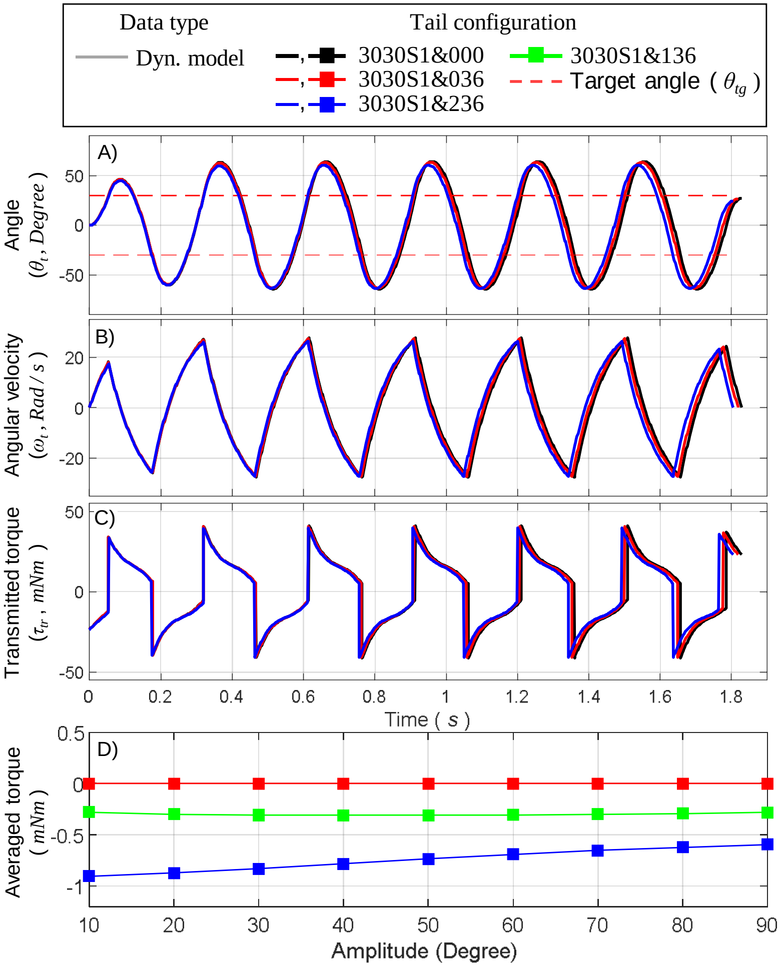

Figure 3.6.: Unbalanced distal-mass type tail with symmetric oscillation. The tail is oscillated within the amplitude with a input torque of constant voltage, $V_{in} = \pm 12\ V$. The amplitude has the positive and negative target angles, θ_{tg}. After the target angle, the direction of the input voltage is changed to the opposite direction with the same voltage for the deceleration. The direction of the changed input voltage is continued to the next target angle. A) Angular position of the tail, B) Angular velocity of the tail oscillation, C) Transmitted torques at the body from the tail, Results of A), B), and C) have the amplitude as 60^o (target angle $= \pm 30^o$), D) Averaged transmitted torque according to the amplitudes. This result is free from gravity. The legend follows a rule given in Table 3.2.

3.2.2. Unbalanced distal mass tail with symmetric and asymmetric oscillations

Within the constraints of limited rotation, two additional operation strategies can be used: symmetric (Figure 3.6) and asymmetric (Figure 3.7) oscillations. In both cases, a full period oscillation is performed, however, the symmetric oscillation uses equal voltages in both directions, whereas asymmetric operation uses different voltages in each direction. In symmetric oscillation operation in still air, the inertial torques are conserved and aerodynamic torques cancel out resulting in no change to the body's angular momentum. Operating the tail with asymmetric voltages however, allows for a more efficient utilization of the aerodynamic forces.

Figure 3.7A shows the schematic view of the asymmetric oscillation operation, where the input motor voltage is varied based on the direction of rotation. The inertial component is still conserved, therefore resulting in zero net torque contribution; as seen in Figure 3.7B configurations 3030S1&000, 3030A2&000, and 3030A3&000. However, the aerodynamic forces are not symmetric and result in a net torque on the body in still air, as seen in Figure 3.7B configurations 3030S1&036, 3030A2&036, and 3030A3&036. The generated net torque is in the direction of the smaller input voltage, and the larger the difference in voltages, the larger the net torque generated. Increasing the amplitude of the aerodynamic tail's oscillations, θ_r, will further increase the net torque, as larger amplitudes allow for more time at higher velocities, accentuating the differences between the aerodynamic forces in each direction.

If external airflow is present, due to locomotion or environmental flows, the torques will be biased in the direction of airflow resulting in a net torque on the body during symmetric oscillation as seen in Figure 3.6D configurations 3030S1&036, 3030S1&136, and 3030S1&236; increasing the flow increases the bias, however, if the symmetric oscillation is symmetric to the flow, the result of the external flow with cancel out. External airflow during asymmetric oscillation can both increased, flow opposite the larger voltage direction, or decreased, flow opposite smaller voltage direction, the

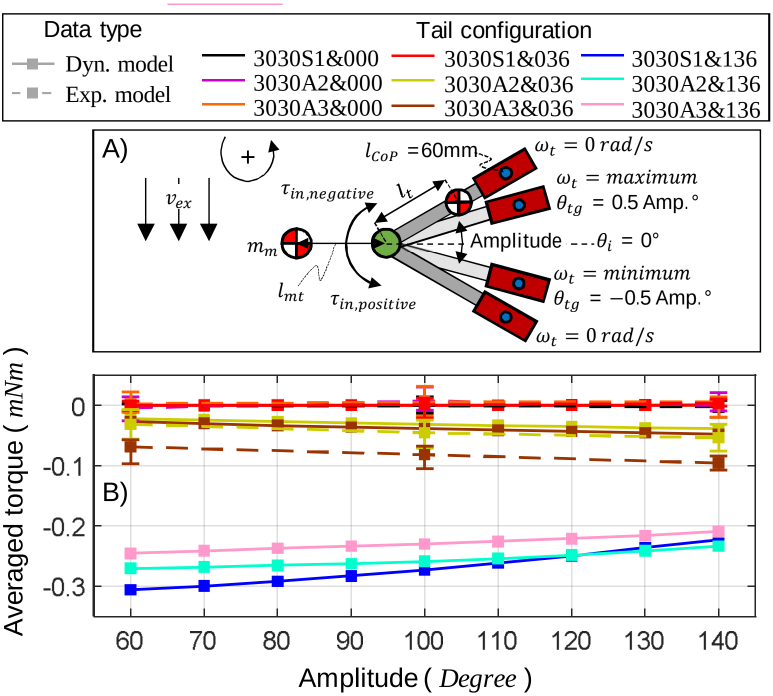

Figure 3.7.: Unbalanced distal mass type tail with asymmetric oscillation. Amplitudes of the symmetric and asymmetric oscillations are between the positive and negative target angles, θ_{tg}. A voltage to stop the tail after reaching the target angles (zero angular velocity, ω_t) is the same during the acceleration state, but opposite direction. Input voltages, V_{in}, in positive direction is always 12 V, but in negative direction is changed for the asymmetric operation. For example, 3030A2&000 has half voltage in negative direction (V_{in}=-6 V). A) Schematic view to describe the asymmetric operation of the unbalanced distal-mass type, B) Results from the dynamic and experimental models for the averaged torque according to the amplitude without gravity. The legend follows a rule given in Table 3.2. Examples of instantaneous and averaged torques for the asymmetric oscillation are shown in Figure 3.10.

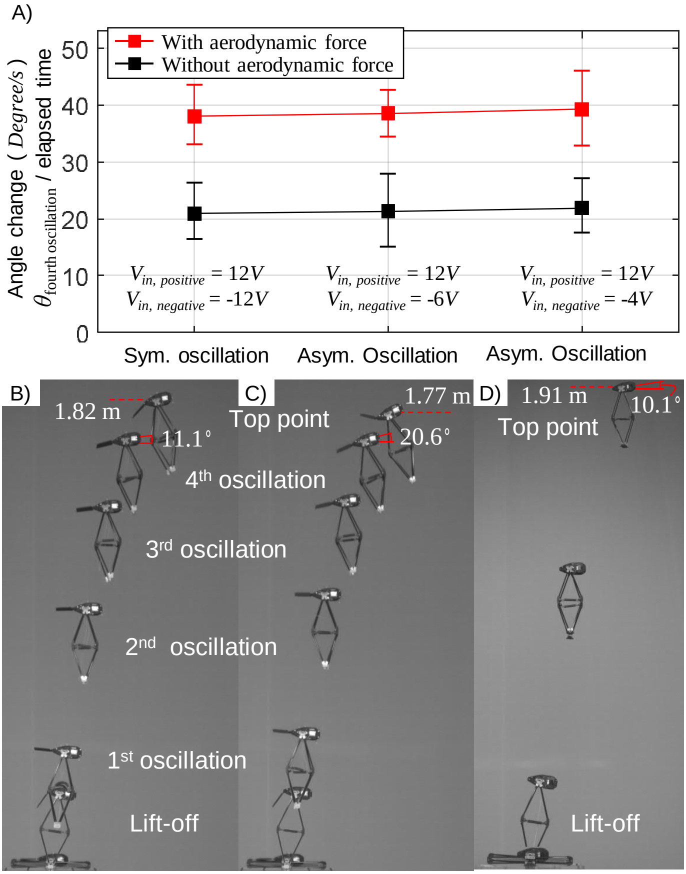

Figure 3.8.: Experimental performance results of the active tail on the jumping robot. A) Active tail performance results according to the different operating strategies of the active tail. Results are from 10 trials. Results indicate the changed angles normalized by the elapsed time during the 4th oscillation. Amplitudes of the oscillation are ± 30 degrees. B) Jumping without the aerodynamic forces on the active tail's asymmetric oscillation. Jumping heights at the top point and angles at the fourth oscillation for the asymmetric oscillation are 1.817 m and 11.9^o ($V_{in,positive}$ / $V_{in,negative}$ = 2), and 1.815 m and 12.1^o ($V_{in,positive}$ / $V_{in,negative}$ = 3). C) Jumping with the aerodynamic forces on the active tail's asymmetric oscillation. Jumping heights at the top point and angles at the fourth oscillation for the asymmetric oscillation are 1.775 m and 22.9^o ($V_{in,positive}$ / $V_{in,negative}$ = 2), and 1.774 m and 23.9^o ($V_{in,positive}$ / $V_{in,negative}$ = 3). D) Jumping without tail. Initial angle of the tail is always zero degree. The external flow to the active tail is the opposite direction of the body's moving direction.

net torque. While the tail generates biased torque with the external airflow, the external airflow changes the rotating speed of the tail. The tail rotation against the external airflow becomes slower, but the other direction is accelerated. The accelerated tail rotation transmits torque to the body in an undesired direction, and wide amplitude generates more undesired torque. As a result, asymmetric oscillation with the aerodynamic tail has wider applicability because it can generate continuous torque with or without the external airflow. Jumping locomotion creates significant changes in the external airflow and is therefore a good candidate for exploring the performance characteristics of tails. Figure 1.7 shows robot configurations, and Figure 3.8 presents the performance of the active tail on the robotic platform during jumping locomotion. The robot uses a spring and four-bar mechanism to store and release the jumping energy [14], and an aerodynamic unbalanced distal mass type tail operated by symmetric and asymmetric oscillation strategies for pitch control. As the asymmetry in the operation increases we see a increased rate of the angle change in the Figure 3.8A.

3.2.3. Unbalanced distal mass tail with full rotation

Assuming an unrestricted tail operation, the unbalanced distal-mass type tails (i.e., configurations of 3030F1500&000, 3030F1500&036, and 3030F1500&236 in Figure 3.9) can be operated in continuous rotation. A major difference between the characteristics of single and continuous rotation tails, is that a single rotation is not sufficient for the tail to reach steady-state operation (i.e., accelerating the entire time). I define steady-state operation as the point where the angular acceleration of the tail reaches 5 rad/s^2, around 1% of the maximum acceleration. As shown in Figure 3.9B, this occurs at approximately the first complete rotation, but it is dependent on the system parameters (e.g., rotational inertia and motor torque) and external airflow. During steady state, the tail has zero angular acceleration and constant angular velocity, therefore, it does not generate the torques that are proportional to the angular acceleration, such as τ_I and τ_T (equation (3.5)). In the case of an inertial tail, the tail only generates torques from the centrifugal

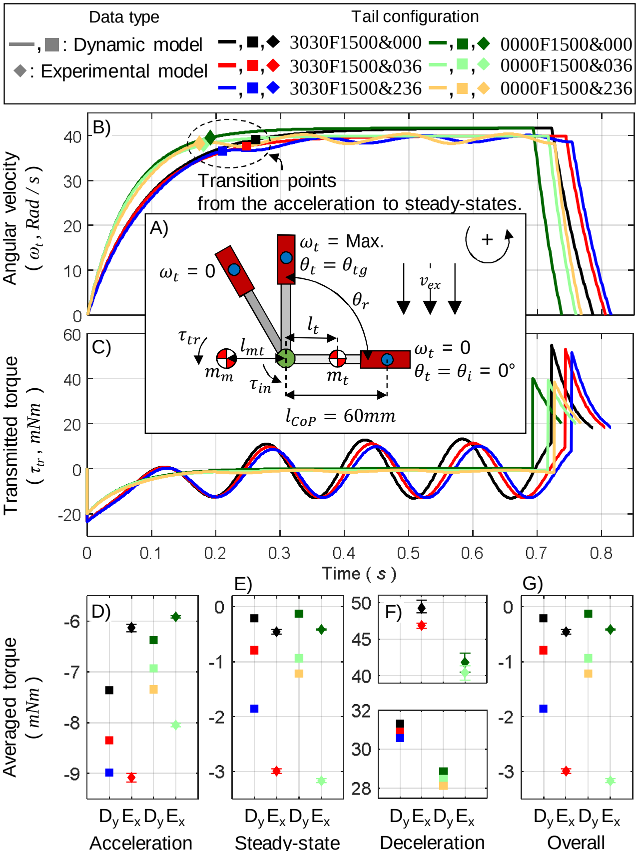

Figure 3.9.: Unbalanced distal- and balanced-mass type tails with full rotation. The tail rotates continuously from the initial angle, θ_i, of zero degree with a input torque of constant voltage, V_{in}=12 V to the target angle, θ_{tg} = 1500^o. When the tail rotation reaches the target angle (zero angular velocity, ω_t), the input voltage is changed in the opposite direction with the same voltage (V_{in}=-12 V) for the deceleration. A) Schematic view for the tail operation, the transition from the acceleration and steady states occurs at 414.5^o (3030F1500&000), 376^o (3030F1500&036), 291.9^o (3030F1500&236), 310.6^o (0000F1500&000), 281.3^o (0000F1500&036), and 262.7^o (0000F1500&236), B) Angular velocity of the tail, C) Transmitted torque at the body from the tail, D), E), and F) Averaged transmitted torque during acceleration state, steady-state behavior, and deceleration state, respectively, G) Averaged transmitted torque after the full cycle of the acceleration and deceleration. This result is free from gravity. Results from the experimental model are from 5 trials, and indicated with error bars. D_y and E_x denote dynamic and experimental results, respectively. The legend follows a rule given in Table 3.2.

forces, τ_C, during steady state (Figure 3.9C); and, the angular momentum of the body from the acceleration state is maintained. The aerodynamic forces however still exist, and can increase the transmitted torque in the opposite direction of the tail rotation during steady state. These forces are proportional to the square of angular velocity of the tail and airflow. As a result, the aerodynamic tail can transmit more torque in the opposite direction of the tail rotation than the inertial tail As shown in Figure 3.9G.

3.2.4. Mass-balanced tail with full rotation

The last tail type is a mass-balanced tail in which the CoM is located at the tail's rotation point. The transmitted torque of this type of tail can be partially decoupled from the tail's angular position, however, if the tail's CoM is located at the CoM of the robot body, the transmitted torque is entirely decoupled from the angular position of the tail. This type of the inertial tail transmits only the torque from the moment of inertia, τ_I, during the acceleration and deceleration states. During steady state, the angular acceleration and transmitted torque become zero as shown in Figure 3.9C. Therefore, the robot body's angular momentum is only from the acceleration state. As before, the inclusion of aerodynamic forces to an inertial tail can increase the transmitted torques in the opposite direction of the tail rotation during both the acceleration and deceleration states in addition to creating torque during steady state (Figure 3.9D-G); all of which accentuated by external airflow. The tail configurations of 0000F1500-&000, 0000F1500&036, and 0000F1500&236 in the Figure 3.9 present the performance of the mass-balanced type tail operating in continuous rotation, where again steady-state operation is the point where the angular acceleration of the tail reaches 5 rad/s^2 (around 1% of the starting acceleration).

3.3. Discussion

The performance of an active tail is a function of the tail type (balanced-mass and distal-mass), the operation strategy (partial oscillation, symmetric oscillation, asymmetric oscillation, and full rotation), and the incorporation of aerodynamic components. Figure 3.10 shows the experimental results of different combinations of the tail type, operating strategy, and incorporation of the aerodynamics. Figure 3.10A presents the instantaneously transmitted torque at each point in time, Figure 3.10B shows the average of all transmitted torques up to that moment in time. I discuss the best combination of the tail configurations by separating the tail operation into limited and unlimited operations.

Limited operation tail: Limited operation has a limited time and rotation angle. Three operation strategies are available for this type of tail: partial oscillation, symmetric oscillation, and asymmetric oscillation. In severely limited cases only partial oscillation may be possible (3030P30&000 and 3030P30&036). During a partial oscillation the transmitted torque is dominated by the first acceleration and deceleration phases with no steady-state operation. The maximum angular momentum of the body is when the direction of transmitted torque changes in Figure 3.10A,B. This is because the angular momentum is proportional to the integration of the transmitted torque ($I\omega \propto \int \tau_{tr}$). Given that energy is conserved, the angular momentum of the body after a complete acceleration and deceleration equals zero and the change in body angle is maximized. Therefore, the optimal tail operation is when the acceleration and deceleration times are the same as the required dynamic control time to avoid over and under tail design. In addition, the distal-mass tail can generate more averaged torque than the balanced-mass tail as seen in Figure 3.10D (comparing 3030P30&000 and 0000F1500&000). The balanced-mass tail generates torque only from the moment of inertia, however the distal-mass tail generates torque from both the moment of inertia and the tangential and centrifugal forces. Contribution from the tangential and centrifugal forces increases the averaged torque. Incorporating an aerodynamic component to the tail further increases the averaged transmitted torque, resulting in the averaged torque of the configurations in Figure 3.10 (3030P30&000 and 3030P30&036) being increased

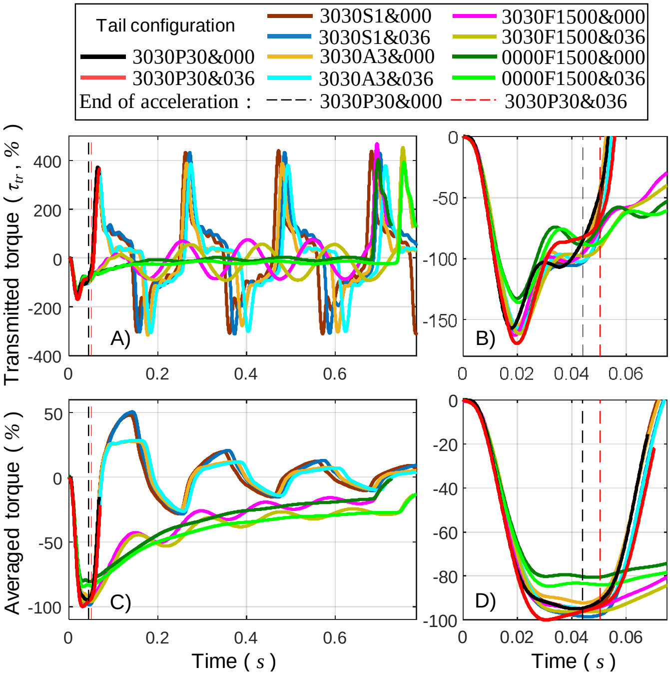

Figure 3.10.: Experimental results of different tail configurations and operating strategies. The initial angle, θ_i, of the tail is 0 degrees. The amplitude of symmetric and asymmetric oscillations is ±30 Degrees. Black and red dotted lines denote a time to separate limited operation and unlimited operation ranges. A) Transmitted torque from the tail operation, B) Zoomed view of the transmitted torque for the limited operating range. C) Averaged torque from the tail operation, D) Zoomed view of the averaged torque for the limited operating range. Values are normalized by the maximum averaged torque (= -17.4072 mNm) among all candidates. The legend follows a rule given in Table 3.2.

by 1.58 % at the maximum angular momentum point.

If the operating time is unlimited, but the rotation angle is limited, there are three available operating strategies: partial oscillation, symmetric oscillation, and asymmetric oscillation. While the partial oscillation generates the torque in a single time within the limited rotation angle of the tail, symmetric and asymmetric oscillations can generate multiple control torques. Transmitted torques from the symmetric oscillation (3030S1&000 and 3030S1&036) were shown to cancel out, resulting in zero net torque with a pure inertial and aerodynamic tail. However, external airflow can bias the averaged torques resulting in non-zero net torque. Asymmetric oscillation (3030A3&000 and 3030A3&036) with the pure inertial tail has the same results. However, incorporating the aerodynamics to the asymmetric oscillation can bias the averaged torque in the desired direction due to differences in the energy consumption in the positive and negative directions. In addition, as before, external airflow can increase the performance of the asymmetric oscillation. As a result, partial oscillation is less suitable for the dynamic motion control under an operating condition of limited rotation angle and unlimited operating time because it cannot generate continuous control torques. Therefore, asymmetric oscillation with an aerodynamic tail is the best strategy.

Unlimited operation tail: A continuous rotation tail has unlimited operating time and rotation angle. While its possible to use any of the tail operation strategies, symmetric oscillation, asymmetric oscillation, and full rotation are more suitable as they create continuous control torques; where the torques created are based on different parameters. While the symmetric and asymmetric oscillations generate the body's angular momentum with the difference of transmitted torques in the positive and negative direction, full rotation generates angular momentum during the acceleration, then keeps it during the steady-state operation. Deceleration of the full rotation removes the angular momentum due to energy conservation. Therefore, the averaged torque from the symmetric and asymmetric oscillations (3030S1&000 and 3030A3&000) are smaller than full rotation (3030F1500&000 and

0000F1500&000) as seen in Figure 3.10C. The two oscillatory operations will also necessarily cause an oscillation in the body angle which may hinder other tasks as seen in Figure 3.10C (3030S1&000, 3030A3&000, 3030S1&036, and 3030A3&036). However, the full rotation operation can avoid this body oscillation as seen in Figure 3.10C (3030F1500&000, 0000F1500&000, 3030F1500A036, and 0000F1500&036). Even though the full rotation with a distal-mass tail (3030F1500&000 and 3030F1500&036) generates a sinusoidal averaged torque during steady-state operation, the direction of the torque is constant. As a result, the full rotation is the best operation strategy under the unlimited operation condition. In addition, while the pure inertial tail generates zero net torque during the steady-state operation due to the zero angular acceleration, the aerodynamic tail generates continuous torque based on the the maximum angular velocity. Therefore, incorporating the aerodynamics with the inertial tail generates more control torque with a full rotation.

3.4. Summary

An active tail provides additional DOF and external forces to the robotic platform for dynamic motion control. In this chapter, I characterized a single-axis active tail through a derived dynamic model, exploring the design parameters of the active tail, comparing the performances of inertial and aerodynamic tails, and categorizing the types of active tails according to their operating strategy and configurations. Experimental results verified the trends observed in the dynamic model.

I highlighted and analyzed the roles of the tail design parameters in generating and transmitting torques to the body. In addition, I observed the characteristics of the operating strategies by comparing the performance changes between inertial and aerodynamic tails. While the inertial tail has limited operating strategies to generate torques for reorientating the body due to the energy conservation, incorporating aerodynamics with the inertial tail is not bound by energy conservation, and works under a wider range of operation strategies. This chapter provides the initial design inspiration for developing an active tail to suit the specific locomotion requirements of robots. Future work will focus on studying the characteristics of a flexible tail, which is common in nature, and may have better performance than a rigid tail. Additionally, the tail's dynamic characteristics in 3D space will be explored.

CHAPTER

4

ENHANCED NON-STEADY GLIDING PERFORMANCE THROUGH OPTIMAL AIRFOIL CONFIGURATION AND CONTROL STRATEGY

H Kim, M A Woodward, M Sitti, "Enhanced Non-Steady Gliding Performance of the MultiMo-Bat through Optimal Airfoil Configuration and Control Strategy", IEEE/RSJ International Conference on Intelligent Robots and Systems (IROS), 2018, pp. 1382-1388. [78]

Many robots make use of gravitational potential energy, generated by another mode, to enhance mobility through gliding locomotion. However, unstructured environments can create situations in which the initial conditions for steady-state gliding cannot be achieved; for example, jumping out of a hole, where the obstacle is very close to the robot. This paper suggests an optimization methodology for finding airfoil configurations and control strategies to maximize the effective non-steady-state gliding ratio for the most challenging initial condition, that of zero velocity. Parameters for the optimization are a location of a robot's center-of-mass in relation to its center-of-pressure and, through the addition of a tail, an active pitch control strategy. The optimal center-of-mass location produces the best passive gliding performance (morphological intelligence), and the optimal control strategy improves the gliding distance. Due to the aerodynamic complexities of modeling the collapsible airfoils, I find the optimal location of the center-of-mass from gliding experiments performed on the robot at different center-of-mass locations and initial pitch angles. An optimal location of the center-of-mass was found to be 40 % of the wing chord for our robotic platform; measured from the wing's leading edge. The optimal location has a wide range of initial pitch angles which result in stable, yet non-steady-state, gliding behaviors. The morphological intelligence built into our robotic platform creates two observable dynamic behaviors, that of horizontal velocity gain and sink rate minimization. I then estimate the drag coefficients from the experiments, and conduct dynamic simulations to optimize the pitch control strategy. The design methodology presented here can enhance the non-steady-state gliding performance of a broad range of gliding robots, and the control strategy can further enhance performance on those which utilize an active tail. As co-authors, Prof. Matthew A. Woodward and Prof. Metin Sitti contributed to the discussions and edited the manuscript. The results of this chapter are previously published from reference [78].

4.1. Gliding experiments

Experiments are conducted to understand the gliding behavior of the jumping-gliding robot in this work, as the aerodynamics of the collapsible airfoils are difficult to model. Through observations of the gliding performance, optimal wing configurations and key dynamic behaviors can be extracted. These dynamic behaviors will then form the control policies employed later for active gliding.

4.1.1. Experimental procedure

Each trial begins by dropping the robot with zero initial velocity at a specific initial pitch angle and wing configuration. The robot is dropped by hand from 2.8 *m* where each configuration is tested 5 times. A motion capture system (Vicon, Vantage V5) captures the gliding motion of the robot as seen in Figure 1.12. Yaw and roll angles start from zero degrees, and their variation during the tests was ±5 degrees which can be negligible.

Figure 1.4 introduces the configuration of the airfoil in the robot [14]. The mechanism has integrated thin membrane airfoils to generate the lift and drag forces for gliding flight. As shifting the robot's center-of-mass (CM_R) is difficult I instead changed the position of the leading edge of the wing and thus the relative position of the range of the center-of-pressure (CP); the folding lines are shown in the Figure 1.4. The location of the CM_R is varied from 30 % to 50 % of the wing chord length, measured from the leading edge, and the initial pitch angle is varied from the onset of unstable gliding, -50 to 30 degrees depending on CM_R position, to 80 degrees; positive indicates nose down.

4.1.2. Basic passive gliding concept

Figure 4.1a presents the position of the center-of-pressure which moves along the chord-direction of the airfoil as a function of the angle-of-attack (AoA). All position percentages of the CM_R and CP, from this point on, are coupled as both are measured from the wing's leading edge. The motion of

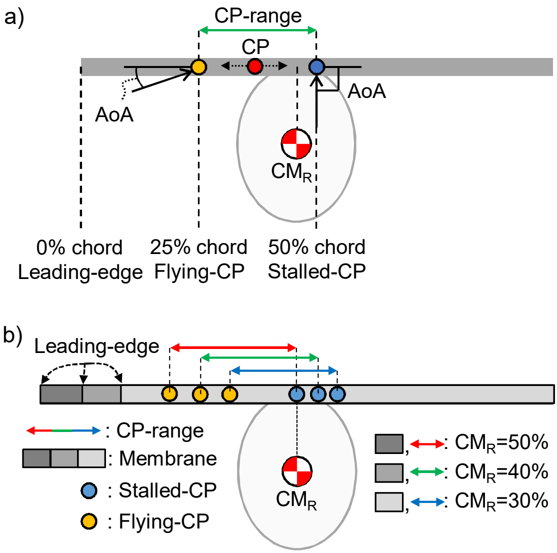

Figure 4.1.: Basic concept of the passive gliding. a) Change of CP locations with the AoA change. b) Change of the CP range about different locations of the CM$_R$ from the leading-edges.

the CP is caused by changes in the pressure distribution over the airfoil and can move from approximately the flying-CP of 25 % (AoA ≈ 5 to 15 degrees) to the stalled-CP of 50 % (AoA = 90 degrees) chord, creating a CP-range. The lower bound comes from flat plate theory and represents a flying flat plate airfoil, whereas the upper bound represents a completely stalled span wise symmetric airfoil; where cambered airfoils can shift the lower bound and associated AoAs.

Figure 4.1b presents the possible CM$_R$ locations in relation to the wing chord, subdivided into three regions. These represent CM$_R$, in front of the flying-CP (free fall), between the flying and stalled-CP (gliding), and behind the stalled-CP (direction switch). For the special case where the CM$_R$ equals 50 % chord, the resulting behavior is parachuting, Figure 4.3a, where the robot does not free fall but does not move in a particular direction.

The airfoils of the robot, being highly integrated into the other structures, makes shifting their relative position on the robot body difficult. Therefore, to change the relative position between of the CM_R and CP-range, I instead shift the leading-edge position through folding of the front part of the wing. This process also changes the area of the wing and therefore couples the gliding performance to both the wing area and CM_R position, as seen in Figure 4.1b.

4.1.3. Optimal location of the robot's center-of-mass (CM_R)

The gliding region of Figure 4.1a can be further subdivided into stable and unstable gliding regimes (see Figure 4.2), where unstable behaviors are caused by significant imbalances between the nose-up and nose-down pitching moments. This is primarily caused by locating the CM_R too close to either the flying or stalled-CP, however, high rotational rates can shift the behavior of cases near the boundaries between stable and unstable gliding. There are two types of unstable pitch behaviors: under and over-rotations.

Under-rotation means that the robot pitches overly nose-down; as seen in the blue area of Figure 4.2. I define this behavior as when the AoA becomes less than 0 degrees during the glide. This occurs when the CM_R is too close to the flying-CP, resulting in a small pitch-up moment arm and insufficient restoring torque; as seen in Figure 4.3a where CM_R=30 % shows little change in pitch angle. I did not conduct experiments for under-rotation, as the behavior is similar to a free fall. This is the most damaging behavior as impact velocities are high, 4.3a, and the gliding ratios are low, as seen in Figure 4.3b.

Over-rotation means that the robot pitches overly nose-up, as can be seen in the red area in Figure 4.2. I define this behavior as when the AoA becomes larger than 90 degrees during the glide. This occurs when the CM_R is too close to the stalled-CP, resulting in a small pitch-down moment arm and insufficient restoring torque; as seen in Figure 4.3a where CM_R=45 % shows significant initial pitch-up behavior. This results in high drag in the motion direction but does not result in free fall and therefore produces slightly better gliding ratio than the under-rotation case.

Stable-rotation means the robot pitches neither too far nose-down or nose-up during gliding, as can be seen in the gray area in Figure 4.2. I define this behavior as when the AoA is between 0 to 90 degrees during the glide. This region produces the best results, both in terms of impact velocities and gliding ratios; as seen in Figure 4.3, CM_R=35 % and CM_R=40 %.

The experimental results show that a CM_R location of 40 % has the widest range of initial pitch angles which generate stable-rotation and higher gliding ratios than other locations, about nearly all of the initial pitch angles. However, this optimal location is specific to the robot in this work and its airfoil design and therefore may be different, requiring recharacterization, for other platforms.

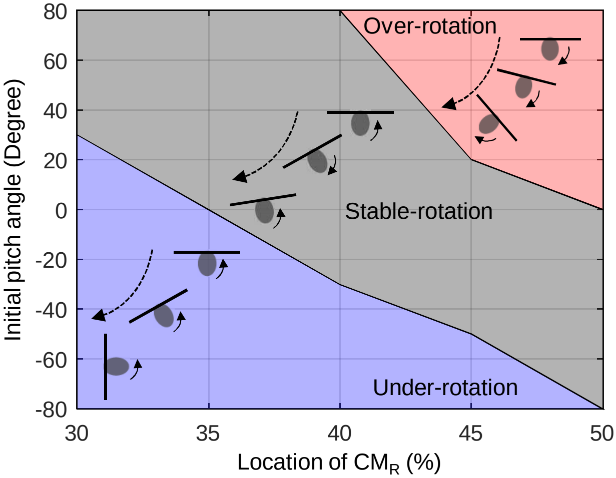

Figure 4.2.: Pitch rotation types with different wing configurations and initial pitch angles. The initial drop height is 2.8 m. See media extension 1 attached in [78]

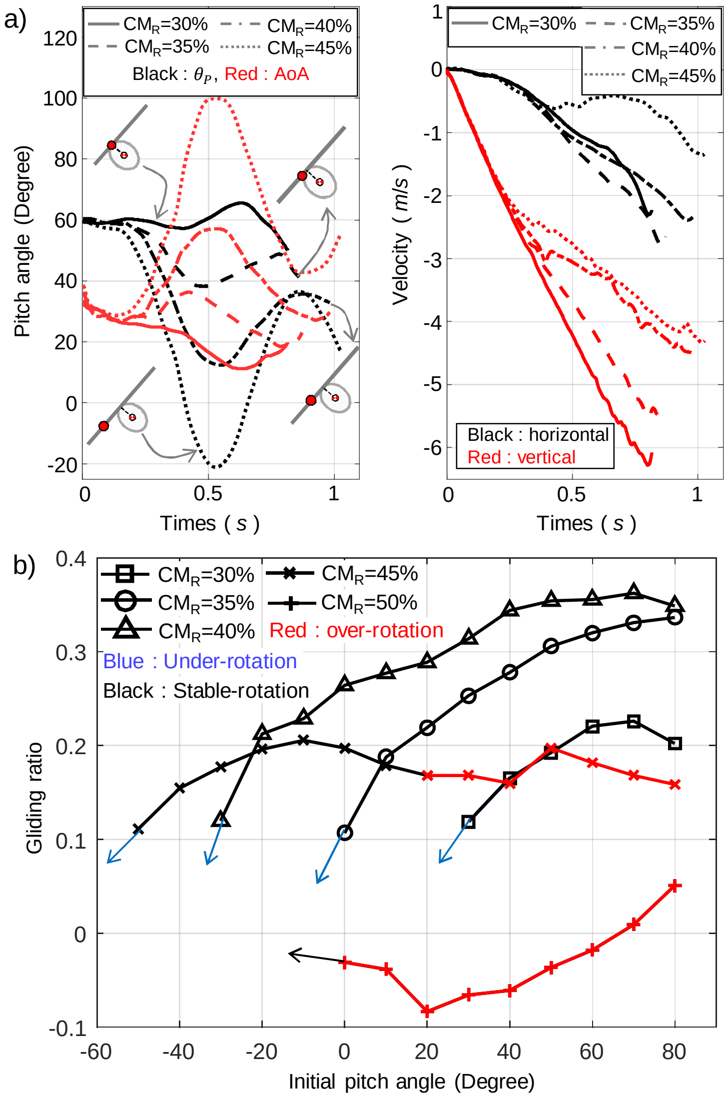

Figure 4.3.: Experimental results of the passive gliding performances. a) Gliding behaviors with different gilding conditions. Left and right figures denote the pitch behaviors and velocities, respectively. b) Gliding ratios for different CM$_R$ locations and initial pitching angles. The initial drop height is 2.8 m. See media extension 1 attached in [78]

4.1.4. Observed gliding behavior primitives

Observed from the gliding experiments, the gliding trajectories can be categorized into two regimes by the relative position of the CP at the onset of gliding and the CM_R. First, when the initial CP is behind the CM_R, ICB (dotted lines in Figure 4.4), the pitch angle is initially increased (nose-up), after which the pitch angle is reduced (nose-down). Whereas the second case is the reverse, the initial CP is in front of the CM_R, ICF (solid lines in Figure 4.4), and the pitch angle is initially reduced (nose-down), after which it is increased (nose-up).

The experimental results in Figure 4.3b show ICF as the best regime which is due to the lift-to-drag ratio being more heavily weight towards propulsive horizontal drag, as evident by the higher horizontal velocities (Figure 4.4b, solid lines), whereas the ICB is more heavily weighted towards lift, as evident by the slightly lower vertical velocities (Figure 4.4c, dotted line). Negative initial pitch angles (nose-up) result in initial resistive drag creating motion in the opposite direction (Figure 4.4b, positive velocities). However, the horizontal velocity gain dominates the behavior, resulting in better performance for the ICF regime.

To extract control policies the passive gliding trajectories are segmented into dynamically similar regimes, where the first regime focuses on increasing horizontal velocity (Policy 1, P1) and the second focuses on minimizing the sink rate (Policy 2, P2). For the robot in this work, the separation of these policies occurs at 0.2 s and ends at 0.6 s when the robot again switches the pitching direction. The timeframe of each policy is, therefore, 0-0.2 s and 0.2-0.6 s, respectively, as can be seen in Figure 4.4.

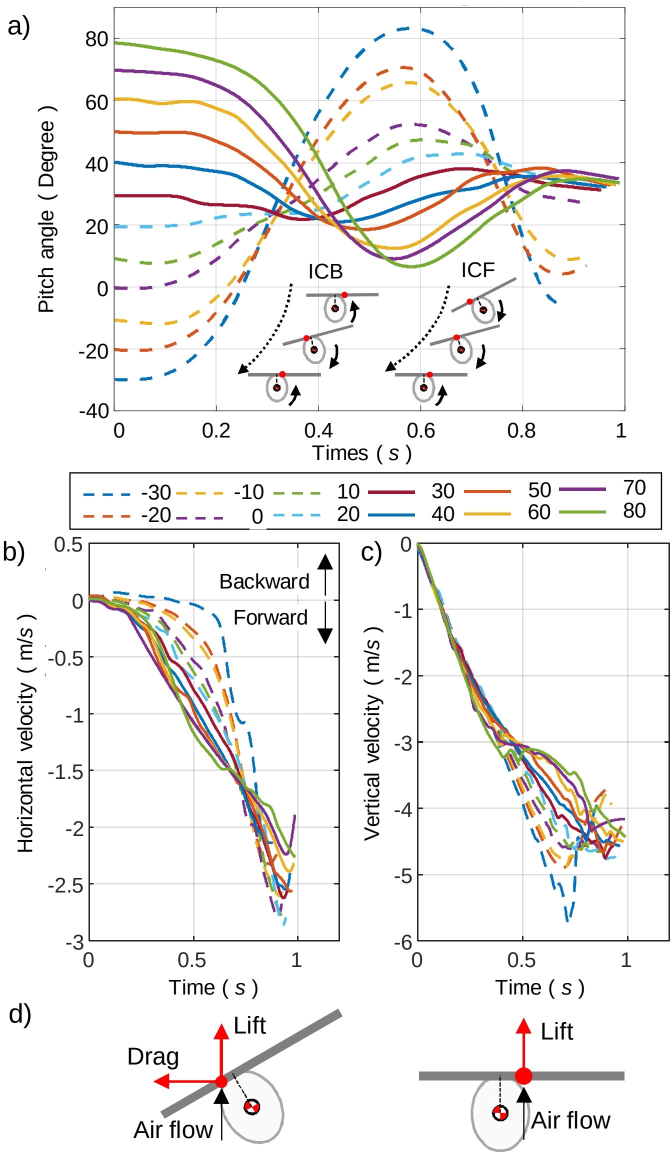

Figure 4.4.: Experimental gliding behaviors with a CM_R location of 40 %. a) Pitch behaviors with different initial pitch angles. b) and c) denote the horizontal and vertical velocities, respectively. d) Policies of the control strategy. Dotted and solid lines denote results of ICB and ICF behaviors, respectively. See media extension 1 attached in [78]

4.2. Dynamic simulations

To work with the passive dynamics, the pitch control strategy is, therefore, to find the optimal switching time between the policies to maximize the gliding ratio. However, to facilitate design, a dynamic simulation is employed to determine the gliding performance at different configurations and transition timings. The derived dynamic equation, a differential equation, is solved by ODE45 function, as provided in Section D of AppendixD.

4.2.1. Estimation of drag coefficients

The simulation employs a standard single body 2D dynamic simulation of the optimal passive gliding configuration, that of CM$_R$=40 %. However, to tailor the simulation to a specific robot requires calculation of the lift, C$_L$, drag, C$_D$, and moment, C$_M$, coefficients about the aerodynamic center; assumed fixed at 25 % chord position. To overcome the challenges of simulating complex airfoils and aerodynamics, I will estimate the coefficients from the experimental data. However, for our purposes I will determine a body frame lift, C$_{AD}$, inertial frame horizontal, C$_Y$, and body frame pitching moment, C$_M$, coefficient.

The free body diagram of the robot is shown in Figure 4.5, where Table 4.1 describes its specifications. I defined a flow vector, $\vec{f}$, which is the negative of the robot's velocity vector in the inertial frame as,

Table 4.1.: Specification of the robot

Specification	Value	Specification	Value
m_r	190 g	w_l	258 mm
l_{mw}	23.24 mm	w_w	270 mm
θ_{mw}	90 degrees	I_{pitch}	0.2 $e^{-3} Kg.m^2$

$$\vec{f} = -\dot{y} - \dot{z}i - \dot{\theta}_p(l_{mw}e^{(\theta_p+\theta_{mw})i} + l_{cp}e^{(\theta_p+\pi)i})e^{(\frac{\pi}{2})i}, \tag{4.1}$$

where $\dot{y}$, $\dot{z}$, and $\dot{\theta}_p$ are velocities in horizontal, vertical, and pitching directions of the robot, respectively. The l_{mw} is the length and θ_{mw} is the angle

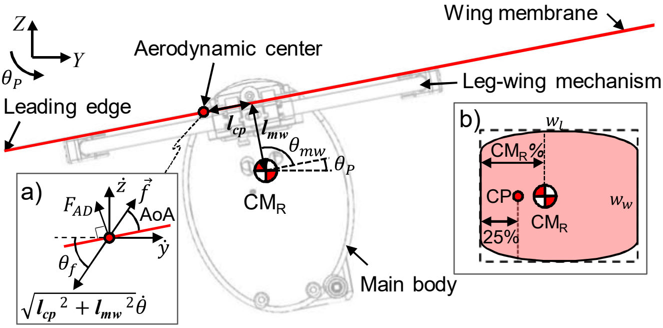

Figure 4.5.: Free body diagram for the robot's gliding. a) Velocity and force vectors at the center of pressure (CP); b) Variables on the wing membrane. CM$_R$ % is 40 as an optimal location of the CM$_R$.

between the CM$_R$ and the wing connection point. The l_{cp} is the length between locations of the CP and CM$_R$ along the chord defined as,

$$l_{CP} = \frac{w_l CM_R}{2(1-CM_R)} - CPc_l, \tag{4.2}$$

The chord length can be defined as

$$c_l = \frac{w_l}{2} + \frac{w_l CM_R}{2(1-CM_R)}, \tag{4.3}$$

where, c_l is the chord length, w_l is the symmetric chord length. The generated drag force of the air can be defined as

$$F_{AD} = C_{AD}(AoA)\rho A_{drag}\left|\vec{f}\right|^2, \tag{4.4}$$

where C_{AD} is a drag coefficient, ρ is a density of the air, and A_{drag} is the area of the wing. The drag force is perpendicular to the wing, as seen in Figure 4.5. The AoA can be defined as

$$AoA = \theta_f - \theta_p, \tag{4.5}$$

where, θ_f is the inertial frame angle of the flow vector, $\vec{f}$. The inertial frame dynamic equations are then defined as

$$m_r\ddot{y} = F_{AD}cos(\theta_P + \frac{\pi}{2})$$
$$m_r\ddot{z} = F_{AD}sin(\theta_P + \frac{\pi}{2}) - mg \tag{4.6}$$
$$I_{pitch}\ddot{\theta}_p = \tau_{AD} = C_M\rho A\left|\vec{f}\right|^2 + virtualtorque,$$

We can calculate the aerodynamic drag coefficients by transforming equations (4.4) and (4.6) as

$$C_{AD} = \frac{m_r\sqrt{\ddot{y}^2 + (\ddot{z}^2 + g)^2}}{F_{AD}}$$
$$C_M = \frac{I_{pitch}\ddot{\theta}_p}{\rho A\left|\vec{f}\right|^2}, \tag{4.7}$$

where m_r is mass of the robot and g and I_{pitch} are gravitational acceleration and moment of inertia in pitching direction, respectively. The ρ and A are the density of the air and area of the wing, respectively. The $\ddot{y}$, $\ddot{z}$, and $\ddot{\theta}_p$ are the measured accelerations from the gliding experiments in the horizontal, vertical, and pitching directions, respectively. The virtual torque simulates the contribution of a tail for pitch control in the dynamic simulation.

Figure 4.6a presents the final estimated drag coefficients in both the body and inertial frames, where the inertial frame coefficients are defined as

$$C_Y = C_{AD}(AoA)cos(\theta_P + \frac{\pi}{2})$$
$$C_Z = C_{AD}(AoA)sin(\theta_P + \frac{\pi}{2}), \tag{4.8}$$

The experimental and simulated results are compared in Figure 4.6b, where the dynamic behaviors are well captured. The difference between the two is cause by double differentiation of the motion capture data which adds significant noise, making exact determination of the coefficients difficult. However, with the tends captured, pitch control strategies are explored in simulation.

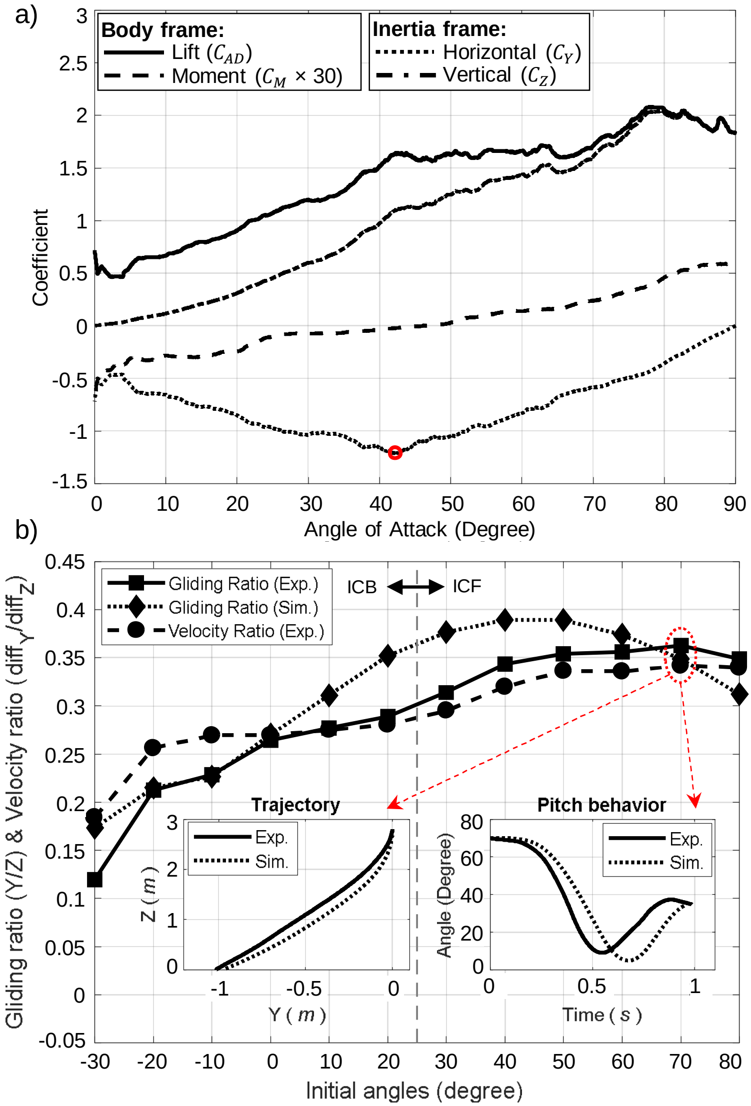

Figure 4.6.: a) Estimated drag coefficients from the experimental data. Red point is the optimal initial AoA (= 42.3 degrees). b) Comparison of the gliding ratios and root-mean-square (RMS) values of the velocity ratio for different initial pitching angles. Inside graphs are example to compare the results between the simulation and experiment (initial angle = 70 degrees). The location of the CM_R is 40 % chord from the leading edge.

4.2.2. Optimization of the control strategy

Active pitch control of a jumping and gliding robot, allows for control over three parameters including, the initial pitch angle at the onset of gliding, the pitch angle within each policy, and transition time between the two policies. The optimal values of these parameters will be determined using the simulation, as it facilitates a broader parameter search.

The first parameter is the initial pitch angle, where the initial condition of zero velocity results in an initial angle of flow of 90 degrees. From the extracted policies presented previously, the first policy, P1, is focused on increase horizontal velocity. Therefore, from Figure 4.6a, I find the optimal initial pitch angle of 47.7 degrees (AoA=42.3 degrees) which produces the maximum horizontal coefficient, C_Y, and thus maximum horizontal force.

The second parameter is the AoA during each policy. Figure 4.7 describes C_Y and C_Z according to the pitch (θ_P) and flow (θ_f) angles where the AoA, equation (4.4), is the difference between the two. If we assume that the robot is able to sense the flow angle, we can find optimal pitch angles, θ_P, to maximize the performances of each policy, P1 and P2. A PID controller is used in the dynamic simulations to control the pitch angle of the robot. As the robot starts to glide, the velocity in horizontal direction increases, and thus the angle of flow reduces requiring the controller to continuously update the optimal pitch angle (Figure 4.7a,b, red line). The output of the controller is the virtual torque to control the pitch behavior.

Finally, the third parameter, the transition time between the P1 and P2 policies must be optimized as each deal with a different aspect of the gliding trajectory; P1 being the horizontal velocity gain and P2 being the sink rate reduction. The transition time is swept from 0.1 s to the end of the glide, Figure 4.8a, at three different drop height levels including 2.8, 3.6, and 4 m. The results demonstrate the dependence on initial drop height to determine optimal transition times.

Figure 4.8a presents the combination of all three optimal parameters where Figure 4.8b presents a single trial (drop height=3.6 m, transition time=1 s) with associated optimal pitch values and robot control results.

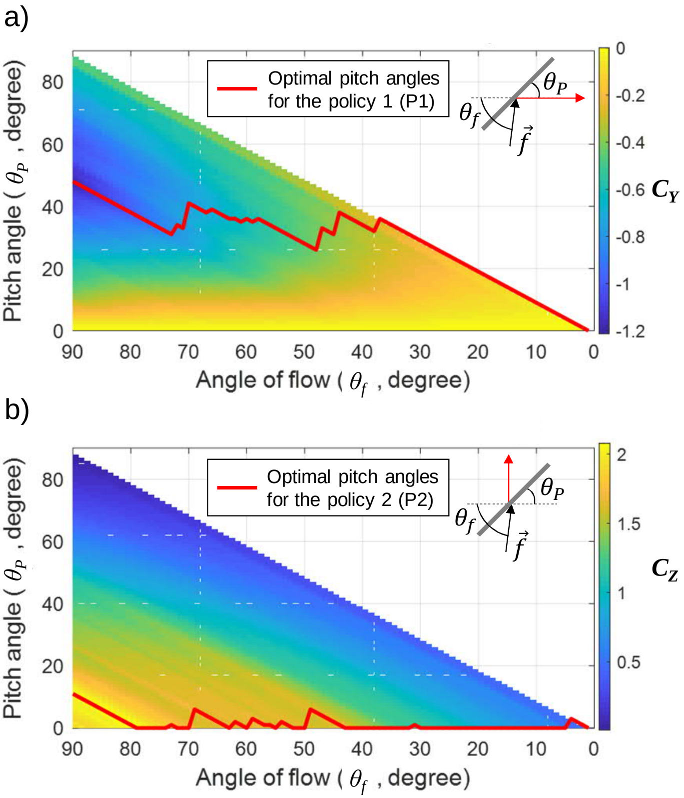

Figure 4.7.: Drag coefficients in horizontal (C_Y) and vertical (C_Z) directions according to the pitch (θ_P) and flow (θ_f) angles. a) Horizontal coefficients to the P1. b) Vertical coefficients to the P2. Red solid lines denote the optimal pitch angles for the best coefficients about the angles of the flow.

The overall gliding enhancement, 8.2 % (2.8 m), 11.9 % (3.6 m), and 18.5 % (4 m), is shown to be dependent on the drop height; more efficient use of the height potential energy is more pronounced for higher initial energies. The importance of the first policy, P1, can be seen in the preference for maintaining P1 for much of the glide. However, once sufficient kinetic energy has been accumulated, the gliding ratio can be further enhanced by focusing instead on the second policy, P2, where the kinetic energy is converted to drag keeping the robot aloft.

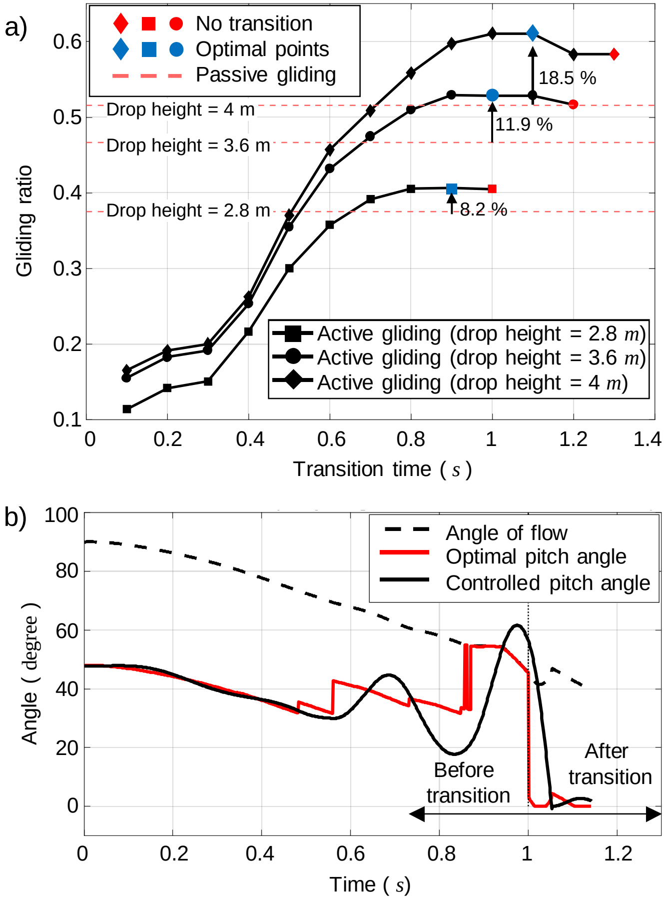

Figure 4.8.: Performances of the gliding motion with the control strategy found from the gliding experiments. a) Gliding ratios of active (controlled) and passive (uncontrolled) gliding about transition times of policies and drop heights. Improvement of the gliding ratios between the no transition and optimal points are 8.2 % (2.8 *m*), 11.9 % (3.6 *m*) and 18.5 % (4 *m*), respectively. b) Example of a pitch motion when the drop height is 3.6 *m* with 1 *s* of transition time.

4.3. Discussion

As the multimodal robot, the robot strategically integrates jumping-gliding, as seen in Figure 1.5. Although previous work studied interactions between integrated passive jumping and gliding [125, 15, 14, 13], this work employed the active tail to provide control torques to enhance agility during jumping. The pitch control allows the robot to have a favorable initial condition for gliding mode. As the first parameter, initial height for gliding, the transition of jumping and gliding modes occurs at the apex of the jumping trajectory to provide the maximum height. The transition takes time due to opening the leg-wing mechanism. In this sense, to use the given height efficiently, rapid mechanism opening minimizes the loss of transition time to transform the potential energy to the propulsion of gliding. The next parameter is the pitch angle at the apex of the jumping trajectory, the active tail can vary the pitch angles during the transition from pitch-controlled jumping to gliding. This chapter optimized the passive and active gliding dynamics to maximize the gliding distances, and provide the best initial pitch angle, which has to be provided by the jumping mode. The active tail can make the best pitch angle until the robot reaches the apex of the jumping trajectory. In addition, pitch control improves the gliding distance further.

4.4. Summary

This chapter has presented a methodology, demonstrated on the robot, for improving the gliding performance of miniature robots through both optimizations of the passive dynamics and active pitch control strategy. For a given platform the passive dynamics are defined by the relative position, along the wing chord, between the CM_R and the range of the CP. Two general policies were extracted from the passive dynamics; P1 focused on horizontal velocity gain, and P2 focused on sink rate reduction. Given the ability to active control pitch through the gliding phase, three more parameters were found which control the gliding performance including, the initial pitch angle, pitch angle during each policy, and transition time between policies.

Both the initial and policy pitch angles are shown to be platform specific whereas the transition time between policies is also dependent on the initial height.

CHAPTER 5

CONCLUSION AND FUTURE OUTLOOK

This dissertation developed a multimodal robotic platform to integrate jumping, perching, and gliding. This work aims to enhance the robot's performance for maneuverability in unstructured environments, such as disaster sites, to provide services for humans by replacing dangerous tasks. For this purpose, motion integration improves an ability to overcome various obstacles, extends possible operating conditions, and provides specific functions during locomotion modes. This dissertation reported two main tasks to improve the performance of multimodal locomotion: mechanical designs for components and dynamics, and studying the strategical integration of locomotion modes.

5.1. Thesis Contributions

Mechanical design

The design tasks conducted for the perching mechanism (Chapter 2), active tail (Chapter 3), and gliding dynamics (Chapter 4). The design tasks integrate locomotion modes and improve each mode's performance.

This work integrates the perching mode into the jumping robot by developing a bioinspired perching mechanism. The developing process includes the mechanism's characterizations according to the design parameters and perching conditions. Like the scenario in Figure 1.5, the perching occurs at the apex of the jumping trajectory to minimize the vertical velocity during perching. To improve the success rate of the perching with passive jumping, the design process of the perching mechanism considers the initial perching angle and speed, which are determined by jumping mode. As a result, the designed perching mechanism provides robust performance on various surface types and improvements in multimodal locomotion. Detailed results and conclusion are mentioned in Chapter 2.

Employing an active tail for an additional degree of freedom improves the robot's agility. The single-axis active tail generates control torque for the body's pitch orientation. The control torque for pitch orientation can improve the performance of each locomotion mode, such as gliding angle control for longer gliding distances, and overall multimodal locomotion by providing favorable initial conditions for the following locomotion mode, such as initial perching and gliding angles. For these purposes, this dissertation conducted active tail characterization according to design parameters, aerodynamic effects, and operating strategies. Through characterization, this dissertation provides initial design inspirations. Chapter 3 includes detailed results and conclusions.

Different airfoil configurations generate different passive gliding behaviors, and this work improves the passive gliding performance through airfoil design. In addition, with the active tail, this work observed the best strategy to control the gliding angle for the gliding distances. Chapter 4 includes the detailed design results for the passive and active gliding dynamics.

Strategical integration of locomotion modes

This work studied interactions between the integrated locomotion modes to improve the performance of multimodal locomotion. This dissertation observed shared parameters during the transition between modes and established the strategical interactions for parameters.

The first case is the integrated jumping-gliding, as seen in Figure 1.5. Chapter 4 discussed strategical interactions during the transition. To use the given jumping height efficiently, the transition occurs at the apex of the jumping trajectory, which has the maximum potential energy, and the transition has to happen rapidly to transform as much of the potential energy into propulsion for gliding as possible. For the pitch angle, an active tail can provide pitch angle control during jumping, and the best pitch angle, which was optimized by Chapter 4, can be transferred to gliding as the initial gliding angle. As a result, strategical interaction can improve the performance of jumping-gliding, specifically gliding distance in this dissertation.

The second case is the integrated jumping-perching-jumping, as seen in Figure 1.6. Chapter 2 discussed strategical interactions about this motion integration. Initial perching angle and velocity significantly determine the success of perching. In the scenario, the initial conditions of the perching are determined by jumping behaviors. For this reason, the perching occurs at the apex of the jumping trajectory to minimize the vertical velocity, and parallel with surfaces as the best perching angle observed in Chapter 2. As the best passive jumping behavior to satisfy these requirements, jumping direction in 80 degrees had the proper interaction during the transition of jumping-perching like Figure 2.21. Chapter 2 showcases jumping-perching performance at various surface conditions, and the high success rates are achieved due to the strategical interaction for the best initial perching angle, as seen in Figure 2.19. After the perching, the robot jumps in the horizontal direction from the vertical surface and generates powerful initial velocity for the next locomotion mode, such as jumping and gliding. The initial velocity increases the jumping distance, furthermore, the distance can be increased further with additional gliding mode. As a result, strategic uses of system energy during the transition of locomotion mode can improve the performance of locomotion modes, and the maneuverability of the robot.

5.2. Future outlook

5.2.1. Jumping-perching-gliding

This work has already developed all the necessary mechanisms for jumping, perching, and gliding. To maximize the system's performance through motion integration, I am planning to integrate jumping-perching-gliding like Figure 1.6. As discussed in Chapter 2, horizontal jumping from the vertical surface after perching provides performance improvements in jumping distance and overcoming obstacles. However, if the additional gliding is integrated after the horizontal jumping, the jumping velocity will be a powerful initial velocity to increase gliding distances. In addition, optimizing the active tail is necessary for the strategical interactions between integrated modes through pitch angle control. The pitch angle control during jumping provides flexibility in jumping angles to provide the proper perching angles. For example, in Figure 2.21, the jumping direction in 80 degrees has a favorable perching angle at the apex of the jumping trajectory however, active pitch control during jumping allows the other jumping direction to have the same favorable perching angles. In addition, control of the gliding angle improves gliding distance further, as discussed in Chapter 4. With the design of some appendages, such as an opening for the leg-wing mechanism during jumping and shape-deformable membrane design to minimize air drag from the leg-wing opening during jumping, I will demonstrate the integrated jumping-perching-gliding.

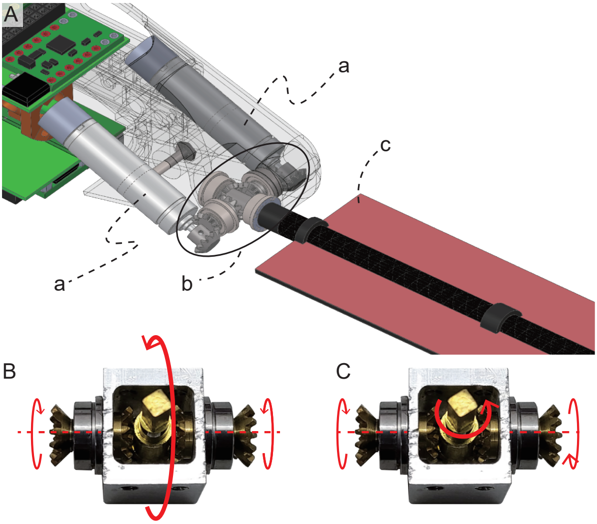

Figure 5.1.: Specification of the 2-axis active tail: A. 3D model design of the 2-axis tail (a. Dc motor, b. Gearbox for 2-axis operation, c. aerodynamic tail), B. Gear rotations for tail's rotation in the pitch direction, C. Gear rotations for tail's rotation in the roll direction.

5.2.2. Two-axis tail design

The additional degree of freedom to the active tail will provide control torques in multiple directions. I am planning to design the 2-axis active tail to achieve pitch control and stabilization in roll and yaw directions. In addition, the 2-axis active tail can reorientate the robot during jumping on the vertical surface. Figure 5.1 depicts the specification of the 2-axis active tail. Two actuators operate the active tail. The different rotational directions of the gear determine the tail's rotating directions: pitch (Figure 5.1B) and roll (Figure 5.1C).

5.2.3. Flexible active tail

In Chapter 1.2.1.3, I characterized the active tail's performance in transmitted torque for the body's pitch control. The characterization was focused only on the solid active tail. However, a flexible tail is a more common type in nature like a lizard's tail. In this sense, I am planning to compare the two types of tails: solid and flexible tails, and furthermore, characterize the flexible tail to employ it in the robot.

APPENDIX A

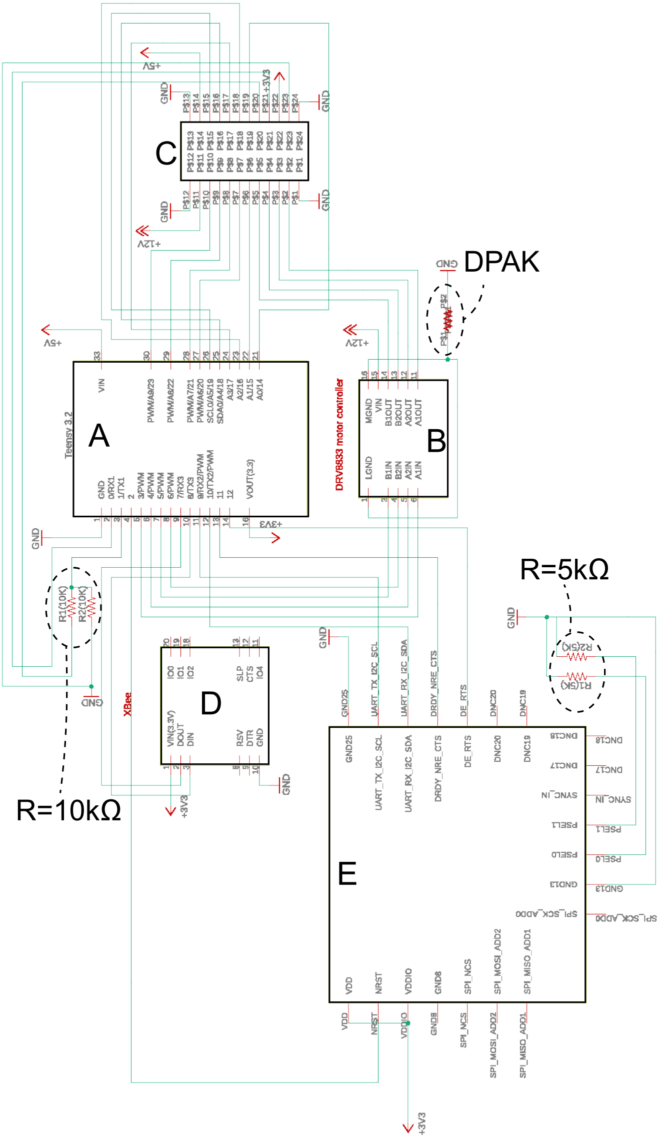

Figure A.1.: Schematic design of the main controller: A. Micro controller (Teensy3.2), B. Motor driver (DRV8833, Pololu), C. Connecotr (2X12), D. Xbee module, E. IMU sensor(MTI3, Xsens).

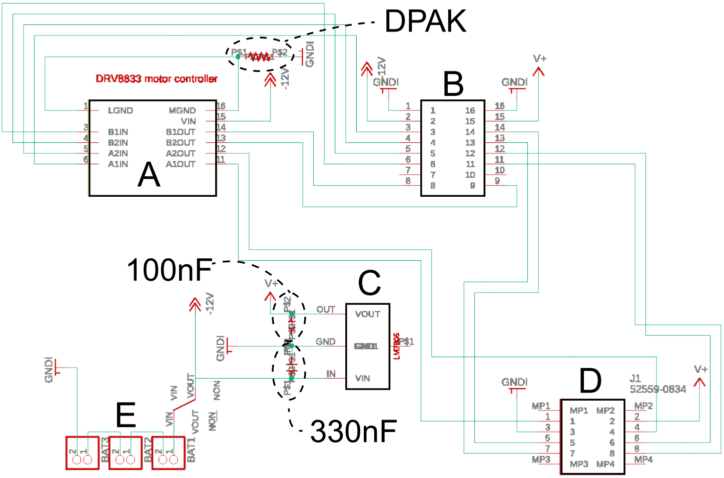

Figure A.2.: Schematic design of the sub controller: A. Motor driver (DRV8833, Pololu), B. connector (2x8), C. Voltage regulator, D. Connector for tail actuator (52559-0834,molex), E. Battery connector

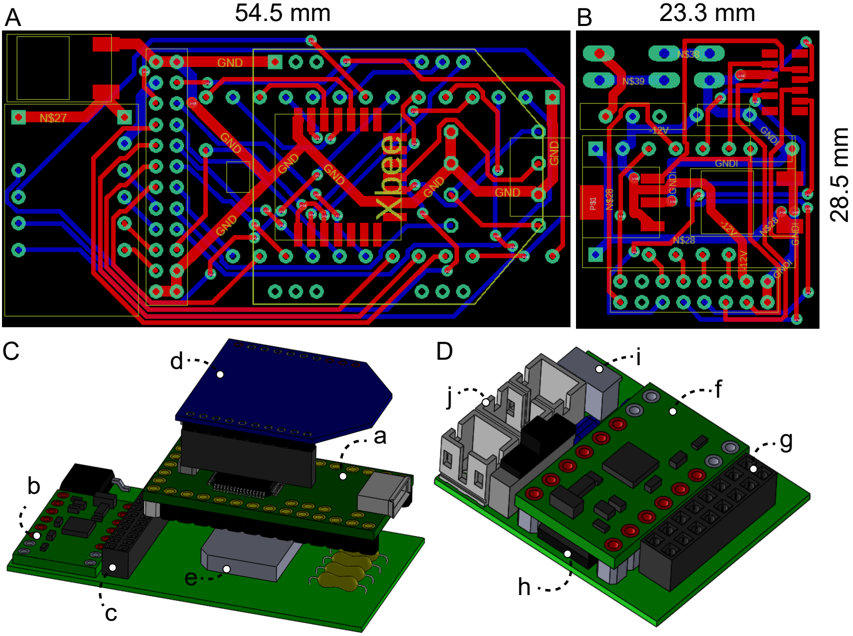

Figure A.3.: Route and node designs of PCB board: A. main board, B. power manager, and 3D model of the controller: C. 3D model for the main board (a. Micro controller (Teensy3.2), b. Motor driver (DRV8833, Pololu), c. Connecotr (2X12), d. Xbee module, e. IMU sensor(MTI3, Xsens)), D. 3D model for the power manager (f. Motor driver (DRV8833, Pololu), g. connector (2x8), h. Voltage regulator, i. Connector for tail actuator (52559-0834,molex). j. Battery connector).

Appendix B

Table B.1.: Jumping behaviors and comparison of jumping distances with and without the integrated perching.

	$\theta_j = 90°$	$\theta_j = 80°$	$\theta_j = 70°$	$\theta_j = 60°$	$\theta_j = 50°$	$\theta_j = 40°$	$\theta_j = 30°$
H_a (m)	$1.72^{+0.025}_{-0.017}$	$1.50^{+0.018}_{-0.026}$	$1.19^{+0.020}_{-0.026}$	$0.92^{+0.017}_{-0.018}$	$0.61^{+0.018}_{-0.011}$	$0.33^{+0.013}_{-0.009}$	$0.12^{+0.015}_{-0.006}$
D_a (m)	$0.45^{+0.021}_{-0.025}$	$1.08^{+0.029}_{-0.018}$	$1.41^{+0.020}_{-0.015}$	$1.52^{+0.011}_{-0.017}$	$1.49^{+0.016}_{-0.013}$	$1.27^{+0.019}_{-0.014}$	$0.88^{+0.013}_{-0.017}$
θ_a (Deg.)	$147.78^{+3.75}_{-1.56}$	$90.23^{+3.56}_{-2.04}$	$34.82^{+3.36}_{-1.97}$	$-9.83^{+2.86}_{-1.85}$	$-28.75^{+1.43}_{-1.35}$	$-46.94^{+2.03}_{-1.85}$	$-64.63^{+2.14}_{-1.93}$
v_a (m/s)	$0.56^{+0.09}_{-0.10}$	$1.78^{+0.09}_{-0.07}$	$2.98^{+0.10}_{-0.07}$	$3.89^{+0.06}_{-0.08}$	$4.65^{+0.06}_{-0.05}$	$5.03^{+0.04}_{-0.02}$	$5.86^{+0.04}_{-0.06}$
T_a (s)	$0.65^{+0.04}_{-0.02}$	$0.63^{+0.05}_{-0.03}$	$0.54^{+0.05}_{-0.05}$	$0.45^{+0.05}_{-0.07}$	$0.41^{+0.04}_{-0.02}$	$0.32^{+0.04}_{-0.02}$	$0.23^{+0.04}_{-0.03}$
D_l (m)	$0.90^{+0.048}_{-0.033}$	$2.04^{+0.032}_{-0.039}$	$2.84^{+0.049}_{-0.032}$	$3.23^{+0.036}_{-0.031}$	$3.15^{+0.030}_{-0.024}$	$2.15^{+0.025}_{-0.017}$	$1.72^{+0.027}_{-0.023}$
T_l (s)	$1.24^{+0.12}_{-0.06}$	$1.17^{+0.10}_{-0.08}$	$1.06^{+0.06}_{-0.08}$	$0.92^{+0.07}_{-0.02}$	$0.78^{+0.05}_{-0.06}$	$0.58^{+0.04}_{-0.05}$	$0.39^{+0.06}_{-0.05}$
D_p (%)	$300.24^{+11.21}_{-15.47}$	$93.72^{+1.67}_{-1.21}$	$44.32^{+0.48}_{-0.69}$	$25.81^{+0.23}_{-0.27}$	$17.84^{+0.14}_{-0.15}$	$6.03^{+0.04}_{-0.05}$	$0.13^{+0.03}_{-0.03}$

where H_a is the height of the robot at the apex, D_a is the distance of the robot from the initial position to the apex, θ_a is the pitch angle of the robot at the apex, v_a is the horizontal speed of the robot at the apex, T_a is the elapsed time of the robot at the apex, D_l is the jumping distance of the robot at the landing position, T_l is the elapsed time of the robot at the landing position, D_p is the changed jumping distance between jumping with angle and the integrated perching motion, $D_p = (D_l$ without perching - D_l with perching$)/$ D_l without perching x 100. The jumping distance with perching for each jumping angle was estimated from the result of the vertical jumping with perching.

APPENDIX C

APPENDIX C

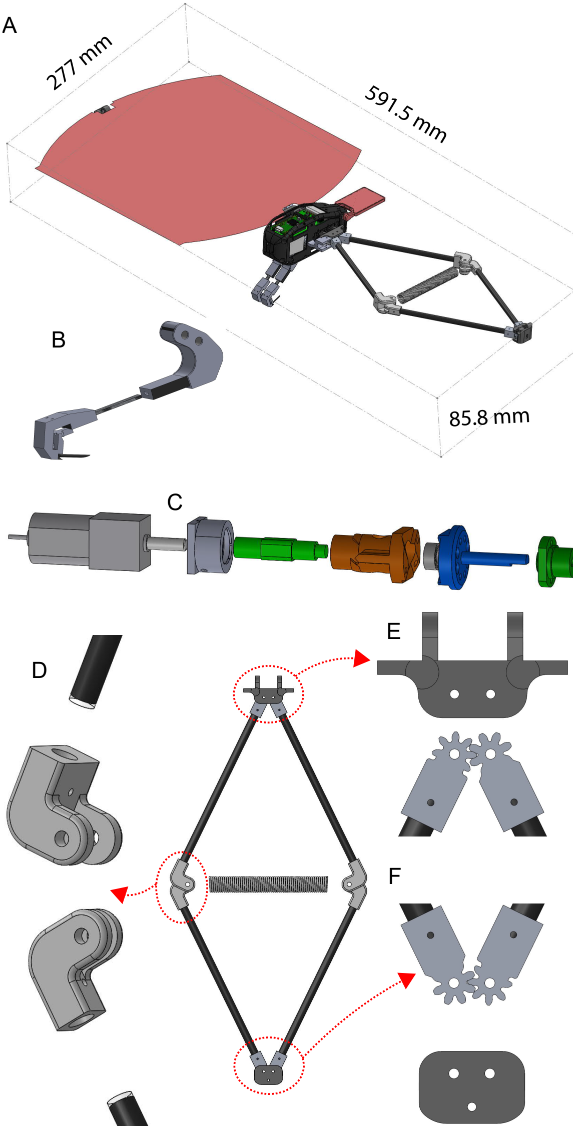

Figure C.1.: Assembly design through 3D modeling software. A. Overall robot size. Exploded views of the perching mechanism (B), jumping energy storage and release mechanism (C), and jumping mechanism's middle (D), upper (E), and lower (F) connections.

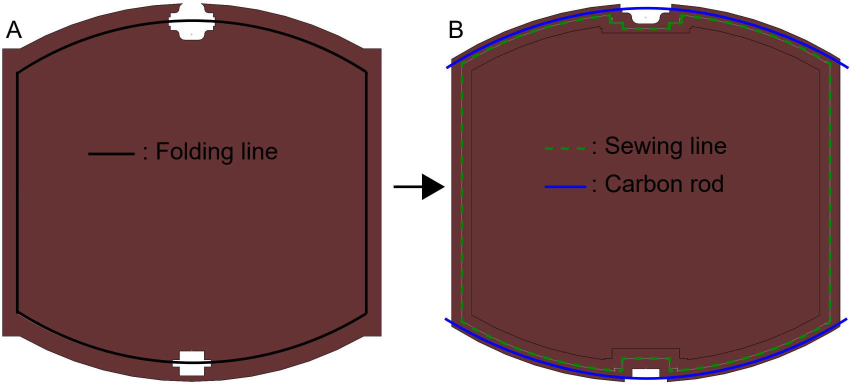

Figure C.2.: Fabrication process of the membrane. A. Original shape of the membrane cut by a laser cutting machine. B. Final shape after Folding and sewing to produce a space for the carbon rod.

APPENDIX D

Matlab code to derive dynamic equation

```matlab
%Define variables
valref={'var1' 'var2' 'var3'};
valref_dot={'dot_var1' 'dot_var2' 'dot_var3'};
valref_dot_dot={'dot_dot_var1' 'dot_dot_var2' 'dot_dot_var3'};

%Define constants
syms con1 con2 con3

%Transfrom the defined variables into symbols
for i=1:length(valref)
    eval(['syms ',char(valref(i))]);
    eval(['syms ',char(valref_dot(i))]);
    eval(['syms ',char(valref_dot_dot(i))]);
end

%Define positions of each body
P1y=P0y+ll*cos(th1);
P1z=P0z+ll*sin(th1);
%differentiation of defined positions
dot_P1y=Z_diff_t(P1y,P0y,P0z,th1,th2);
dot_P1z=Z_diff_t(P1z,P0y,P0z,th1,th2);
%Calculation of kinetic and potential energies
K1=0.5*m1*(dot_P1y^2+dot_P1z^2)+0.5*I1*(dot_th1)^2;
P1=m1*g*P1z;
%Calculation of Laglangian equation
L1=K1-P1;

%Summing all Lagrangian equations of each body
L=Lm+2*(L1+L2+L3+L4+Ls)+Lt;

%Transformation of symbol into character as function of time
```

```
for i=1:length(valref)
    eval([char(valref(i)),'=sym(''',char(valref(i)),'(t)''',');']);
    eval([char(valref_dot(i)),'=sym(''',char(valref_dot(i)),'(t)''',');']);
    eval([char(valref_dot_dot(i)),'=sym(''',char(valref_dot_dot(i)),'(t)''',');']);
end

%Replacing the variables in the Lagrangian equation into the time variables
for i=1:length(valref)
    L=eval(['subs(L,''',char(valref(i)),''',',char(valref(i)),');']);
    L=eval(['subs(L,''',char(valref_dot(i)),''',',char(valref_dot(i)),');']);
    L=eval(['subs(L,''',char(valref_dot_dot(i)),''',',char(valref_dot_dot(i)),');']);
end

%Calculation of dynamic equation from the Lagrangian equation
for i=1:length(valref)
    eval(['eq',num2str(i),'=simplify(diff(subs(diff(subs(L,',char(valref_dot(i)),',tmp),tmp),tmp,',char(valref_dot(i)),'),t)-subs(diff(subs(L,',char(valref(i)),',tmp),tmp),tmp,',char(valref(i)),'));']);
end

%Replacing the variables in the dynamic equation into the variables, which
%is not fuction of time
for i=1:length(valref)
for j=1:length(valref)
```

```
    eval([’eq’,num2str(i),’=subs(eq’,num2str(i),’,
       diff(’,char(valref_dot(j)),’, t),’,char(
       valref_dot_dot(j)),’);’]);
    eval([’eq’,num2str(i),’=subs(eq’,num2str(i),’,
       diff(’,char(valref(j)),’, t),’,char(valref_dot
       (j)),’);’]);
end
end

%Rearraging the dynamic equations into matrix form
for i=1:length(valref)
for j=1:length(valref)
eval([’M1(’,num2str(i),’,’,num2str(j),’)=simplify((
   collect(-eq’,num2str(i),’,’,char(valref_dot_dot(j)
   ),’)+subs(collect(eq’,num2str(i),’,’,char(
   valref_dot_dot(j)),’),’,char(valref_dot_dot(j)),’
   ,-’,char(valref_dot_dot(j)),’))/-2/’,char(
   valref_dot_dot(j)),’);’]);
eval([’eq’,num2str(i),’=eq’,num2str(i),’-M1(’,num2str
   (i),’,’,num2str(j),’)*’,char(valref_dot_dot(j)),’;
   ’]);
end
eval([’eq’,num2str(i),’=simplify(eq’,num2str(i),’);’
   ]);
end

for i=1:length(valref)
for j=1:length(valref)
eval([’M2(’,num2str(i),’,’,num2str(j),’)=simplify((
   collect(-eq’,num2str(i),’,’,char(valref_dot(j)),’)
   +subs(collect(eq’,num2str(i),’,’,char(valref_dot(j
   )),’),’,char(valref_dot(j)),’^2,-’,char(valref_dot
   (j)),’^2))/-2/’,char(valref_dot(j)),’^2);’]);
eval([’eq’,num2str(i),’=eq’,num2str(i),’-M2(’,num2str
   (i),’,’,num2str(j),’)*’,char(valref_dot(j)),’^2;’
```

```
]);
end
eval(['eq',num2str(i),'=simplify(eq',num2str(i),');']);
end

cou=1;
for i=1:length(valref)
for j=1:length(valref)-1
eval(['M3ref',num2str(i),num2str(j),'=simplify((collect(-eq',num2str(i),',',char(valref_dot(j)),')+subs(collect(eq',num2str(i),',',char(valref_dot(j)),'),',char(valref_dot(j)),',-',char(valref_dot(j)),'))/-2/',char(valref_dot(j)),');']);
    for k=j+1:length(valref)
        eval(['M3(',num2str(i),',',num2str(cou),')=simplify((collect(-M3ref',num2str(i),num2str(j),',',char(valref_dot(k)),')+subs(collect(M3ref',num2str(i),num2str(j),',',char(valref_dot(k)),'),',char(valref_dot(k)),',-',char(valref_dot(k)),'))/-2/',char(valref_dot(k)),');']);
        eval(['eq',num2str(i),'=eq',num2str(i),'-M3(',num2str(i),',',num2str(cou),')*',char(valref_dot(j)),'*',char(valref_dot(k)),';']);
        cou=cou+1;
    end
end
cou=1;
end

for i=1:length(valref)
for j=1:length(valref)
```

```
eval(['M4(',num2str(i),',',num2str(j),')=simplify((collect(-eq',num2str(i),',',char(valref_dot(j)),')+subs(collect(eq',num2str(i),',',char(valref_dot(j)),'),',char(valref_dot(j)),',-',char(valref_dot(j)),'))/-2/',char(valref_dot(j)),');']);
eval(['eq',num2str(i),'=eq',num2str(i),'-M4(',num2str(i),',',num2str(j),')*',char(valref_dot(j)),';']);
end
eval(['eq',num2str(i),'=simplify(eq',num2str(i),');']);
end

for i=1:length(valref)
eval(['M5(',num2str(i),')=simplify(eq',num2str(i),');']);
eval(['eq',num2str(i),'=eq',num2str(i),'-M5(',num2str(i),');']);
end
```

Matlab code to solve differential equations

```
% Define of initial vlaues
var1=0;
var2=0;
Gcon=0;

% Solving differential equations
while (Termination_condition)

[t result]=ode45(@Dynamic_model,[0 sampling],[var1
    var2 dot_Gvar1 dot_Gvar2]);

var1=result(end,1);
var2=result(end,2);

dot_Gvar1=result(end,3);
dot_Gvar2=result(end,4);

end
```

APPENDIX E

Software set-up for the motion capture system

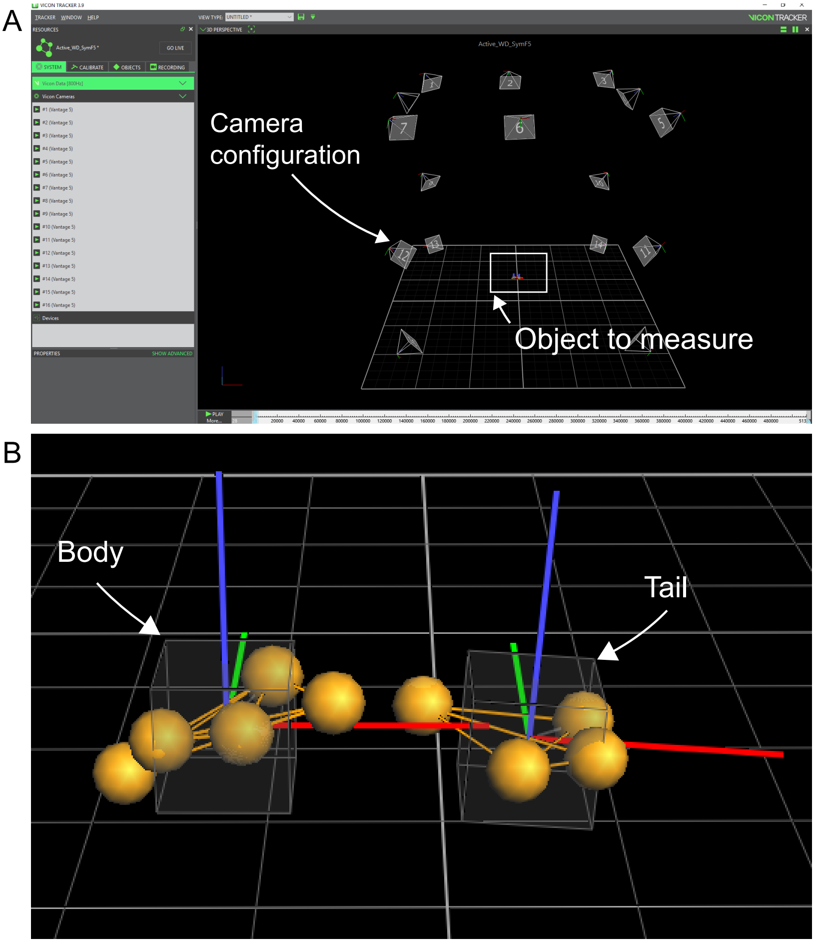

Figure E.1.: Software set-up of the motion capture system. A. Set-up for camera parameters, calibration, target object define. B. Defined target objects from attached markers at the body and tail. The marker at the body is 7 *mm* diameter spheres; The marker at the tail has 2 *mm* diameter spheres.

Software set-up for the high-speed camera

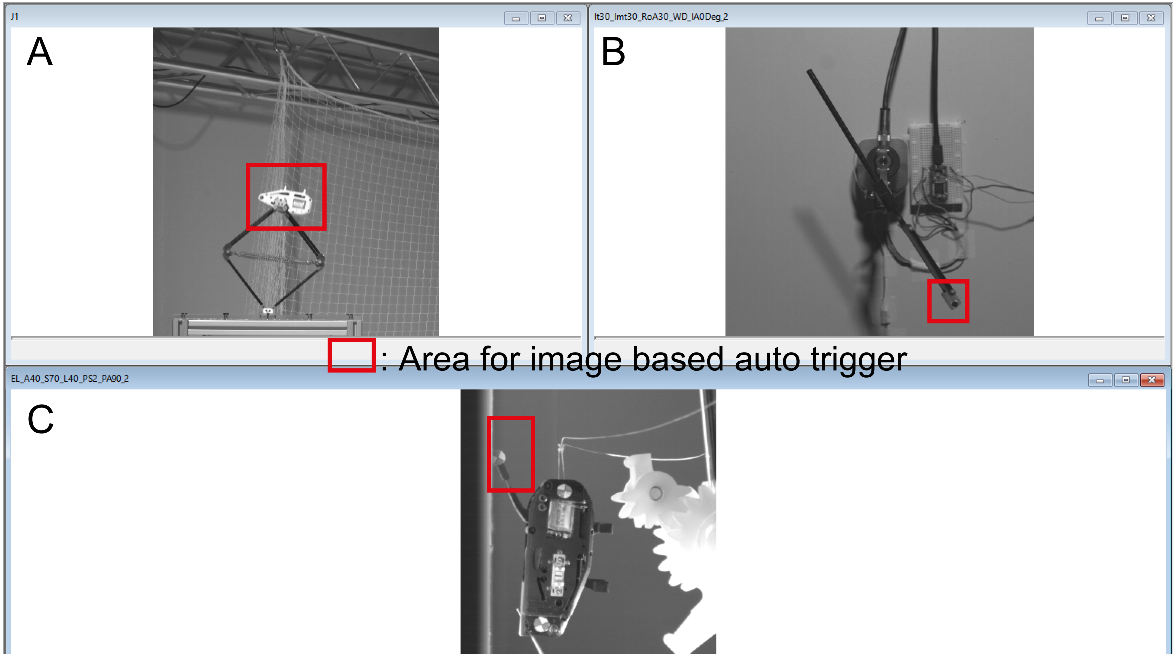

Figure E.2.: Software set-up of the high-speed camera: A. Set-ups to record jumping, B. active tail dynamics, and C. perching

REFERENCES

[1] Toshiba. *Small Robot Developed to Investigate Interior of Primary Containment Vessel of Fukushima Daiichi Nuclear Power Station Unit 2*. 2015. URL: `https://www.global.toshiba/ww/news/corporate/2015/06/pr3001.html` (visited on 30/06/2015) (cit. on p. 44).

[2] Toshiba. *New Toshiba and IRID Robot Will Inspect Interior of Primary Containment Vessel at Fukushima Daiichi 3*. 2017. URL: `https://www.global.toshiba/ww/news/corporate/2017/06/pr1501.html` (visited on 15/06/2017) (cit. on p. 44).

[3] S. R. Lab. *OceanOne Lands on the Moon*. URL: `https://khatib.stanford.edu/ocean-one.html` (cit. on p. 44).

[4] B.-H. Jun et al. 'A new concept and technologies of multi-legged underwater robot for high tidal current environment'. *2011 IEEE Symposium on Underwater Technology and Workshop on Scientific Use of Submarine Cables and Related Technologies*. 2011, pp. 1–5 (cit. on p. 44).

[5] B. Dynamics. *Spot*. URL: `https://www.bostondynamics.com/products/spot` (cit. on p. 44).

[6] G. Bledt et al. 'MIT Cheetah 3: Design and Control of a Robust, Dynamic Quadruped Robot'. *2018 IEEE/RSJ International Conference on Intelligent Robots and Systems (IROS)*. 2018, pp. 2245–2252 (cit. on p. 44).

[7] H.-W. Park et al. 'High-speed bounding with the MIT Cheetah 2: Control design and experiments'. *The International Journal of Robotics Research* 36.2 (2017), pp. 167–192 (cit. on p. 44).

[8] J. Cho et al. ‘Investigation of the emergency response robots used for mitigation of severe accident of the fukushima nuclear power plant’. *Institute of Control, Robotics and Systems Conference*. 2011, pp. 1–8 (cit. on p. 44).

[9] A. L. Desbiens et al. ‘Design principles for efficient, repeated jumpgliding’. *Bioinspiration & biomimetics* 9.2 (2014), p. 025009 (cit. on pp. 46, 55).

[10] A. Vidyasagar et al. ‘Performance analysis of jump-gliding locomotion for miniature robotics’. *Bioinspiration & biomimetics* 10.2 (2015), p. 025006 (cit. on pp. 46, 48, 58).

[11] A. L. Desbiens et al. ‘Efficient jumpgliding: Theory and design considerations’. *2013 IEEE International Conference on Robotics and Automation*. IEEE. 2013, pp. 4451–4458 (cit. on pp. 46, 48, 58).

[12] M. Kovač et al. ‘The locomotion capabilities of the EPFL jumpglider: A hybrid jumping and gliding robot’. *2011 IEEE International Conference on Robotics and Biomimetics*. IEEE. 2011, pp. 2249–2250 (cit. on p. 46).

[13] M. A. Woodward et al. ‘Design of a miniature integrated multi-modal jumping and gliding robot’. *2011 IEEE/RSJ International Conference on Intelligent Robots and Systems*. IEEE. 2011, pp. 556–561 (cit. on pp. 46, 48, 50, 58, 64, 66, 109, 157).

[14] M. A. Woodward et al. ‘Multimo-bat: A biologically inspired integrated jumping–gliding robot’. *The International Journal of Robotics Research* 33.12 (2014), pp. 1511–1529 (cit. on pp. 46, 48–50, 58, 64, 66, 109, 132, 143, 157).

[15] M. A. Woodward. *MultiMo-Bat: Biologically Inspired Integrated Multi-Modal Locomotion*. Carnegie Mellon University, 2017 (cit. on pp. 46, 49, 50, 64, 66, 157).

[16] W. Roderick et al. ‘Bird-inspired dynamic grasping and perching in arboreal environments’. *Science Robotics* 6.61 (2021), eabj7562 (cit. on pp. 46, 50, 83).

[17] K. Hang et al. ‘Perching and resting—A paradigm for UAV maneuvering with modularized landing gears’. *Science Robotics* 4.28 (2019), eaau6637 (cit. on pp. 46, 82).

[18] M. T. Pope et al. ‘A multimodal robot for perching and climbing on vertical outdoor surfaces’. *IEEE Trans. Robot.* 33.1 (2016), pp. 38–48 (cit. on p. 46).

[19] H.-N. Nguyen et al. ‘A passively adaptive microspine grapple for robust, controllable perching’. *2019 2nd IEEE International Conference on Soft Robotics (RoboSoft)*. IEEE. 2019, pp. 80–87 (cit. on p. 46).

[20] M. A. Graule et al. ‘Perching and takeoff of a robotic insect on overhangs using switchable electrostatic adhesion’. *Science* 352.6288 (2016), pp. 978–982 (cit. on p. 46).

[21] L. Daler et al. ‘A perching mechanism for flying robots using a fibre-based adhesive’. *2013 IEEE International Conference on Robotics and Automation*. IEEE. 2013, pp. 4433–4438 (cit. on p. 46).

[22] A. S. Boxerbaum et al. ‘Design of an autonomous amphibious robot for surf zone operation: part I mechanical design for multi-mode mobility’. *IEEE/ASME Int. Conf. Adv. Intell. Mechatron.* IEEE. 2005, pp. 1459–1464 (cit. on p. 46).

[23] S. Floyd et al. ‘A novel water running robot inspired by basilisk lizards’. *2006 IEEE/RSJ International Conference on Intelligent Robots and Systems*. IEEE. 2006, pp. 5430–5436 (cit. on pp. 46, 47).

[24] H. Kim et al. ‘Water and ground-running robotic platform by repeated motion of six spherical footpads’. *IEEE/ASME Transactions on Mechatronics* 21.1 (2015), pp. 175–183 (cit. on p. 46).

[25] J. Gray. ‘The mechanism of locomotion in snakes’. *Journal of experimental biology* 23.2 (1946), pp. 101–120 (cit. on p. 46).

[26] P. Liljebäck et al. ‘A review on modelling, implementation, and control of snake robots’. *Robotics and Autonomous systems* 60.1 (2012), pp. 29–40 (cit. on p. 46).

[27] T. Horvat et al. ‘Inverse kinematics and reflex based controller for body-limb coordination of a salamander-like robot walking on uneven terrain’. *2015 IEEE/RSJ International Conference on Intelligent Robots and Systems (IROS)*. IEEE. 2015, pp. 195–201 (cit. on p. 46).

[28] W. Wang et al. ‘Bio-inspired design and realization of a novel multimode amphibious robot’. *2009 IEEE International Conference on Automation and Logistics*. IEEE. 2009, pp. 140–145 (cit. on p. 46).

[29] V. Kaznov et al. 'Outdoor navigation with a spherical amphibious robot'. *2010 IEEE/RSJ International Conference on Intelligent Robots and Systems*. IEEE. 2010, pp. 5113–5118 (cit. on p. 46).

[30] J. Yu et al. 'On a bio-inspired amphibious robot capable of multimodal motion'. *IEEE/ASME Transactions On Mechatronics* 17.5 (2011), pp. 847–856 (cit. on p. 46).

[31] K. Peterson et al. 'Experimental dynamics of wing assisted running for a bipedal ornithopter'. *2011 IEEE/RSJ International Conference on Intelligent Robots and Systems*. IEEE. 2011, pp. 5080–5086 (cit. on p. 46).

[32] F. J. Boria et al. 'A sensor platform capable of aerial and terrestrial locomotion'. *2005 IEEE/RSJ International Conference on Intelligent Robots and Systems*. IEEE. 2005, pp. 3959–3964 (cit. on p. 46).

[33] L. Daler et al. 'A bioinspired multi-modal flying and walking robot'. *Bioinspiration & biomimetics* 10.1 (2015), p. 016005 (cit. on p. 46).

[34] Q.-V. Nguyen et al. 'Design and demonstration of a locust-like jumping mechanism for small-scale robots'. *Journal of Bionic Engineering* 9.3 (2012), pp. 271–281 (cit. on p. 46).

[35] R. Niiyama et al. 'Mowgli: A bipedal jumping and landing robot with an artificial musculoskeletal system'. *Proceedings 2007 IEEE International Conference on Robotics and Automation*. IEEE. 2007, pp. 2546–2551 (cit. on p. 46).

[36] B. Jun et al. 'Design and control of jumping mechanism for a Kangaroo-inspired robot'. *2016 6th IEEE International Conference on Biomedical Robotics and Biomechatronics (BioRob)*. IEEE. 2016, pp. 436–440 (cit. on p. 46).

[37] N. T. Jafferis et al. 'Untethered flight of an insect-sized flapping-wing micro-scale aerial vehicle'. *Nature* 570.7762 (2019), pp. 491–495 (cit. on p. 46).

[38] H. Huang et al. 'An all servo-driven bird-like flapping-wing aerial robot capable of autonomous flight'. *IEEE/ASME Transactions on Mechatronics* (2022) (cit. on p. 46).

[39] Festo. *BionicSwift*. 2021. URL: `https://www.festo.com/de/en/e/about-festo/research-and-development/bionic-learning-network/highlights-from-2018-to-2021/bionicswift-id_326830/` (cit. on p. 46).

[40] D. Zarrouk et al. ‘STAR, a sprawl tuned autonomous robot’. *2013 IEEE International Conference on Robotics and Automation*. IEEE. 2013, pp. 20–25 (cit. on p. 47).

[41] D. Zarrouk et al. ‘Rising STAR: A highly reconfigurable sprawl tuned robot’. *IEEE Robotics and automation letters* 3.3 (2018), pp. 1888–1895 (cit. on p. 47).

[42] K. Jayaram et al. ‘Cockroaches traverse crevices, crawl rapidly in confined spaces, and inspire a soft, legged robot’. *Proceedings of the National Academy of Sciences* 113.8 (2016), E950–E957 (cit. on p. 47).

[43] K. Autumn et al. ‘Evidence for van der Waals adhesion in gecko setae’. *Proceedings of the National Academy of Sciences* 99.19 (2002), pp. 12252–12256 (cit. on pp. 47, 87).

[44] M. P. Murphy et al. ‘Gecko-inspired directional and controllable adhesion’. *Small* 5.2 (2009), pp. 170–175 (cit. on p. 47).

[45] S. Kim et al. ‘Smooth vertical surface climbing with directional adhesion’. *IEEE Transactions on robotics* 24.1 (2008), pp. 65–74 (cit. on p. 47).

[46] D. Santos et al. ‘Directional adhesive structures for controlled climbing on smooth vertical surfaces’. *Proceedings 2007 IEEE International Conference on Robotics and Automation*. IEEE. 2007, pp. 1262–1267 (cit. on p. 47).

[47] C. Menon et al. ‘Gecko inspired surface climbing robots’. *2004 IEEE international conference on robotics and biomimetics*. IEEE. 2004, pp. 431–436 (cit. on p. 47).

[48] M. Carlo et al. ‘A biomimetic climbing robot based on the gecko’. *Journal of Bionic Engineering* 3.3 (2006), pp. 115–125 (cit. on p. 47).

[49] O. Unver et al. ‘Geckobot: A gecko inspired climbing robot using elastomer adhesives’. *Proceedings 2006 IEEE International Conference on Robotics and Automation, 2006. ICRA 2006.* IEEE. 2006, pp. 2329–2335 (cit. on p. 47).

[50] S. Kim et al. ‘Whole body adhesion: hierarchical, directional and distributed control of adhesive forces for a climbing robot’. *Proceedings 2007 IEEE International Conference on Robotics and Automation*. IEEE. 2007, pp. 1268–1273 (cit. on p. 47).

[51] D. Santos et al. ‘Gecko-inspired climbing behaviors on vertical and overhanging surfaces’. *2008 IEEE International Conference on Robotics and Automation*. IEEE. 2008, pp. 1125–1131 (cit. on p. 47).

[52] M. J. Spenko et al. ‘Biologically inspired climbing with a hexapedal robot’. *Journal of field robotics* 25.4-5 (2008), pp. 223–242 (cit. on p. 47).

[53] A. Sintov et al. ‘Design and motion planning of an autonomous climbing robot with claws’. *Robotics and Autonomous Systems* 59.11 (2011), pp. 1008–1019 (cit. on p. 47).

[54] A. Ji et al. ‘A bio-inspired climbing robot with flexible pads and claws’. *Journal of Bionic Engineering* 15.2 (2018), pp. 368–378 (cit. on p. 47).

[55] M. Sfakiotakis et al. ‘Review of fish swimming modes for aquatic locomotion’. *IEEE Journal of oceanic engineering* 24.2 (1999), pp. 237–252 (cit. on p. 47).

[56] R. Du et al. ‘Robot fish’. *Berlin, Heidelberg: Springer. doi* 10 (2015), pp. 978–3 (cit. on p. 47).

[57] J. Glasheen et al. ‘A hydrodynamic model of locomotion in the basilisk lizard’. *Nature* 380.6572 (1996), pp. 340–342 (cit. on p. 47).

[58] S. T. Hsieh. ‘Three-dimensional hindlimb kinematics of water running in the plumed basilisk lizard (Basiliscus plumifrons)’. *Journal of Experimental Biology* 206.23 (2003), pp. 4363–4377 (cit. on p. 47).

[59] S. T. Hsieh et al. ‘Running on water: three-dimensional force generation by basilisk lizards’. *Proceedings of the National Academy of Sciences* 101.48 (2004), pp. 16784–16788 (cit. on p. 47).

[60] S. Floyd et al. ‘Design and development of the lifting and propulsion mechanism for a biologically inspired water runner robot’. *IEEE transactions on robotics* 24.3 (2008), pp. 698–709 (cit. on p. 47).

[61] H. S. Park et al. ‘Dynamic modeling of a basilisk lizard inspired quadruped robot running on water’. *2008 IEEE/RSJ International Conference on Intelligent Robots and Systems*. IEEE. 2008, pp. 3101–3107 (cit. on p. 47).

[62] H. S. Park et al. ‘Dynamic modeling and analysis of pitch motion of a basilisk lizard inspired quadruped robot running on water’. *2009 IEEE International Conference on Robotics and Automation*. IEEE. 2009, pp. 2655–2660 (cit. on p. 47).

[63] W. D. Shin et al. 'Bio-inspired design of a gliding-walking multi-modal robot'. *2018 IEEE/RSJ International Conference on Intelligent Robots and Systems (IROS)*. IEEE. 2018, pp. 8158–8164 (cit. on p. 47).

[64] D. W. Haldane et al. 'Robotic vertical jumping agility via series-elastic power modulation'. *Science Robotics* 1.1 (2016), eaag2048 (cit. on pp. 47, 54, 55).

[65] A. Crespi et al. 'Salamandra robotica II: an amphibious robot to study salamander-like swimming and walking gaits'. *IEEE Transactions on Robotics* 29.2 (2013), pp. 308–320 (cit. on p. 47).

[66] A. Crespi et al. 'AmphiBot II: An amphibious snake robot that crawls and swims using a central pattern generator'. *Proceedings of the 9th international conference on climbing and walking robots (CLAWAR 2006)*. CONF. 2006, pp. 19–27 (cit. on p. 47).

[67] M. Kovač et al. 'The EPFL jumpglider: A hybrid jumping and gliding robot with rigid or folding wings'. *2011 IEEE International Conference on Robotics and Biomimetics*. IEEE. 2011, pp. 1503–1508 (cit. on pp. 48, 58).

[68] K. Kim et al. 'A bipedal walking robot that can fly, slackline, and skateboard'. *Science Robotics* 6.59 (2021), eabf8136 (cit. on p. 48).

[69] W. Saab et al. 'Design and Integration of a Novel Spatial Articulated Robotic Tail'. *IEEE/ASME Trans. Mechatronics* 24.2 (2019), pp. 434–446 (cit. on p. 48).

[70] B. Li et al. 'Transition Optimization for a VTOL Tail-Sitter UAV'. *IEEE/ASME Trans. Mechatronics* 25.5 (2020), pp. 2534–2545 (cit. on p. 48).

[71] Y. Shen et al. 'Biomimetic Realization of a Robotic Penguin Wing: Design and Thrust Characteristics'. *IEEE/ASME Trans. Mechatronics* 26.5 (2021), pp. 2350–2361 (cit. on p. 48).

[72] G. Bledt et al. 'MIT Cheetah 3: Design and control of a robust, dynamic quadruped robot'. *Proc. IEEE/RSJ Int. Conf. Intell. Robot. Syst.* IEEE. 2018, pp. 2245–2252 (cit. on p. 48).

[73] H.-W. Park et al. 'Variable-speed quadrupedal bounding using impulse planning: Untethered high-speed 3d running of mit cheetah 2'. *Proc. IEEE Int. Conf. Robot. Autom.* IEEE. 2015, pp. 5163–5170 (cit. on p. 48).

[74] H.-W. Park et al. ‘High-speed bounding with the MIT Cheetah 2: Control design and experiments’. *Int. J. Robot. Res.* 36.2 (2017), pp. 167–192 (cit. on p. 48).

[75] R. Briggs et al. ‘Tails in biomimetic design: Analysis, simulation, and experiment’. *Proc. IEEE/RSJ Int. Conf. Intell. Robot. Syst.* IEEE. 2012, pp. 1473–1480 (cit. on p. 48).

[76] D. W. Haldane et al. ‘Repetitive extreme-acceleration (14-g) spatial jumping with Salto-1P’. *Proc. IEEE/RSJ Int. Conf. Intell. Robot. Syst.* IEEE. 2017, pp. 3345–3351 (cit. on pp. 49, 54, 55).

[77] H. Kim et al. ‘Active Tail Configurations for Enhanced Body Reorientation Performance’. *Advanced Intelligent Systems* n/a.n/a (), p. 2200219. eprint: `https://onlinelibrary.wiley.com/doi/pdf/10.1002/aisy.202200219`. URL: `https://onlinelibrary.wiley.com/doi/abs/10.1002/aisy.202200219` (cit. on pp. 49, 50, 58, 60, 113, 114).

[78] H. Kim et al. ‘Enhanced Non-Steady Gliding Performance of the MultiMo-Bat through Optimal Airfoil Configuration and Control Strategy’. *Proc. IEEE/RSJ Int. Conf. Intell. Robot. Syst.* IEEE. 2018, pp. 1382–1388 (cit. on pp. 49, 50, 58, 60, 141, 142, 146, 147, 149).

[79] T. Libby et al. ‘Tail-assisted pitch control in lizards, robots and dinosaurs’. *Nature* 481.7380 (2012), pp. 181–184 (cit. on pp. 49, 54).

[80] E. Chang-Siu et al. ‘A lizard-inspired active tail enables rapid maneuvers and dynamic stabilization in a terrestrial robot’. *Proc. IEEE/RSJ Int. Conf. Intell. Robot. Syst.* IEEE. 2011, pp. 1887–1894 (cit. on p. 49).

[81] A. Jusufi et al. ‘Righting and turning in mid-air using appendage inertia: reptile tails, analytical models and bio-inspired robots’. *Bioinspir. Biomim.* 5.4 (2010), p. 045001 (cit. on p. 49).

[82] T. Libby et al. ‘Comparative design, scaling, and control of appendages for inertial reorientation’. *IEEE Trans. Robot.* 32.6 (2016), pp. 1380–1398 (cit. on p. 49).

[83] H. Kim et al. ‘Avian-Inspired Perching Mechanism for Jumping Robots’. *Advanced Intelligent Systems* (2023), p. 2300072 (cit. on pp. 50, 60, 81, 82).

[84] A. T. Asbeck et al. ‘Scaling hard vertical surfaces with compliant microspine arrays’. *Int. J. Robot. Res.* 25.12 (2006), pp. 1165–1179 (cit. on pp. 52, 87).

[85] N. J. Kohut et al. ‘Precise dynamic turning of a 10 cm legged robot on a low friction surface using a tail’. *Proc. IEEE Int. Conf. Robot. Autom.* IEEE. 2013, pp. 3299–3306 (cit. on pp. 53, 55).

[86] J. Zhao et al. ‘Controlling aerial maneuvering of a miniature jumping robot using its tail’. *Proc. IEEE/RSJ Int. Conf. Intell. Robot. Syst.* IEEE. 2013, pp. 3802–3807 (cit. on pp. 53, 55).

[87] J. Zhao et al. ‘MSU tailbot: Controlling aerial maneuver of a miniature-tailed jumping robot’. *IEEE/ASME Trans. Mechatronics* 20.6 (2015), pp. 2903–2914 (cit. on pp. 53, 55).

[88] A. Patel et al. ‘Rapid acceleration and braking: Inspirations from the cheetah’s tail’. *Proc. IEEE Int. Conf. Robot. Autom.* IEEE. 2014, pp. 793–799 (cit. on pp. 53, 55).

[89] A. Patel et al. ‘On the conical motion of a two-degree-of-freedom tail inspired by the cheetah’. *IEEE Trans. Robot.* 31.6 (2015), pp. 1555–1560 (cit. on pp. 53, 55).

[90] G.-H. Liu et al. ‘A bio-inspired hopping kangaroo robot with an active tail’. *J. Bionic Eng.* 11.4 (2014), pp. 541–555 (cit. on pp. 53, 55).

[91] X. Zhang et al. ‘Effects of head and tail as swinging appendages on the dynamic walking performance of a quadruped robot’. *Robotica* 34.12 (2016), pp. 2878–2891 (cit. on pp. 53, 55).

[92] C. Casarez et al. ‘Using an inertial tail for rapid turns on a miniature legged robot’. *Proc. IEEE Int. Conf. Robot. Autom.* IEEE. 2013, pp. 5469–5474 (cit. on pp. 54, 55).

[93] J. K. Yim et al. ‘Precision jumping limits from flight-phase control in Salto-1P’. *Proc. IEEE/RSJ Int. Conf. Intell. Robot. Syst.* IEEE. 2018, pp. 2229–2236 (cit. on pp. 54, 55).

[94] J. W. Bahlman et al. ‘Glide performance and aerodynamics of non-equilibrium glides in northern flying squirrels (Glaucomys sabrinus)’. *J. R. Soc. Interface* 10.80 (2013), p. 20120794 (cit. on p. 54).

[95] K. L. Bishop. ‘The relationship between 3-D kinematics and gliding performance in the southern flying squirrel, Glaucomys volans’. *J. Exp. Biol.* 209.4 (2006), pp. 689–701 (cit. on p. 54).

[96] N. J. Kohut et al. ‘Aerodynamic steering of a 10 cm high-speed running robot’. *Proc. IEEE/RSJ Int. Conf. Intell. Robot. Syst.* IEEE. 2013, pp. 5593–5599 (cit. on p. 54).

[97] A. Suarez et al. ‘Winged aerial manipulation robot with dual arm and tail’. *Appl. Sci.* 10.14 (2020), p. 4783 (cit. on p. 54).

[98] S. Channel. *Stunning Footage of a Kubong Gliding Through the Trees*. Youtube. URL: `https://www.youtube.com/watch?v=T79dJPqVVA4$%5C&$t=36s$%5C&$ab$%5C_$channel%20=SmithsonianChannel` (cit. on p. 54).

[99] BBCEarth. *Flying Dragons Of The Jungle | Planet Earth II*. Youtube. URL: `https://www.youtube.com/watch?v=rBVgbxTkEuo&ab_channel=BBCEarth` (cit. on p. 54).

[100] J. Norby et al. ‘Enabling Dynamic Behaviors With Aerodynamic Drag in Lightweight Tails’. *IEEE Trans. Robot.* (2021) (cit. on p. 55).

[101] H. Kim et al. ‘Tail-Assisted Mobility and Stability Enhancement in Yaw and Pitch Motions of a Water-Running Robot’. *IEEE/ASME Trans. Mechatronics* 22.3 (2017), pp. 1207–1217 (cit. on p. 55).

[102] A. Pelletier et al. ‘Low Reynolds number aerodynamics of low-aspect-ratio, thin/flat/cambered-plate wings’. *Journal of aircraft* 37.5 (2000), pp. 825–832 (cit. on p. 55).

[103] S. Sunada et al. ‘Comparison of wing characteristics at an ultralow Reynolds number’. *Journal of aircraft* 39.2 (2002), pp. 331–338 (cit. on p. 55).

[104] M. Kovac et al. ‘A 1.5 g SMA-actuated microglider looking for the light’. *Proceedings 2007 IEEE International Conference on Robotics and Automation*. IEEE. 2007, pp. 367–372 (cit. on p. 55).

[105] A. Paranjape et al. ‘Closed-loop perching and spatial guidance laws for bio-inspired articulated wing MAV’. *AIAA Guidance, Navigation, and Control Conference*. 2012, p. 4979 (cit. on p. 55).

[106] M. Di Luca et al. ‘Bioinspired morphing wings for extended flight envelope and roll control of small drones’. *Interface focus* 7.1 (2017), p. 20160092 (cit. on p. 55).

[107] A. Jusufi et al. ‘Active tails enhance arboreal acrobatics in geckos’. *Proceedings of the National Academy of Sciences* 105.11 (2008), pp. 4215–4219 (cit. on p. 55).

[108] U. Norberg. 'How a long tail and changes in mass and wing shape affect the cost for flight in animals'. *Functional Ecology* (1995), pp. 48–54 (cit. on p. 55).

[109] A. L. Thomas. 'Why do birds have tails? The tail as a drag reducing flap, and trim control'. *Journal of Theoretical Biology* 183.3 (1996), pp. 247–253 (cit. on p. 55).

[110] C. E. Doyle et al. 'An avian-inspired passive mechanism for quadrotor perching'. *IEEE/ASME Trans. Mechatronics* 18.2 (2012), pp. 506–517 (cit. on p. 82).

[111] D. D. Chin et al. 'Birds repurpose the role of drag and lift to take off and land'. *Nat. Commun.* 10.1 (2019), pp. 1–10 (cit. on p. 82).

[112] A. Mo et al. 'Effective viscous damping enables morphological computation in legged locomotion'. *Front. Robot. AI.* 7 (2020), p. 110 (cit. on p. 83).

[113] K. Zhang et al. 'Bioinspired design of a landing system with soft shock absorbers for autonomous aerial robots'. *J. Field Robot.* 36.1 (2019), pp. 230–251 (cit. on p. 83).

[114] T. Bartelds et al. 'Compliant Aerial Manipulators: Toward a New Generation of Aerial Robotic Workers'. *IEEE Robot. Autom. Lett.* 1.1 (2016), pp. 477–483 (cit. on p. 83).

[115] A. L. Desbiens et al. 'Landing, perching and taking off from vertical surfaces'. *Int. J. Robot. Res.* 30.3 (2011), pp. 355–370 (cit. on p. 83).

[116] J. E. Clark et al. 'Design of a bio-inspired dynamical vertical climbing robot' (2007) (cit. on p. 87).

[117] J. M. Brown et al. 'Maneuverability in dynamic vertical climbing'. *Proc. IEEE/RSJ Int. Conf. Intell. Robot. Syst.* IEEE. 2018, pp. 4340–4347 (cit. on p. 87).

[118] M. P. Austin et al. 'Leg design to enable dynamic running and climbing on bobcat'. *Proc. IEEE/RSJ Int. Conf. Intell. Robot. Syst.* IEEE. 2018, pp. 3799–3806 (cit. on p. 87).

[119] S. Wang et al. 'A palm for a rock climbing robot based on dense arrays of micro-spines'. *Proc. IEEE/RSJ Int. Conf. Intell. Robot. Syst.* IEEE. 2016, pp. 52–59 (cit. on p. 87).

[120] S. Kim et al. ‘SpinybotII: climbing hard walls with compliant microspines’. *Proc. IEEE Int. Conf. Robot. Autom.* IEEE. 2005, pp. 601–606 (cit. on p. 87).

[121] M. Kovač et al. ‘A perching mechanism for micro aerial vehicles’. *Journal of Micro-Nano Mechatronics* 5.3 (2009), pp. 77–91 (cit. on p. 87).

[122] J. S. Lee et al. ‘Self-engaging spined gripper with dynamic penetration and release for steep jumps’. *Proc. IEEE Int. Conf. Robot. Autom.* IEEE. 2018, pp. 6082–6089 (cit. on p. 87).

[123] H. W. Wopereis et al. ‘Mechanism for perching on smooth surfaces using aerial impacts’. *IEEE Int. Symp. Saf. Secur. Rescue Robot.* IEEE. 2016, pp. 154–159 (cit. on p. 87).

[124] R. Siddall et al. ‘Tails stabilize landing of gliding geckos crashing head-first into tree trunks’. *Commun. Biol.* 4.1 (2021), pp. 1–12 (cit. on p. 96).

[125] M. A. Woodward et al. ‘Morphological intelligence counters foot slipping in the desert locust and dynamic robots’. *Proc. Natl. Acad. Sci. U.S.A.* 115.36 (2018), E8358–E8367 (cit. on pp. 105, 157).

Role of the author

The relevant three studies of “Avian-Inspired Perching Mechanism for Jumping Robots”, "Active Tail Configurations for Enhanced Body Reorientation Performance", and "Enhanced Non-Steady Gliding Performance of the MultiMo-Bat through Optimal Airfoil Configuration and Control Strategy" described in Chapter 2, 3, and 4, were conducted by H. Kim, M. A. Woodward, and M. Sitti. Overall tasks, such as robot design, dynamic modeling, experimental setup, conducting experiments, data analysis, and paper writing have been completed by H. Kim with discussion, advice, and help of M. A. Woodward, and M. Sitti.

Declaration of authorship

I hereby certify that I am the sole author of this thesis entitled “Development of a Bio-inspired Multimodal Mobile Robot Platform” and that I have not used any sources other than those listed in the bibliography and identified as references. I further declare that I have not submitted this thesis at any other institution in order to obtain a degree.

HyunGyu Kim
Stuttgart, October 16th, 2023